Title
ON THE INDENTATION AND EROSION OF BRITTLE MATERIALS

Permalink
https://escholarship.org/uc/item/0972p638

Author
Khatibloo, M.A.

Publication Date
1981-06-01

LBL-11883

c2

Lawrence Berkeley Laboratory
UNIVERSITY OF CALIFORNIA

Materials & Molecular Research Division

ON THE INDENTATION AND EROSION OF BRITTLE MATERIALS

Mohsen Ashrafi Khatibloo
(Ph.D. thesis)

June 1981

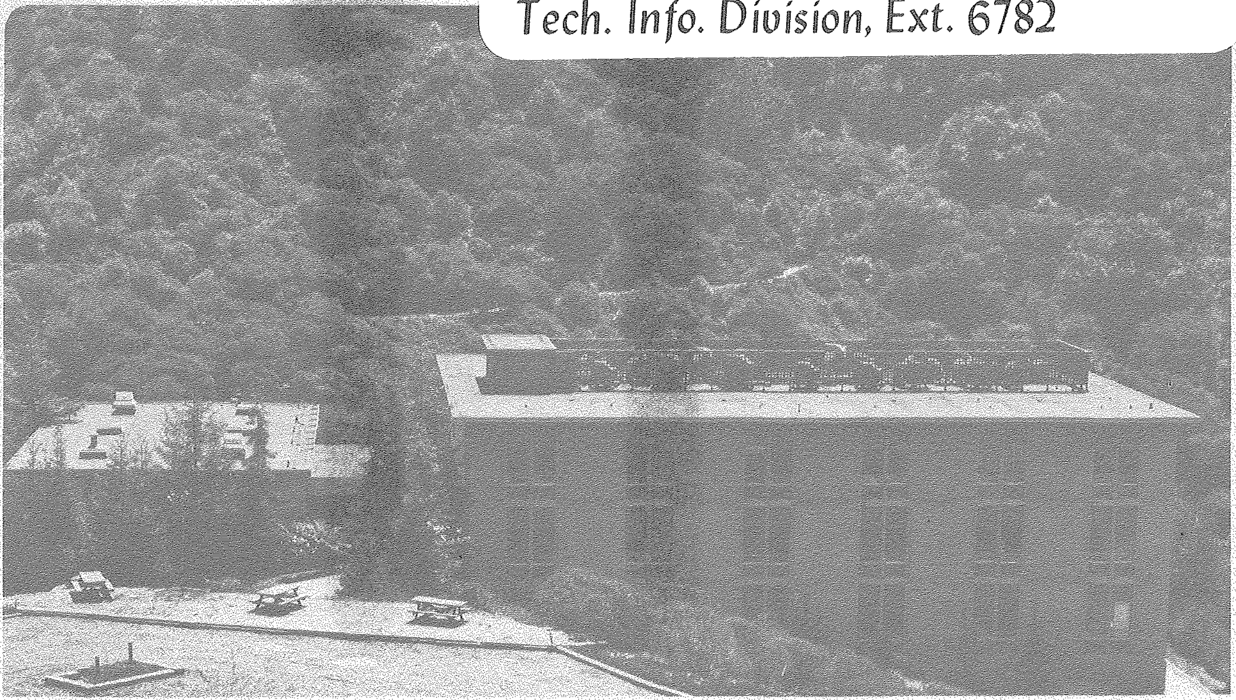

Prepared for the U.S. Department of Energy under Contract W-7405-ENG-48

LBL-11883

ON THE INDENTATION AND EROSION OF BRITTLE MATERIALS

Mohsen Ashrafi Khatibloo

Materials and Molecular Research Division
Lawrence Berkeley Laboratory
and Department of Materials Science and Mineral Engineering
University of California
Berkeley, CA 94720

This work was supported by the Director, Office of Energy Research, Office of Basic Energy Sciences, Materials Sciences Division of the U. S. Department of Energy under Contract No. W-7405-ENG-48.

ON THE INDENTATION AND EROSION OF BRITTLE MATERIALS

Contents

Abstract v

Acknowledgement. vi

1. Introduction 1

2. The Brittle and Ductile Behavior of Materials 4

    2.1. Microstructural Effect on Mechanical Behavior 7

    2.2. Plastic Deformation 11

3. Indenter-Surface Interaction 17

    3.1. Critical Angle of Attack as a Function of Material Behavior 18

    3.2. Crack Formation and Type 25

    3.3. Ring and Cone Cracks 26

    3.4. Median Vent and Radial Cracks 33

    3.5. Lateral Cracks 43

    3.6. Elastic Plastic Analysis 46

4. Indentation of Brittle (Elastic) Materials by Spherical Indenters--A Review of Past Work 59

    4.1. The Elastic Stress Field 62

    4.2. Comparison Between Experiment and Theory 70

    4.3. Energy Balance Approach 72

    4.4. Effects of Friction 76

    4.5. Surface Roughness 79

    4.6. Probabilistic Approaches 80

5. Indentation of Brittle Materials: A New Approach 87
    5.1. Criterion for Propagation of a Flaw 88
    5.2. Effect of Stress Gradient 91
    5.3. Location of Fracture 94
    5.4. Determination of Fracture Toughness by Indentation 100
    5.5. Load-Crack Size Relation 105
    5.6. The Auerbach Phenomenon and Its Range of Applicability . . 110
    5.7. Scatter in the Results 117
    5.8. Development of the Cone Crack 125
6. Analysis of the Erosion of Brittle Materials—A Historical Background 132
    6.1. Elastic Response 134
    6.2. Elastic-Plastic Response 138
7. Summary and Conclusions 145
Appendix A 148
References 149

ON THE INDENTATION AND EROSION OF BRITTLE MATERIALS

Mohsen Ashrafi Khatibloo

Materials and Molecular Research Division
Lawrence Berkeley Laboratory
and Department of Materials Science and Mineral Engineering
University of California
Berkeley, CA 94720

ABSTRACT

This work deals with the indentation and erosion of brittle materials. After a review of the extensive literature on both static indentation and low velocity impacts with round particles, no completely satisfactory explanation was found for the apparent increase in the strength of brittle materials as the indenter radius is decreased.

As a starting point, the mechanical behavior of brittle materials was studied and their various responses to loading were classified. The response can be elastic, elastic-plastic or completely plastic depending on the structure and bonding type of the material as well as the shape and size of the indenter. Plasticity occurs whenever sharp or very small indenters are used. In this case, it was found that the idealization of plastic deformation by an expanding cavity concept is a satisfactory one. A model using this approach showed that cracks refered to as median vent, radial and multiple cone cracks initiate and propagate along paths close to the principal stress trajectories in the uncracked solid. On the other hand, this model can give only the initiation locations of lateral cracks. A prediction of the crack trajectories in this case appears to require additional analysis.

A new model is developed for the elastic response regime. It was found that since the size of the surface flaws become comparable with the size of the stressed area, the critical stress intensity, instead of the maximum tensile stress, should be used as the fracture criterion. By taking this approach, an explanation for the relation noted by Auerbach in 1890 that fracture load varies linearly with indenter radius was obtained. The development also suggests a possible method for measuring the fracture toughness of a surface.

From erosion experiments it was found that analyses of single impacts on undamaged surfaces may not represent the steady state phase of erosion. However, they can provide some upper limit approximation of material removal. From all erosion analyses it is clear that fracture toughness should be a primary consideration when when selecting materials for their resistance to erosion. By comparison, hardness and elastic constants are less significant properties.

ACKNOWLEDGEMENT

I would like to express my sincere thanks and gratitude to Professor Iain Finnie. His continuous assistance and guideness toward completion of this work is greatly appreciated.

I also wish to extend by thanks to Mr. Al Levy and the Department of Energy who encouraged and supported this work.

The considerable patient effort, and competence shown by Ms Jean Wolslegel in typing the manuscript are deeply appreciated.

This work was supported by the Director, Office of Energy Research, Office of Basic Energy Sciences, Materials Sciences Division of the U. S. Department of Energy under contract No. W-7405-ENG-48.

1. INTRODUCTION

In many applications, the impact of small particles traveling in a fluid stream causes cuts, indentation, and removal of material from a surface. This process, known as the erosive wear of materials, occurs every day and its associated problems are too costly to ignore. There have been many efforts in the past and the present to understand this phenomenon and to classify materials for their resistance to erosion.

The prevention of component failure due to erosion is an important technological problem. For example, damage to gas turbine compressor blades caused by the inhalation of dust in off-highway vehicles and helicopters can cause severe reduction of service life. There are also severe erosion problems in many industrial processes which involve liquids or gases carrying entrained solid particles. Many such problems have been experimented in petrochemical plants. Severe erosion is also anticipated in proposed coal conversion processes. This has caused a great deal of concern as coal gasification and liquefaction become more attractive with the diminishing of oil and natural gas supplies.

Since many processes involving erosion occur at high temperatures where strength retention, creep resistance, and erosion resistance are important, ceramics, super alloys with protective coating, or alloys which get protected by their own oxides may have to be used to withstand the severe operating conditions. The combined corrosive-erosive behavior of such protective coatings which would generally be classified as brittle at room temperature is very complicated. However, an understanding of the behavior of bulk specimens of such materials should provide a better insight into their behavior as coatings.

The vast majority of the literature on erosion deals with ductile metals since these are the traditional materials used in mechanical equipment. Only recently has detailed attention been given to the erosion of brittle solids. For such materials, the mechanisms of removal are not well understood and the different studies in the literature present conflicting points of view. For this reason, and because of the potential importance of the erosion of brittle solids, the present work presents a detailed review and analysis of this topic.

In processes where low-velocity impact is encountered, damage caused by a particle closely resembles a quasi-static indentation. Because of this, calculations for erosion are generally based upon the formulation for static indentation. This also removes the distinction that otherwise might exist between the words "indenter" and "particle" or "projectile." An approach will be presented which appears to resolve some of the contradictions in the literature on fracture under spherical indenters and hopefully sheds some light on the processes involved in the indentation and erosion of brittle materials.

As a starting point, in Chapter 2 a general discussion is given of the brittle and ductile behavior of materials. An important aspect is the transition from brittle to ductile behavior that may occur when the size of the loaded region is very small.

In Chapter 3, the literature on indenter-surface interaction involving plastic deformation is collected and reviewed. With some extension, this information is used to explain test behavior. The situation in which indentations by spheres produce only elastic deformation prior to fracture is treated in Chapters 4 and 5. An interesting aspect of this fracture problem is that two completely different types of analysis, one probabilistic and one deterministic, have been used to explain the experimental results. In the present work, the limitations of both approaches are discussed and a new procedure is developed to explain the test results.

The analyses that have been developed to date for erosion of brittle solids are based on crack patterns observed under single indentations. This work is reviewed in Chapter 6, and the present knowledge on this subject is summarized. An attempt is made to access the importance of the different variables in erosion. Finally, Chapter 7 presents some general conclusions and suggestions for further research.

2. THE BRITTLE AND DUCTILE BEHAVIOR OF MATERIALS

Loading a material subjects it to two kinds of competing processes. One is permanent distortion due to plastic or viscous deformation, and the other is fracture from a preexisting or deformation induced flaw. Engineering materials are categorized as either ductile or brittle, based upon which one of these processes predominates.

In an ideally brittle material, the strain up to final failure is purely elastic. By contrast, a ductile material experiences large plastic strains prior to fracture. Thus, most metals are thought of as ductile materials while, on the other hand, ceramic materials can usually be categorized as brittle. In more detail, materials in general can be classified as:

1. Ductile at all temperatures. This group includes all face centered cubic (FCC) metals.

2. Ductile at room temperature, brittle at low temperature. This group includes many metals of non-FCC crystal structure such as iron, titanium, zinc, and magnesium.

3. Brittle at room temperature, ductile at elevated temperature. This group includes some metals such as beryllium, silicon, many intermetallic compounds, some ionic crystals such as sodium chloride, and glasses.

4. Brittle over a wide range of temperature. This group contains most carbides, nitrides, and oxides.

The behavior and strength of all materials is, of course, highly dependent on their type of bonding and microstructure. However, in the case of brittle materials an equally important aspect is the presence and density of inherent flaws. Indirect evidence for the presence of these flaws is provided by the large variability in strength of apparently similar specimens, the increase in average fracture stress as size is decreased, and the fact that strength values in bulk specimens are very much less than theoretical strength. As a result, the strength of brittle materials has to be specified by a function that depends on the flaw density and size, as well as on the inherent properties of the material.

Weibull,[1] as discussed later in Section 4.6, derived a mathematically convenient relation, with an implicit dependence on the above variables, to predict the failure probability of brittle materials. His expression for the cumulative density function was

$$P(\sigma) = 1 - \exp \int_v \left(\frac{\sigma - \sigma_u}{\sigma_o} \right)^m dv \qquad \sigma > \sigma_u \qquad (1a)$$

$$= 0 \qquad \sigma \leq \sigma_u \qquad (1b)$$

where σ_u is the stress below which there is zero probability of failure, σ_o is a scaling stress, v is the volume stressed in tension, and m is the parameter that characterizes the flaw distribution. These parameters can be deduced from experiment by testing a batch of similar specimens.

Equation (1) has been used successfully in a variety of applications involving the fracture of brittle materials. However, in all of these problems the number of flaws in the stressed volume v is very high. This would be the case in many conventional mechanical tests such as uniaxial tension or bending. However, reducing the size of the stressed volume by a large factor may cause two problems. First, the increase in the strength predicted from Eq. (1) may be so high that plastic flow may precede fracture. In this case, with some caution a nominally brittle material can be treated as if it were a ductile metal. Second, stress alone as used in Eq. (1) will not be a sufficient criterion for failure if the size of a typical flaw becomes comparable with the dimensions of the stressed volume. In such situations, the Weibull approach would not be realistic.

In principle, if the flaw sizes were known, the Weibull approach would not be necessary and could be replaced by the deterministic procedures of fracture mechanics. For problems such as indentation or erosion, the loaded region may be very small. For this reason it appears worthwhile to attempt to study such problems in a deterministic manner. In doing this it is realized that the flaw distribution may have to be based on certain assumptions and that the relation between fracture toughness, smooth bar strength, and flaw size is not well established for brittle materials. With these cautions, it appears that these aspects must be studied:

1) Influence of microstructure on mechanical behavior.

2) Flaw size and distribution.

3) Stress magnitude and distribution.

The first two are solely dependent on the target material, while the third one will change drastically if any plasticity occurs during contact. The third factor will depend on the material properties and shape of both contacting surfaces. Once these factors are known, and the boundary between brittle and ductile behavior is specified, in principle, a relation between all the controlling variables for prediction of fracture and its location can be obtained. However, the extent of damage or crack propagation are not as easily determined. To obtain an approximate answer for studying crack propagation and material removal one needs to resort to semiempirical methods based upon the formation and propagation of the most important types of cracks. In Chapter 3 the effect of the variables leading to formation of different types of cracks will be examined.

2.1. Microstructural Effect on Mechanical Behavior

From the point of view of mechanical behavior, it is convenient to divide ceramic materials into three categories. Depending on their crystal structures, bond character, and the temperature, they may be completely brittle, semibrittle, or ductile (Table I).

Table 1.

Category	Room Temperature	High Temperature
Completely Brittle	TiC, SiO_2, Al_2O_3, Si, TiO_2, SiC	
Semi Brittle	CaF_2, MgO, LiF, NaCl CsCl	Al_2O_3, TiO_2, MgO
Ductile	AgCl, AgBr	CaF_2, LiF, NaCl, CsCl

In the completely brittle category are materials in which dislocations cannot move, even at stresses approaching the theoretical strength. They are generally covalently bonded materials with complex structure at temperatures below approximately 0.5 Tm, where Tm is the absolute melting temperature.

Semibrittle solids include both the ionically bonded materials, with simple crystal structures at temperatures below approximately 0.5 Tm, and many covalent materials above that temperature. The dislocations find it difficult to cross-slip and cannot jump from one slip surface to another very easily. For structural reasons they are restricted to specific slip planes (plastic-anisotropy).

Ductile behavior is demonstrated by many ionically bonded materials in which dislocations can move and manoeuver easily with considerable flexibility in the choice of slip planes. These microscopic factors which control the flow stress and consequently hardness, as will be shown, play an important role in determining the type of damage that will occur in indentation and erosion. The variation of hardness, which is the reflection of dislocation mobility, versus modulus of elasticity (E), which is directly related to interatomic forces, is shown in Fig. 2.1. In both covalently and metallically bonded materials, the hardness is proportional to E, but the proportionality constant differs by a factor of about 500. This figure clearly shows the importance of the nature of interatomic bonding on the mechanical behavior of materials. Thus, for the ductile category, in which dislocations move more easily, the hardness is a small fraction of the elastic modulus (5×10^{-3} for the data shown). By contrast, the hardness of covalent crystals is a much higher fraction of the modulus (~10 percent). Most ceramics of interest lie somewhere in the spectrum between these specific categories of behavior. Where they lie again depends on their relative dislocation mobility, manoeuverability, and slip modes.

In this section, materials have been examined from a microscopic point of view. Whether permanent deformation appears on a macroscopic scale depends as much on the material structure as on the state of stress in the body. In the next section, this topic is discussed with particular attention to the size and geometry of the indenter.

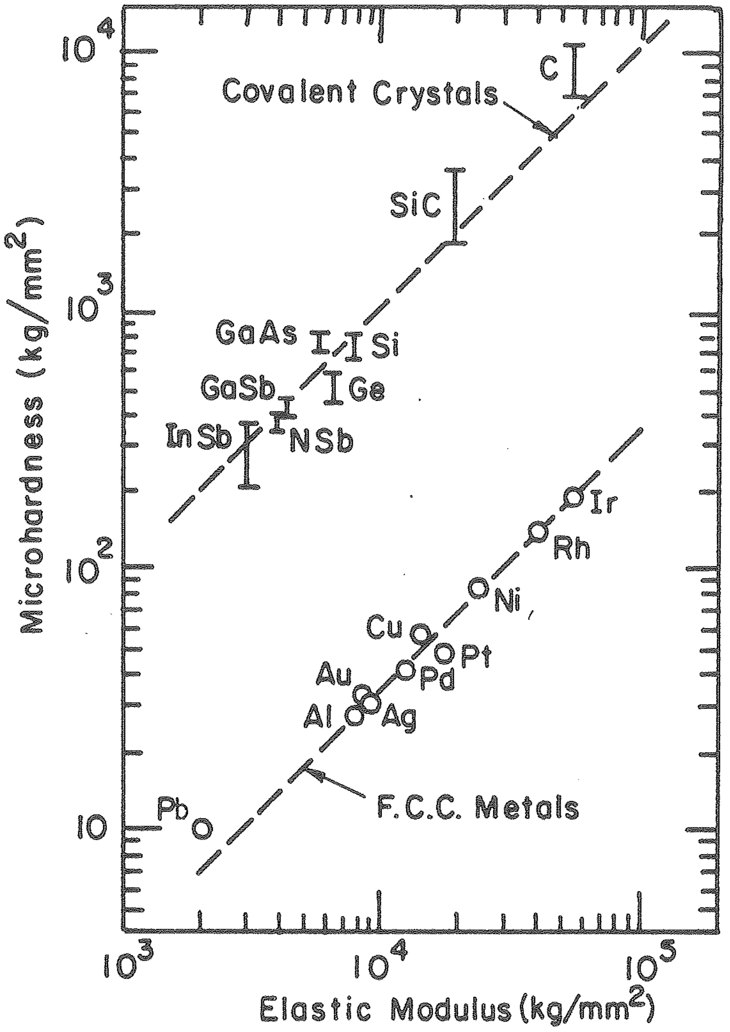

XBL8010-6205

Fig. 2.1. Hardness versus elastic modulus for F.C.C. metals and covalent crystals.[34]

2.2. Plastic Deformation

Impact of particles on brittle solids produces fragmentation of surface material around the impact site. The process of fragmentation, like the stress-strain curve of brittle materials, always appears to be completely brittle, regardless of the category of the target material (as discussed in the beginning of Section 2.1) and the particle used. This sometimes misleading information is what one might obtain by sequential photography of impacts. These pictures give a good global impression of the failure process. However, no detailed information about how propagation and interaction of cracks lead to fragmentation can be gained by this method. Crack formation and propagation are controlled by the magnitude and direction of the stresses due to impact. These two quantities can substantially change if the target responds plastically to impact loading. Therefore, it is very important to look for the existence of plasticity and the condition under which it occurs.

The presence of plastic deformation in otherwise brittle materials leads to a rather large discrepancy between the expected and measured surface energy values. Shand[2] and Roesler[3] showed that the energy absorbed in fracture of glass is much higher than the true (thermodynamic) surface energy. Because of this, the Griffith[4] energy approach to fracture prediction has been critized since no account was made for plastic deformation energy. The significance of this deformation naturally depends on its extent, which in turn is determined by the specific category in which that material falls.

Direct observation of fracture in glass has been said to provide other evidence of plastic flow. Photoelastic observations[5] show that large residual stresses exist at the root of a crack in glass. Originally it was believed[5,6] that the wedging action by the debris in the crack was responsible for the residual stresses that remain at the crack tip upon unloading. However, in other work it has been claimed that the residual stresses are due to plastic, deformation.[40]

Despite the extensive evidence for the occurrence of plastic deformation in nominally brittle solids, many investigators have been reluctant to accept this concept. On one hand, essentially ideal elastic behavior can occur. For example, Fig. 3.5 shows the top view of the cone-crack type of failure due to indentation of glass by a 3 mm spherical steel ball. In this case, stresses acting on surface flaws reach a critical value at a much lower load than that required for the start of plastic deformation below the indenter. While this type of failure can be classified as completely elastic, indenting the same material by a Vickers hardness tester, Fig. 3.9 shows plastic deformation. This fact was known as early as 1926 when Gohlhoff and Thomas[9] used scratching to measure hardness by drawing a lightly loaded point across a glass surface . Their result was similar to scratching a ductile material. Since at that time glass was thought of as a brittle material, this interesting observation prompted many other studies. For example, in 1957 Joos[10] showed a "scratch curl" formed by the material ejected from plastic furrows due to scratching. In larger scale experiments by Bridgeman and Simon,[11] they prevented premature failures by large hydrostatic pressures and observed as much as 25 percent plastic deformation in glass.

Statements have been made that materials that are brittle may show viscous flow in indentation due to heating. But clearly the experiments by Bridgeman and Simon,[11] and the fact that static tests produce no significant heating, discount those arguments. However, during dynamic testing substantial heating may develop. This may occur during ductile erosion due to the large plastic strains that are produced in a very short time.

Investigation of single-particle impact sites in metals by Hutchings et al.[12] has shown the formation of a shear lip at the exit side of the crater produced by particle impact. They concluded that temperatures exceeding the melting point of the metal could be generated during formation of the shear lip. More recent experiments by Hockey and Wiederhorn[13] on erosion of glass at 600°C and 15° impingement angle with 150 μm SiC particles traveling at 54 m/s, clearly show evidence of melting at the exit portion of the shear zone. By means of an analysis of the adiabatic shear process similar to that presented by Recht[14] and Yust et al.,[15] they found that it is possible to attain temperatures that exceed the melting point of the surface under the erosion condition of their experiment. Also, the lower thermal conductivity of ceramics favors generation of higher local temperatures than metals. Their calculations based upon adiabatic heating, even though very approximate, nonetheless indicate the possibility of reaching temperatures of the order of the melting point.

Most of the studies of ductile behavior in nominally brittle solids have been carried out with glasses. However, many studies have confirmed that such behavior also occurs in ceramic materials. Etch-pit techniques have been used to study the dislocation slip bands associated with impact damage or hardness impressions on "soft" ceramics like MgO and LiF.[16] Dislocations in these materials were found to propagate a considerable distance from the impact site, while in harder materials like SiC and Al_2O_3 they are located closer to the impact site. This close proximity, along with the lack of X-ray resolution and dissolution of dislocations by the etching process, creates difficulties when dealing with hard ceramics. These problems have been resolved by using TEM.

Studies by Hockey[18] give direct evidence of high densities of dislocations at both static indentations and impact sites. In both cases, high densities of dislocations, with qualitatively similar appearance, were found directly beneath the central region of contact and arrays of individual dislocations were found extending a short distance into the surrounding regions. Figure 2.2 shows an array of dislocations observed in alumina. However, these plastic impressions, unlike those in ductile materials, contain a high volume of twin-induced microcracks. Lankford[19] observed for Al_2O_3 that on the impression walls there are a large number of deformation bands which appear to be twins, based on their resemblance to the twins he observed in compression and tension tests. These twins became visible in many grains above a threshold stress level, and with increasing stress level

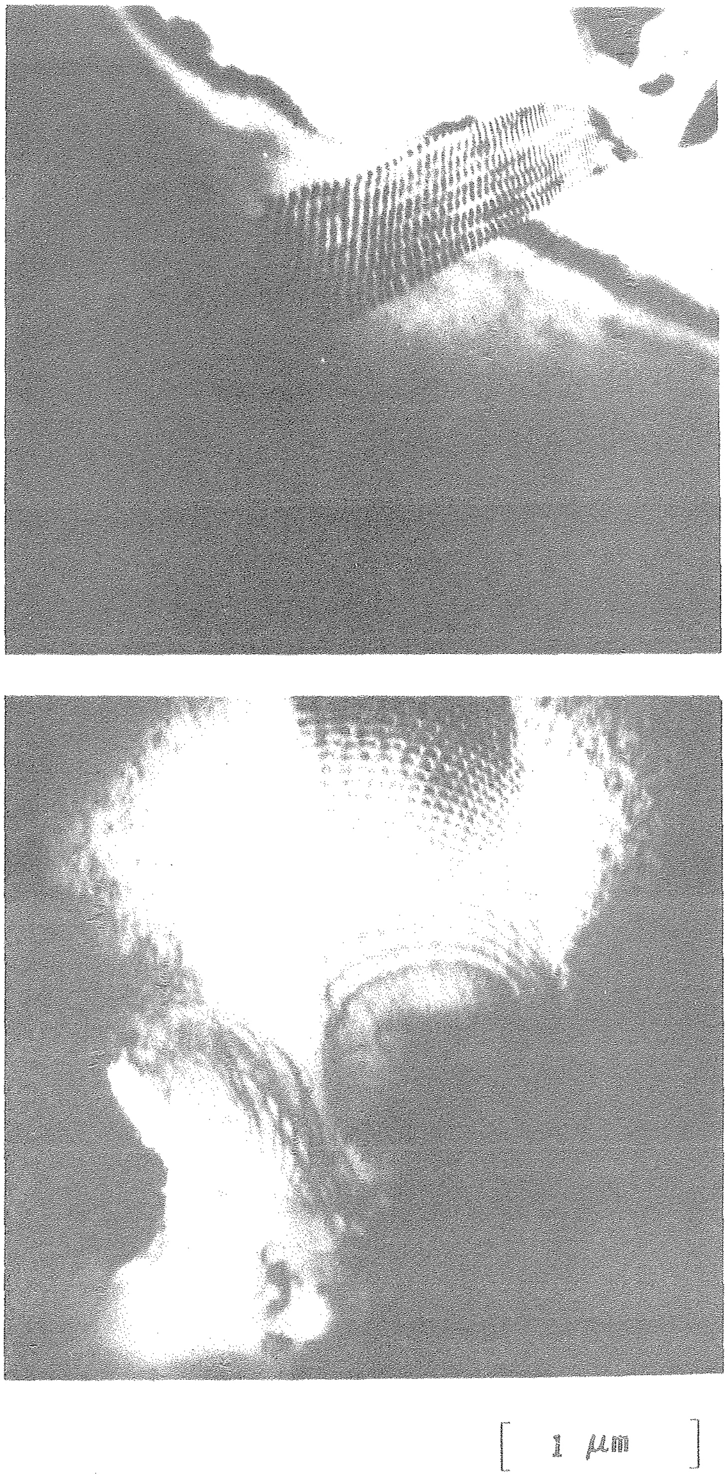

XBB 800-13457

Fig. 2.2. TEM photographs of dislocations generated in Al_2O_3 by impact.[7]

still more twins are produced. Also, microcracking associated with twin-grain boundary intersections and twin-plane decohesion regins to appear. It is interesting to note that twinning in Al_2O_3 during tensile tests ($T = 23^\circ C$, $\epsilon \sim 10^{-5}/s$) commences at around 130 MN m^{-2} (18 ksi), while compressive loading under similar conditions requires a stress level of about 1400 MN m^{-2} (193 ksi) to induce twinning. This stress level is an order of magnitude lower than its hardness.

This evidence indicates that plastic deformation, to a greater or lesser degree, always occurs during static indentation or impact loading of brittle materials, especially when hard angular particles or softer targets are used.

3. INDENTER-SURFACE INTERACTION

An essential first step in any erosion study is a knowledge of the prospective crack formation and geometry. The formation and propagation of cracks are controlled by the magnitude and direction of the principal stresses and the fracture toughness. If interaction is completely elastic, as usually expected for brittle materials, all the cracks, because of similarities in stress distribution, will have the same general pattern and a single model would be adequate for analysis of single impacts. However, crushing and plasticity or a combination of both under various circumstances are observed to occur. This will drastically change the stress distribution and consequently the crack pattern.

In the previous chapter it was pointed out that the response of brittle materials is as much dependent on their microstructure as on the indenter size and shape. Therefore, depending on the circumstances, a material may exhibit a brittle state in one application and ductile in another. Generally, the responses that are observed to occur can be classified in three different groups. They are:

1. Elastic response: sphere indenting a perfectly brittle material.

2. (a) Elastic-plastic response caused by the geometry of the indenter: cone or pyramid indenting a brittle or semibrittle material. (b) Elastic-plastic response resulting from the relatively low hardness of the surface: sphere indenting a semibrittle material.

3. Plastic response caused by the low hardness of the surface or size of the indenter: indentation of ductile materials, or brittle materials with very small indenters.

The above categories are separated by the extent (increasing from top to bottom) of plasticity. It should be noted that, as far as the material properties are concerned, hardness plays the most significant role, and whether the mean contact pressure reaches this value before fracture occurs is determined by the size and shape of the indenter as well as the fracture toughness.

3.1. Critical Angle of Attack as a Function of Material Deformation

The difference between ductile and brittle behavior, as well as the appearances of ductility in nominally brittle materials, are illustrated by the results of erosion tests in Figs. 3.1 and 3.2. These figures immediately show the distinct difference that exists between these two types of wear processes. Materials behaving in a ductile manner show a maximum removal rate at shallow angles while maximum removal for brittle materials occurs around 90°.

For both types of behavior, materials removal requires a certain stress or energy level for formation of new surfaces. This energy will be provided by the particle. But very little of the particle energy goes into creating new surfaces. A portion of it may be consumed by plastically deforming the surface, or may be preserved by rebounding from the surface. The normal component of velocity V_n is always capable of doing work. However, the effectiveness of the tangential component V_t will depend on the interference between the two

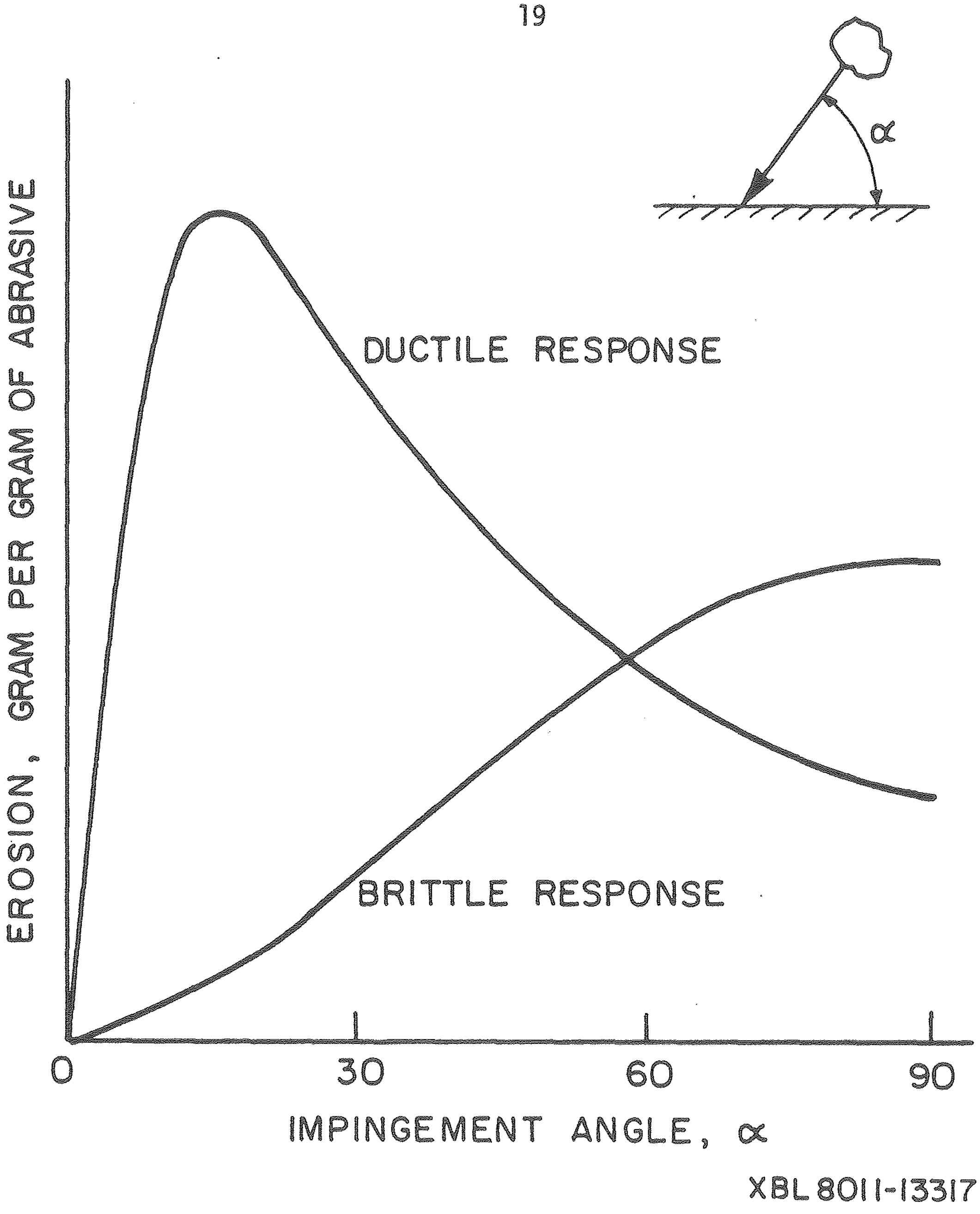

Fig. 3.1. Mass removed by erosion as a function of the angle of impingment α and the response of the material. Vertical scale is arbitrary.

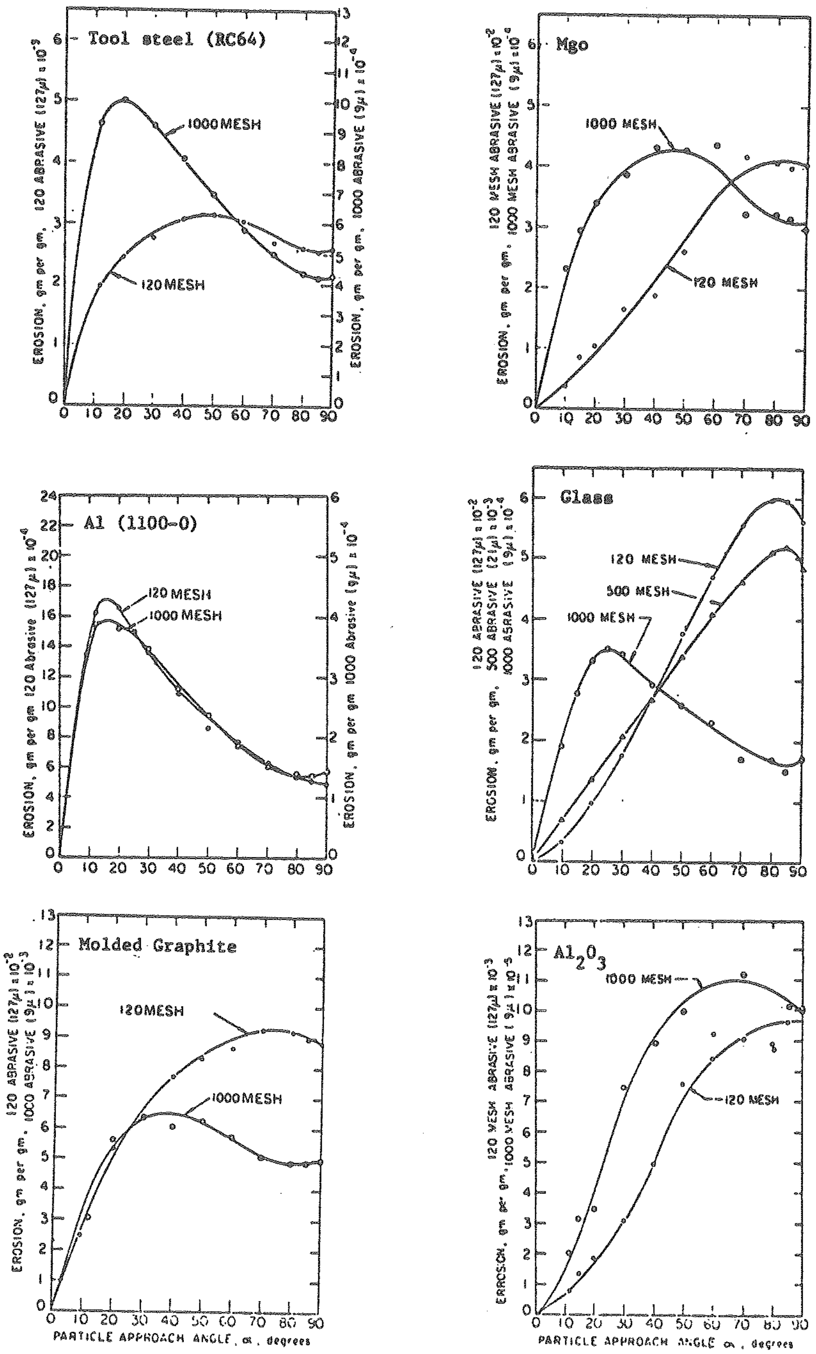

XBL 8010-12564

Fig. 3.2. Effect of particle size on the erosion of various materials.[47]

surfaces. It is convenient to define the interference or adhesion between the surfaces in terms of a coefficient of friction μ. The magnitude of μ is equal to the ratio of the average tangential-to-normal force. For instance, if μ is zero, tangential momentum will be preserved. For $\mu > 0$, the maximum tangential force that the surface may experience is the lesser of the force that V_t can produce and the normal force times μ. The friction coefficient, which depends on the amount of particle penetration and adhesion between the surfaces, is low for brittle materials due to their high hardness. But, it should be high for ductile materials or for a brittle material that behaves in ductile manner. So, while the tangential momentum of the particle may be totally consumed in eroding a ductile material, it may be preserved when impacting a brittle material. Therefore, brittle materials tend to erode more at high impingement angles. This is confirmed by the results of erosion of various surfaces with 127 μm (120 mesh) SiC particles shown in Fig. 3.2. The peak of these curves is reached slightly off the normal position, $\alpha = 90^\circ$. This would be found only when penetration is increased by using angular particles like SiC. With spherical steel shot the curves consistently peak at $\alpha = 90^\circ$.

The erosion of ductile materials appears to occur by at least two separate mechanisms. First, cutting at low angles of impingement, and second, failure due to a very complex shearing process at high angles. The cutting action at low angles has been analyzed. However, no definite model has yet been developed for high-angle erosion, which is sometimes known as deformation wear. Nevertheless, a general agreement exists that removal is due to overstraining, and possibly fatigue of the surface material.

Finnie's theory[20] of erosive cutting of ductile materials under the action of a stream of particles predicts low-angle erosion very well. The theory assumes that a hard angular particle cuts into the surface much like a sharp tool, and the maximum removal occurs in the range $15^\circ < \alpha < 25^\circ$. Very close correlation with experiment verifies the cutting action assumption. However, the contribution of cutting to material removal reduces at high angles, while that due to "deformation wear" increases. Examination of the deformation-wear process in more detail reveals that single particles most likely cause no material removal.[8] In this case, the net result is a gross deformation of the surface caused by a rather large displacement of material around and underneath the impact site. Accumulation of plasticity continues by repetitive impacts until the material is removed by a mechanism that is not yet understood.

Removal may occur by a process involving low-cycle fatigue or by an extrusion and shearing mechanism. This process consumes a great deal of energy. Therefore, the resulting removal rate is much lower than that due to cutting. The increase in the contribution of deformation wear and the reduction in cutting causes the removal rate to decrease at large angles.

It appears that if the resistance of a material to penetration (hardness) is increased, the angle α_{max} for maximum erosion is increased. In the limit, when very hard (brittle) surfaces are impacted by blunt particles, α_{max} reaches 90 degrees. This point is illustrated in Fig. 3.2, where various surfaces are eroded with 9 μm (1000 mesh) and 127 μm (120 mesh) SiC particles at various impingement angles. Particles of 9 μm size erode the surface, especially the softer ones, as if they were ductile, and indeed the mechanism of removal is the same. The values of angle corresponding to maximum removal rate, α_{max}, for each particle size and surface hardness are tabulated in Table 2 and plotted in Fig. 3.3.

Table 2.

Material	Hardness (GPa)	α_{max} (9 μm)	α_{max} (127 μm)
Al	0.5	15	16
Tool Steel	6.0	22	52
Glass	6.3	22	80
MgO	9.2	48	80
Al_2O_3	18.0	65	90

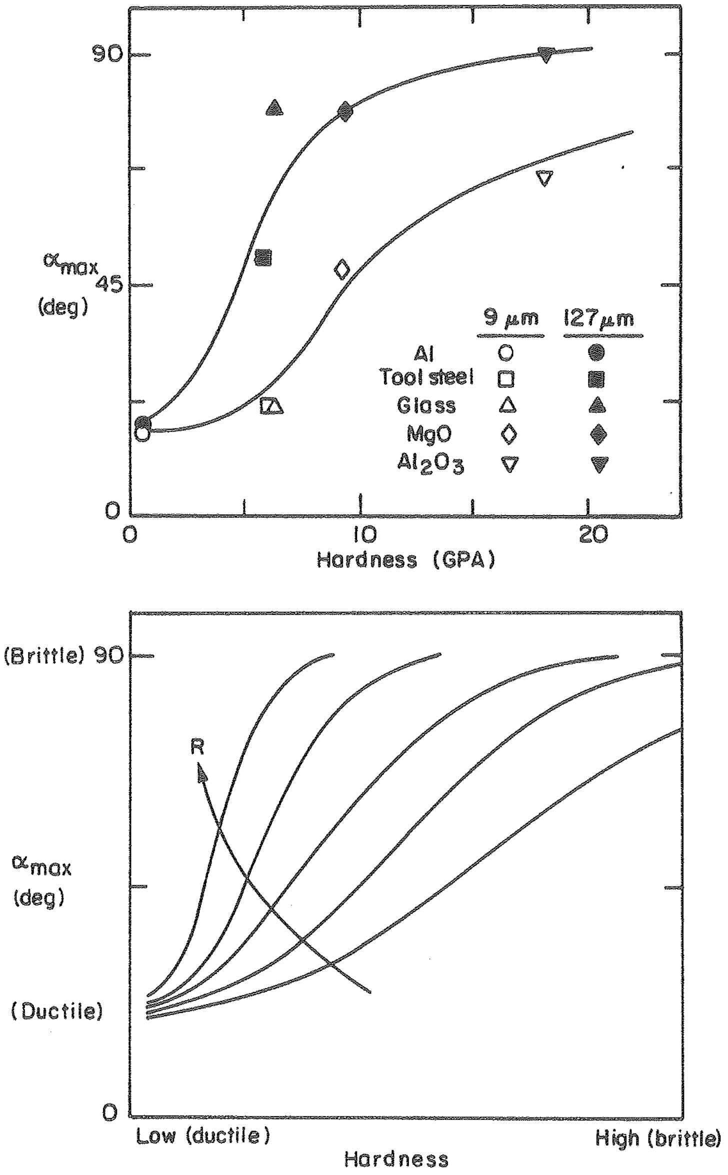

XBL 8010-6206

Fig. 3.3. Effect of hardness and particle size on the transition from brittle to ductile behavior.

Also shown in Fig. 3.3 is a schematic representation of the general effect of particle size on α_{max} for various hardness values. By examining Table 2 and Fig. 3.3, two conclusions about the effect of hardness on the angle of maximum removal rate can be reached: (a) increase of hardness increases the value of α_{max} for any particle size, and (2) the transition from ductile to brittle behavior with changing hardness becomes sharper when larger particles are used.

3.2. Crack Formation and Type

It was pointed out in the previous sections that, depending on the target material and particle size and shape, there are three different types of response with some overlapping. They were classified as either elastic, elastic-plastic, or completely plastic responses.

Elastic response is self-explanatory. However, definitions used for elastic-plastic or completely plastic response are different from those used for describing the uniaxial stress-strain curve of a material. Elastic-plastic response in the present context implies that material below the contact area, where compressive hydrostatic pressures and shear stresses are greatest, plastically deforms; but the actual brittle fracture starts from the elastic-plastic boundary and propagates into the elastic material.

Plastic response is associated with completely ductile behavior, where no cracking in the elastically stressed region occurs, and the material removal may be caused by a combination of over-straining, cutting, or fatigue. Of source, the significance of the contribution of each of these removal mechanisms as discussed depends on the angle of attack, α.

In indentation or erosion of brittle materials, the first two cases are usually encountered. The type of cracking associated with these responses are discussed in the following sections. The third case which, except for ductile materials, occurs only for very small particles will not be considered in the present work, since its treatment belongs with the study of ductile materials.

3.3. Ring and Cone Cracks

The nature of contact and the fracture that results due to impact or indentation of an elastic-brittle surface by an elastic sphere is named after Hertz, the famous scientist who first studied this problem. In the Hertzian fracture test, the surface of the material is depressed in a controlled way until it responds by fracturing, as opposed to plastically deforming as in the case of the hardness test. This test by virtue of its ease of application is by far the most extensively studied elastic contact configuration.

The cracking associated with the Hertzian stress field, as shown in Figs. 3.4 and 3.5, initiates from a critical pre-existing surface flaw located at a radius typically 10-30 percent greater than that of the contact area. After encircling the contact area in the form of a shallow ring crack, it propagates downward to form a frustrum of a cone. But because of the diminishing stresses below the surface, propagation becomes stable with crack growth. Typically, stable propagation is observed when the size of the cone c_c becomes

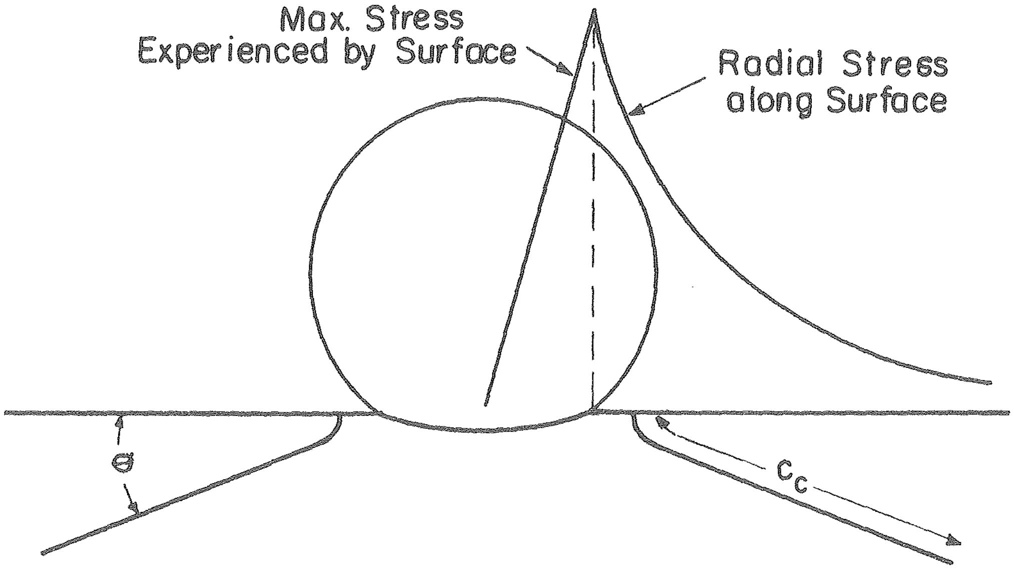

XBL 8010-6207

Fig. 3.4. Schematic representation of cone crack formation and the relative magnitude of the radial stress on the surface.

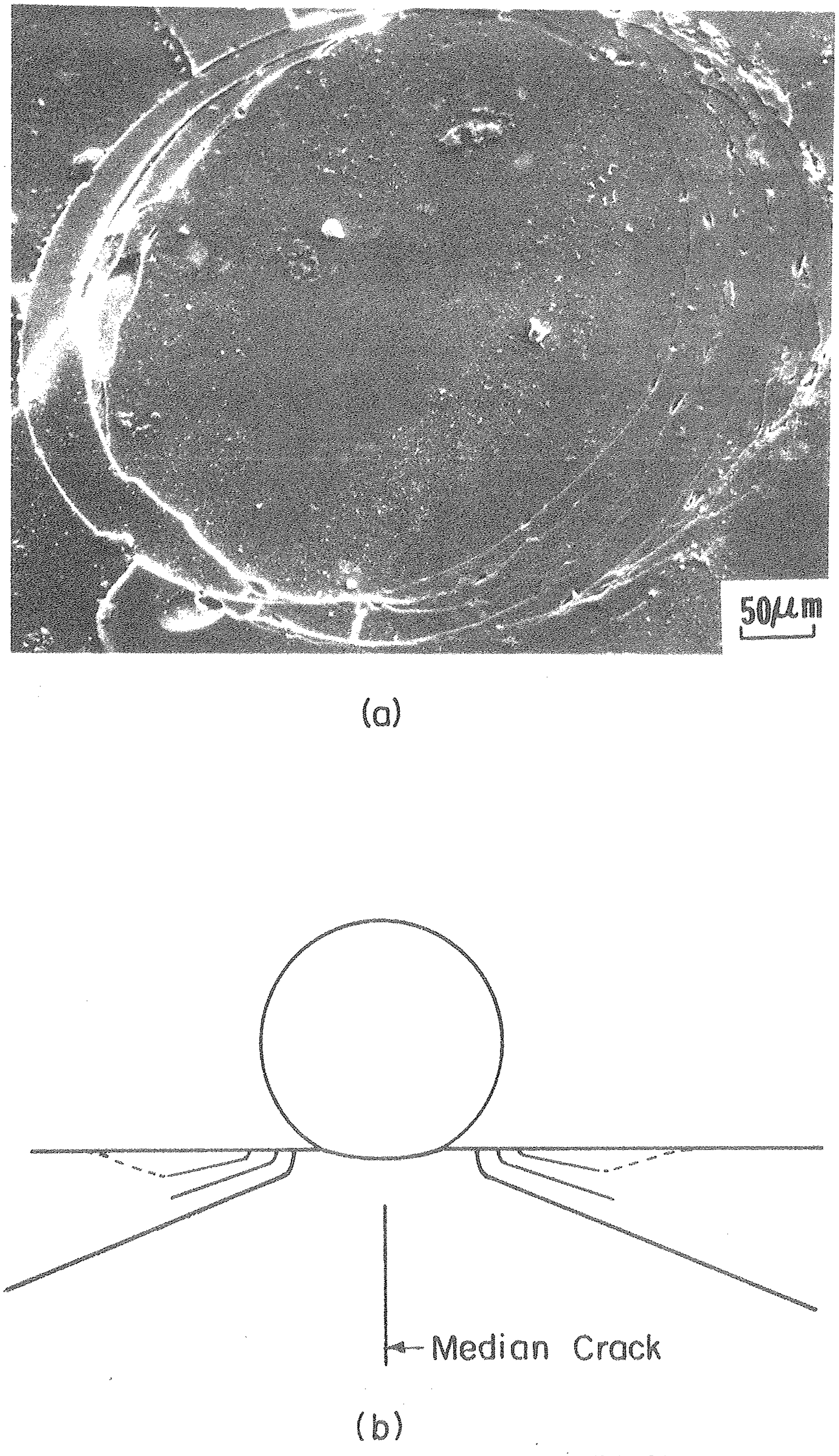

XBB 800-12929

Fig. 3.5. (a) Surface appearance of ring cracks on glass, (b) A schematic view of the cracks in cross-section. The median crack forms at a much higher load than that at which the ring cracks form.

comparable with or larger than the contact radius, a. For stable crack propagation, the direction in which the crack extends under a general state of stress has been discussed extensively in the literature. The three most plausible explanations which can be shown to lead to virtually identical predictions are:

1. The crack grows to maximize the energy release rate.

2. The crack grows in a direction normal to the maximum hoop stress $\sigma_{\theta\theta}$ at its tip.

3. The crack grows in such a way as to maintain pure mode I loading at its tip.

These arguments are based upon isotropic materials and would have to be modified for anisotropic materials such as single crystals. For Hertzian loading, the crack follows a path quite close to the trajectory normal to the maximum tensile stress in the uncracked solid. Since "exact" calculations of the crack path require time-consuming step-by-step calculations, it may be convenient to assume that the Hertzian crack follows the trajectory associated with the smallest principal stress σ_{33} in the solid prior to cracking. Also, as shown schematically in Fig. 3.5b, some other shallow cones will form outside the principal cone. These cones, which appear to also follow the σ_{33} trajectories, are seen as ring cracks on the surface, Fig. 3.5a. Increasing the indenter load propagates all cones further down, until one of the shallower cones suddenly propagates to the surface. The resulting surface failure is shown in Fig. 3.6. This type of failure has also been observed to occur during unloading.[21]

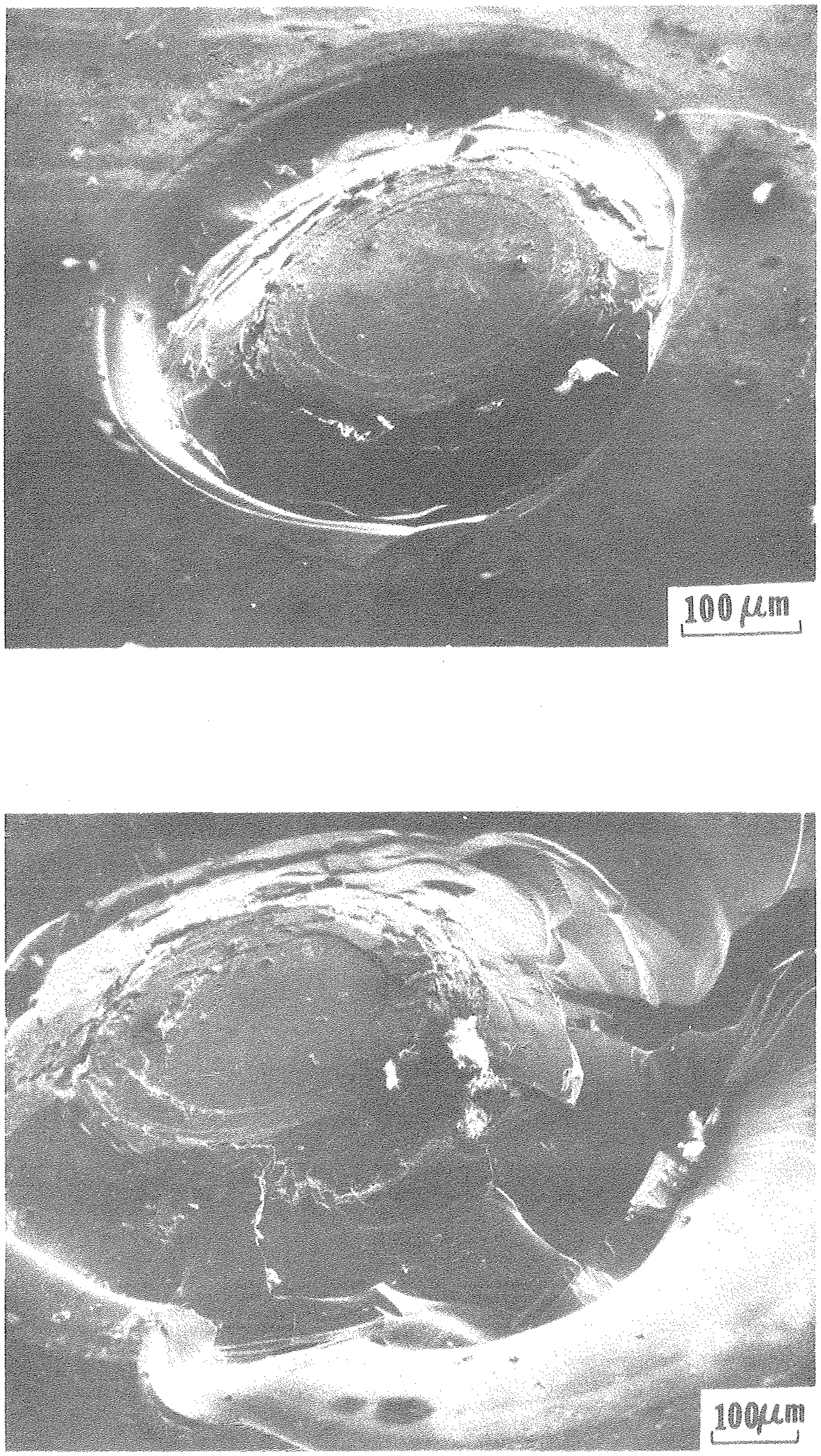

XBB 807-8904

Fig. 3.6. Surface failure produced in glass by increasing the indenter load beyond that for initial cone crack formation.

From the Hertzian analysis, it is expected that the critical load P_c for initiation of a cone would be proportional to the square of the indenter radius R if initial fracture occurs at a critical tensile stress. However, experimentally it has been found that for smaller indenters the relation between P_c and R is close to linear, while for larger indenters, load is approximately proportional to the radius squared, as shown in Fig. 3.7. The radius at which this transition occurs is typically between 1-3 cm for glass. This discrepancy between experiment and theory points out the fact that for prediction of fracture the knowledge of stresses in the elastic stress field is necessary but not sufficient. Clearly, the simple maximum tensile stress criterion is inadequate. This topic is further discussed in Chapter 4.

For the limiting case of a true cone, $c > 2a$, the mechanics of fracture becomes independent of the events within the contact zone (i.e., surface condition and location of fracture), as seen in the simple equilibrium relation obtained by Roesler,[3]

$$c_c = [F(\nu)\ P^2/K_{Ic}^2]^{1/3} \tag{3.1}$$

where $F(\nu)$ is a dimensionless constant involving only Poisson's ratio.

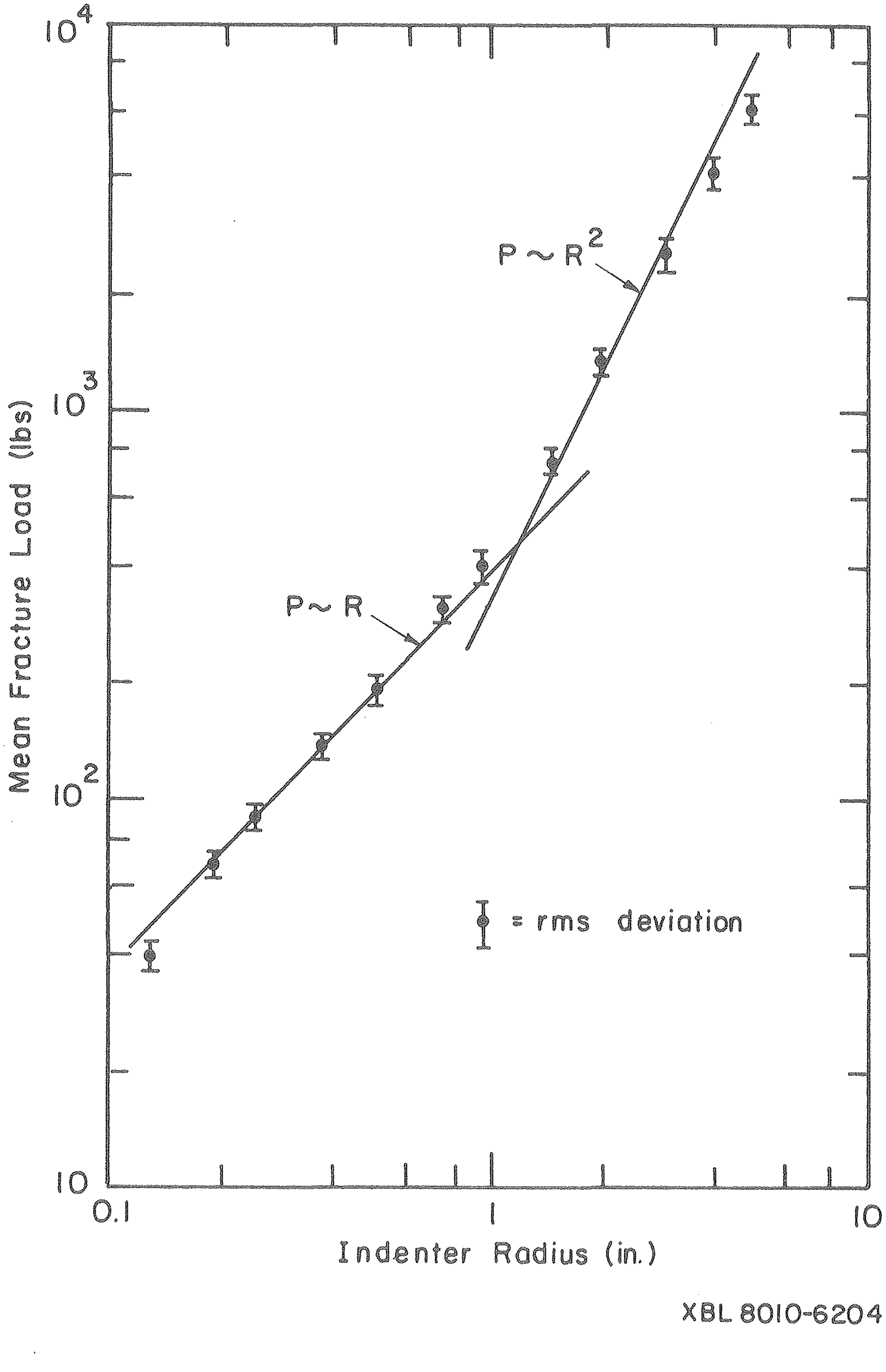

Fig. 3.7. The effect of indenter radius on the force required to produce a ring crack.[50]

The preceding discussion relates to the classical cone cracks that are observed to form during elastic contact. A similar type of cone cracking may occur even when the surface has responded plastically to the loading. Multiple cone crack formation in glass due to indentation by the spherical tip of a Rockwell C hardness tester is shown in Fig. 3.8a. The schematic representation of these cracks as also observed by Evans et al.[22] in ZnS impacted by WC and glass projectiles is shown in Fig. 3.8b. These cracks, unlike those forming during the elastic contact from a preexisting surface flaw, initiate most likely from deformation induced flaws. The formation and extension of these cracks does not appear to be as predictable as the elastic case. The stresses responsible for the formation of these cracks are discussed in Section 3.6.

3.4. Median Vent and Radial Cracks

The effect of increasing the indenter load beyond that at which the cone crack suddenly appears is to further extend the developed cone and, as the result of the increasing stress level, to induce and expand a zone of plastic deformation immediately below the contact area where shear and hydrostatic compression stresses are greatest. This behavior is more pronounced in materials with lower hardness or higher fracture toughness. From the bottom of the plastic zone where the stresses apparently become tensile, a system of penny-like (circular) cracks evolve once some threshold is reached in loading.[23,24] These are known as median or median vent cracks. Because plastic deformation occurs more readily under a sharp indenter than a sphere, median

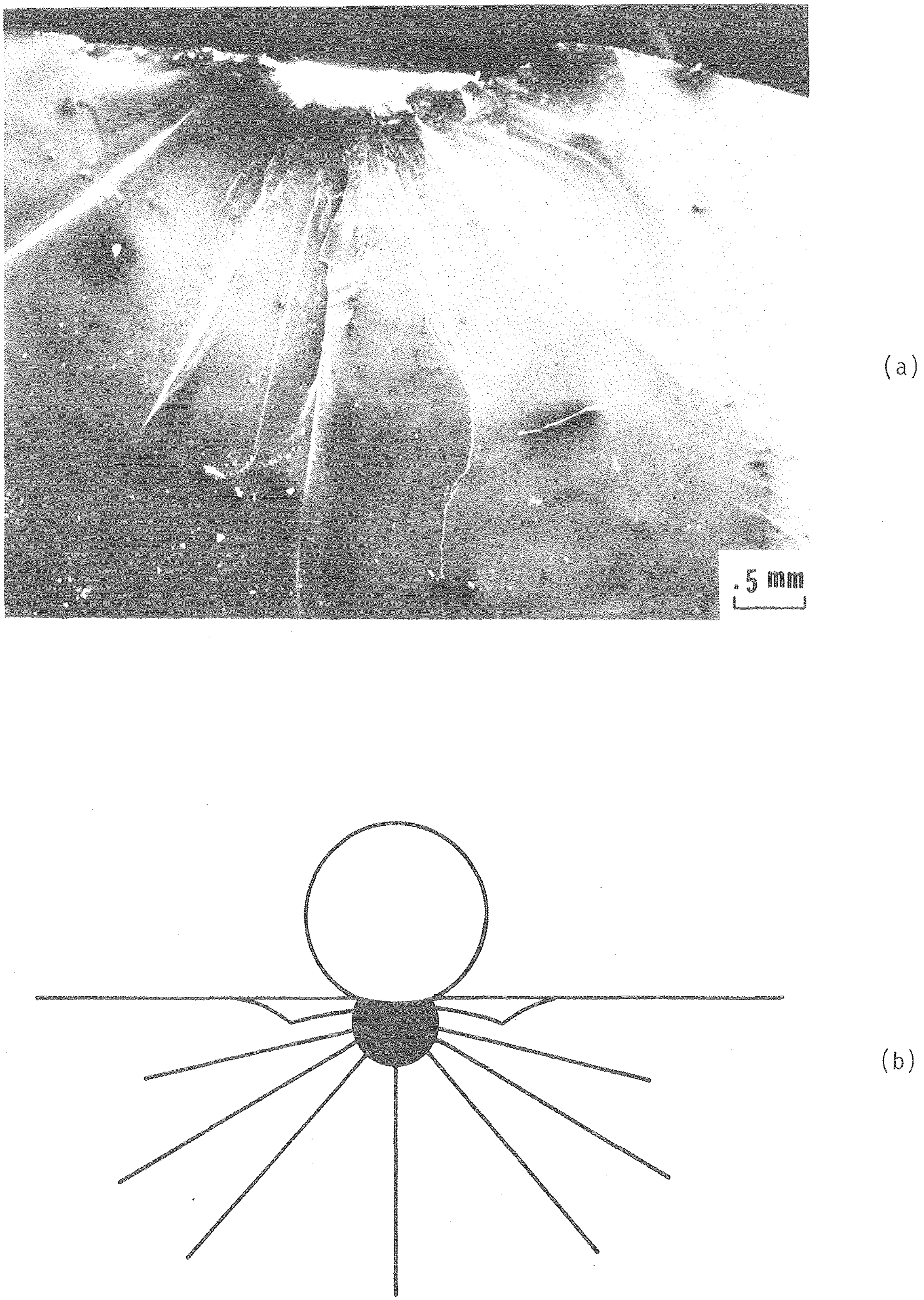

XBB 800-12928

Fig. 3.8. Formation of multi cone cracks when a surface plastically deforms under a Rockwell C hardness indenter.

cracks are usually studied using sharp indenters. They form on symmetry planes containing the load axis and line up with the diagonals of the indentation produced by pyramid indenters.

These cracks, as schematically shown in Figs. 3.9 and 3.10 for a sharp indenter, are circular and lie below the surface. With increase or removal of load, they extend without much downward propagation to reach the surface and eventually become semicircular. In this configuration they are usually referred to as radial cracks. Lawn and Marshall[33] observed the sequence of formation of these cracks on glass with a Vickers hardness tester for loads in the range of 20-150 N (4.5-33 lb). Their observations reveal that at higher loads median cracks break through the surface prior to unloading, while at lower loads cracks do not reach the surface until unloading.

Depending on the material properties, it is conceivable that median cracks may occur either before, during, or after propagation of a cone crack. Usually because of lower stresses at the locations where these median cracks form, surface cone cracks tend to form first. But if cone formation could be somehow prevented or delayed, an increase in load with consequently higher stresses may lead to the initiation and propagation of a median crack before or during cone formation. As will be shown, for a given particle radius and surface fracture toughness there should exist a specific range of surface flaw sizes that grow to form the cone crack. If these flaws are absent or are removed by polishing or etching the surface, cone cracks would start from any other smaller or larger flaws at higher loads. This might be

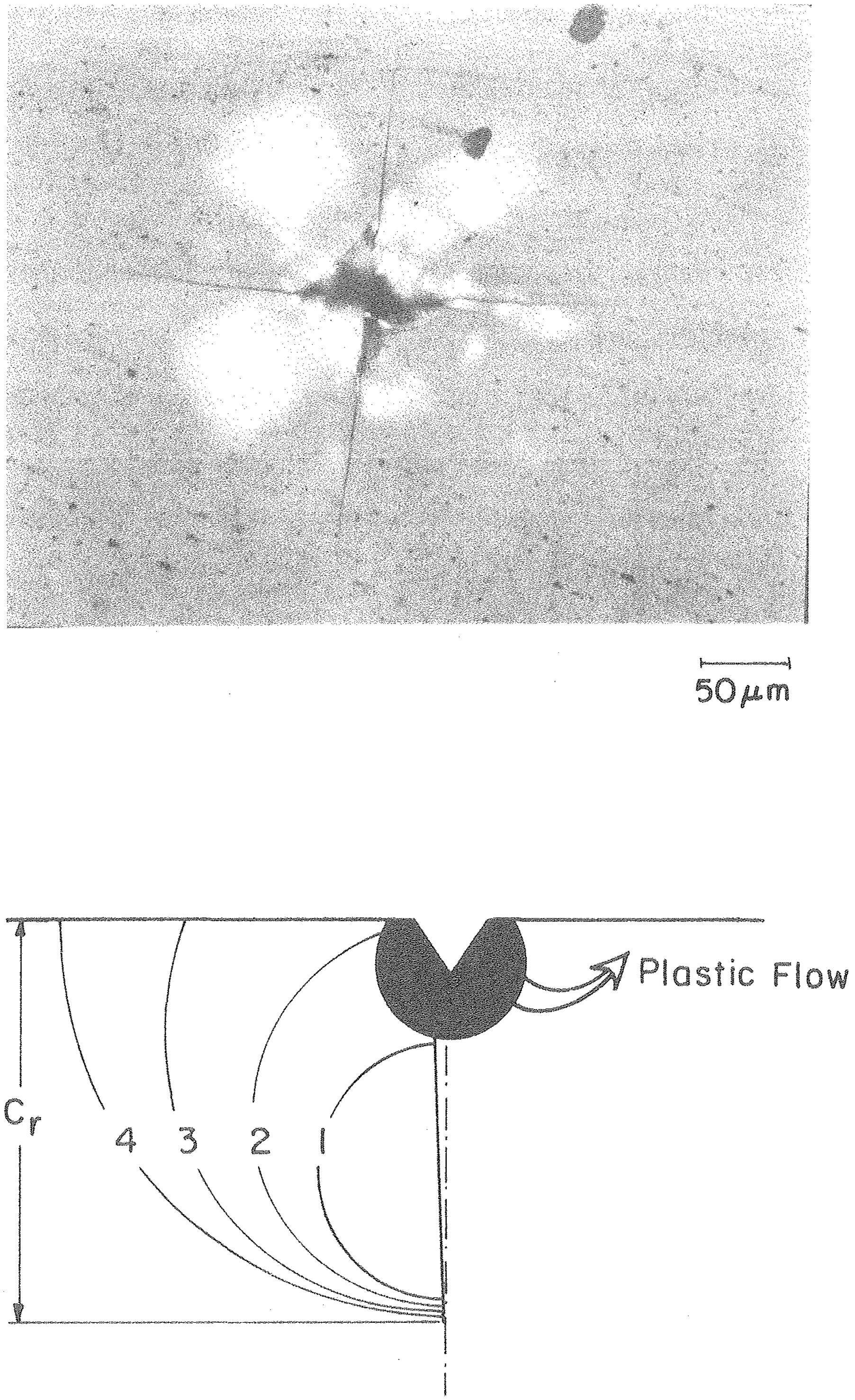

XBB 800-12927

Fig. 3.9. (a) Indentation impression by Vickers hardness tester and the resulting radial cracks on glass. (b) Schematic view of progressive extension of a median crack (1) to final radial crack (4) upon unloading.

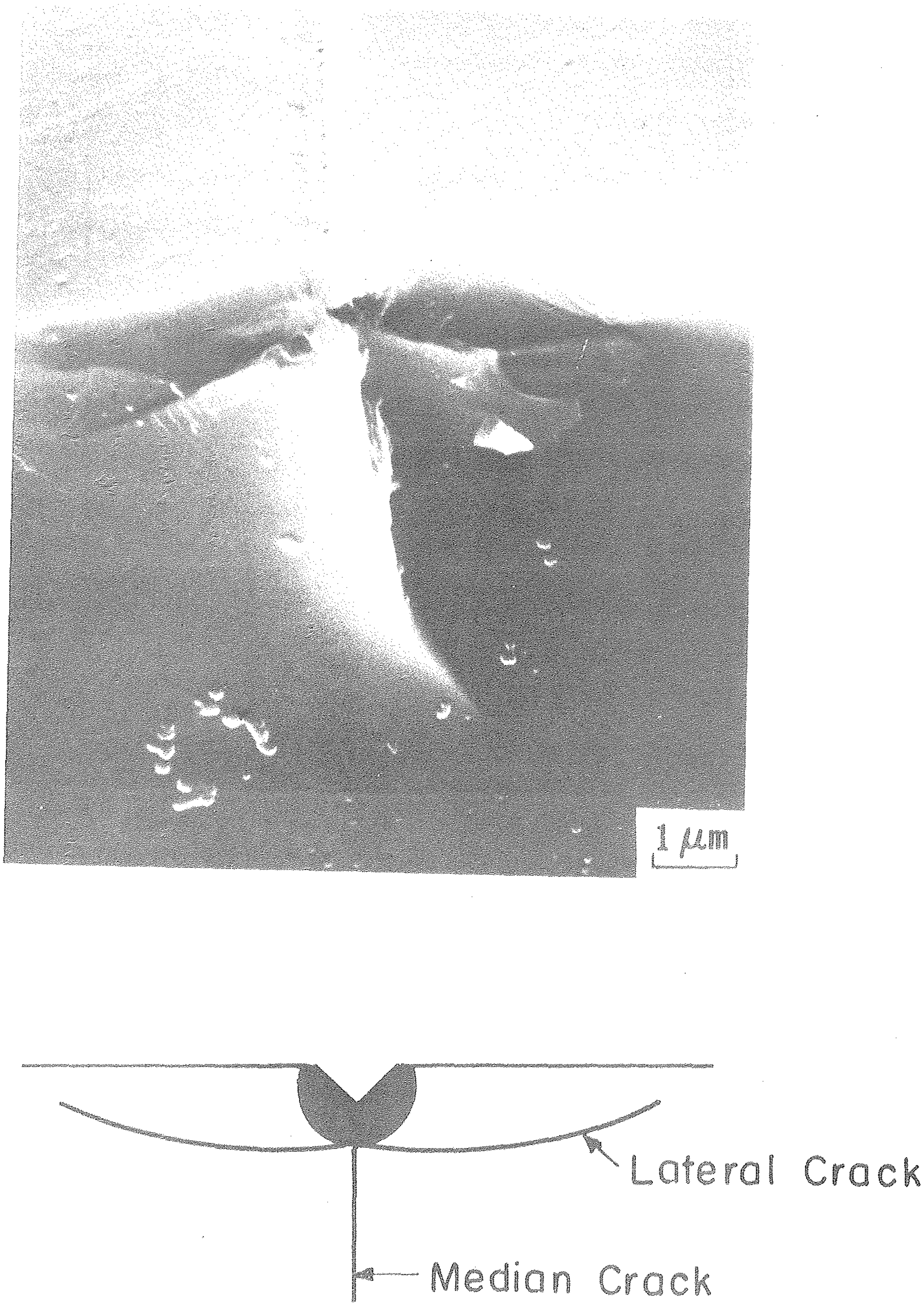

XBB 800-12926

Fig. 3.10. Formation of lateral and median cracks by indentation or scribing using a sharp tool. Photograph courtesy of Dr. A. Misra.

sufficient to propagate a median crack from a favorably sized or oriented flaw underneath the contact area before a cone crack starts. Again, because of rapidly diminishing tensile stresses below the surface, median cracks are more likely to form during overloading after formation of the cone.

Photographs by Lawn and Wilshaw[24] of indentations produced on an as received soda lime glass by a $R = 0.5$ mm ball, show that even though cone cracks may form with loads as low as 10 N, median vent cracks do not form until loads exceed about 140 N. At these loads, the cone extension rate decreases while plasticity, crushing, and the median crack propagation rate increase.

Since plasticity reduces the magnitude of the surface radial tensile stresses, the trend of cracking shifts from cone to median. These stresses are reduced the sooner the plastic zone forms and the larger its extent. For instance, in less brittle materials like hard metals, PMMA, or brittle ceramics at elevated temperatures the median crack system tends to begin operating before the cone has had a chance to develop at all. In these situations a combination of cone and radial cracks may form.

No Hertzian cone (initiating from the surface) forms when pointed or sharp indenters are used. The largely triaxial compressive stresses inhibit fracture, while shear stresses plastically deform the area around the contact site. The impression made by indenters such as cones, pyramids, or wedges are geometrically similar. Thus, the mean pressure is independent of the size of the indentation. Because of this the intensity of the stress field outside the plastically deformed area which is controlled by the contact pressure (hardness), remains independent of the impression size. However, the spatial extent of the stress field increases with the size of the indentation. The growth of the stress field with load P increases the chance of finding a flaw of more favorable size and orientation. It also increases the possibility of propagating larger flaws. So, at some critical load, P_c, a preexisting or deformation-induced crack will experience such tension over a sufficient portion of its area that an instability in crack size occurs. Evans et al.[22] obtained the following expression for P_c:

$$P_c \sim \frac{K_{Ic}^4}{H^3} \tag{3.2}$$

where K_{Ic} and H are the surface fracture toughness and hardness, respectively, and the proportionality factor is to be determined empirically for a given combination of indenter and surface. While Eq. (3.2) only indicates the role of hardness and fracture toughness in the median crack formation process, P_c due to its dependence on flaw sizes might have a statistical variation rather than being constant. However, experimental studies by Weiderhorn et al.[23] show a very small variation in strength degradation due to the median vent cracks produced by sharp indenters. This indicates that sharp indenters, through the deformation process within the plastic zone, produce their own incipient flaws. This is consistent with Lankford's[19] observation that pointed indenters create a large volume of micro-cracks in alumina by twinning. On the other hand, elastic interaction with blunt indenters necessitates a search for a suitable starting fracture nucleus on the target surface, and consequently a larger variation in fracture load.

After initiation, these median crack propagate to the surface in the form of radial cracks (Fig. 3.9). The radius, c_r, of these semicircular radial cracks increases with the size of the contact radius or diagonal, a, where a is related to the mean contact pressure, p_m, through the following relations,

$$p_m = P/\pi a^2 = H \qquad \text{(circular contact)} \tag{3.3}$$

However, this mean load is subject to variation with the indenter apex angle and friction. The apex angle at which maximum mean pressure occurs depends on the test material, and may lie anywhere from 60–150°. Usually, higher angles for maximum mean pressure are approached when more ductile materials are used. Conversely, hard materials favor a sharper indenter for maximum contact pressure.[27,59] Friction amplifies the magnitude of contact pressure and its effect becomes more pronounced for more acute angles.[29] But since impressions for a given apex angle caused by cones or pyramids are geometrically similar for dimensional reasons, it could be argued that the resulting cracks should also be geometrically similar. This means that the size of radial cracks should be proportional to the contact radius. But due to the work hardening character of most materials, mean pressure increases when large loads are applied and consequently large deformation is caused.[29] It should be noted that this possible small increase in p_m happens after the initial drop in the apparent hardness due to complete development of the plastic zone under the indenter. From Eq. (3.3) this means that a grows more slowly with load P. But, the magnitude of the residual stresses responsible for radial crack formation remains high, after removal of the load because of the high yield strength of these materials. Therefore, the ratio of c_r/a is expected to increase slowly with load or equivalently with a. Lawn and Fuller[30] obtained the following empirical relation for the radius of a radial crack in terms of indentation load,

$$c_r \sim \left(\frac{P}{K_{Ic}}\right)^{2/3} \tag{3.4}$$

Substituting P from Eq. (3.3) into Eq. (3.4) gives

$$\frac{c_r}{a} \sim a^{1/3}\left(\frac{p_m}{K_{Ic}}\right)^{2/3} \tag{3.5}$$

This equation also indicates that the normalized size of the radial cracks increases with the size of impression in two geometrically similar indentations.

Evans and co-workers[31,32] formulated two semi-empirical relations between the magnitude of radial cracks and the relevant target and projectile parameters. For $c_r/a > 2$, they obtained the following approximate proportionality,

$$c_r \sim \frac{P^{1/2}}{H^{1/4} K_{Ic}^{1/3}} \tag{3.6}$$

P in the above equation can be replaced by appropriate parameters[32] to represent the impact load in low-velocity impacts where damage morphology is very close to the quasistatic indentation,

$$c_r \sim R\ G^{0.2}\ V^{0.6}\ \rho^{0.3} /\ K_{Ic}^{0.33}\ H^{0.25} \tag{3.7}$$

where G is the target shear modulus and V and ρ are projectile velocity and density, respectively.

For high-velocity impacts where dynamic effects become significant, they found,[22]

$$c_r \sim \gamma\ (RV)^{1.33} / K_{Ic}^{0.66} \tag{3.8}$$

γ is a parameter that has a weak dependency on both the acoustic impedance and the density of particle and target. Comparison of Eqs. (3.7) and (3.8) indicates that the effect of velocity and fracture toughness become more pronounced in high-velocity impacts, due to the increase of dynamic effects.

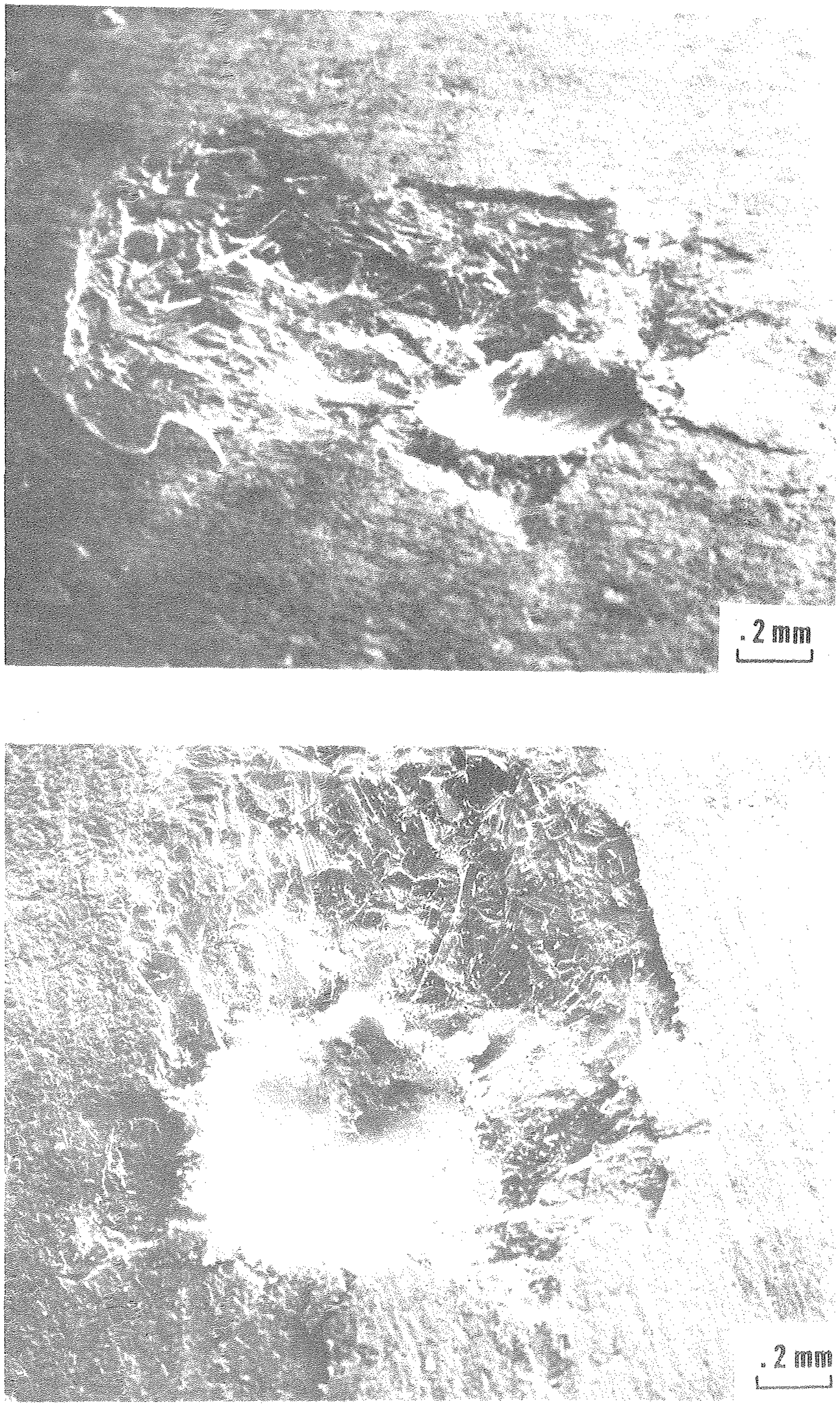

XBB 800-12925

Fig. 3.12. Surface failure of MgO during loading by a Rockwell C hardness tester.

clear that the surface is bent upward around the contact area. These cracks, unlike those forming on unloading as shown in Fig. 3.10, initiate and propagate from the sides of the plastic zone rather than from the bottom of it.

For low-velocity impacts, it is more appropriate to put the emphasis on analyzing the low-load indentation case. The sequence of all the cracking that occurs under this condition, as observed by Evans and Wilshaw,[32] is shown in Fig. 3.13. it is apparent that the driving force behind the formation and propagation of the lateral and radial cracks are the residual stresses caused by the mismatch between elastic and plastic regions. Analysis toward prediction of the size of these cracks requires detailed knowledge of the plastic zone and the stress distribution around it. This topic is discussed in the next section.

Evans and Wilshaw[32] from their semi-empirical approach found the following proportionality for the lateral crack size under quasi-static conditions,

$$c_l \sim \left(\frac{P}{K_{Ic}}\right)^{3/4} \quad , \quad \text{for} \quad c_l/a > 2 \qquad (3.9)$$

3.6. Elastic Plastic Analysis

The equations describing elastic behavior are exact and well-established. Many analytical solutions have been obtained for simple configurations, but more complicated situations require numerical

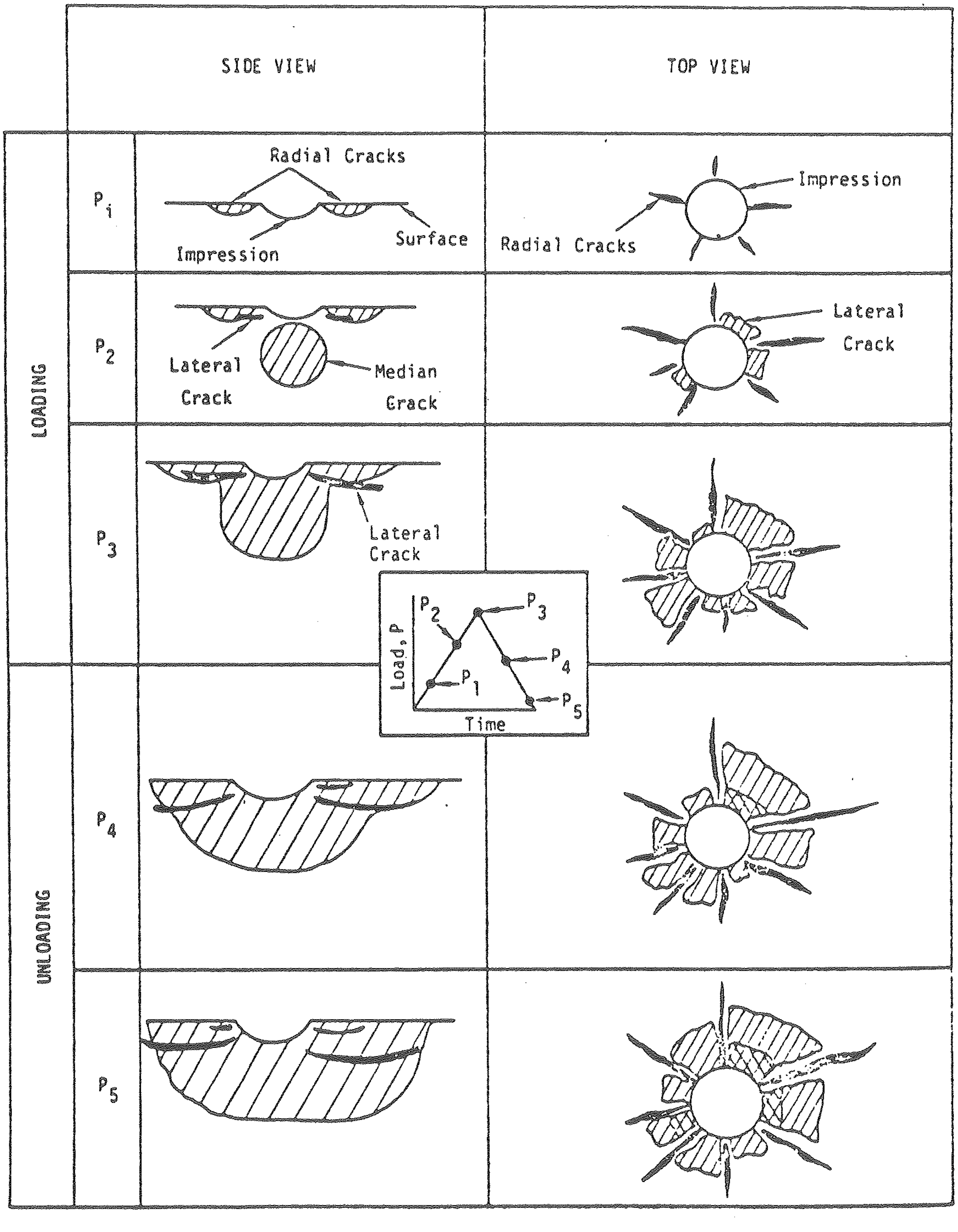

XBL 8010-12568

Fig. 3.13. Schematic of crack formation and growth during loading and unloading by small spherical indenters when the surface plastically deforms prior to fracture.[32]

solutions. A somewhat similar situation exists when the plastic components of strain are large compared to the elastic components, but not so large that dimensional changes must be considered. Reasonably accurate constitutive equations are available. Closed form solutions exist for a few simple problems, but in most cases numerical solution is again required. In problems which require consideration of both elastic and plastic components of strain, only a few very simple problems are amenable to a closed form solution. Because of the time-consuming and complicated nature of the computations, approximate solutions are often used. For the problem of interest in this work, the stress state under an indenter, it is important to consider both elastic and plastic components of strain.

In this section some idealizations have been used to find the stresses responsible for the formation and propagation of cracks when elastic and plastic deformation occurs. One of the goals is to determine whether crack propagation coincides with prior principal stress trajectories. If it does, the effort for obtaining a relation between the applied load and crack propagation would be greatly reduced.

As a first step toward modeling the plastic deformation in order to find the stresses in the elastic zone where cracking occurs, it is necessary to check the shear stresses responsible for such deformation. The validity of a model can be assessed by its ability to predict the location of the different types of cracks. When the load is light, deformation beneath the indenter will be elastic and the Hertzian theory will pertain. Figure 3.14 shows the distribution of normal

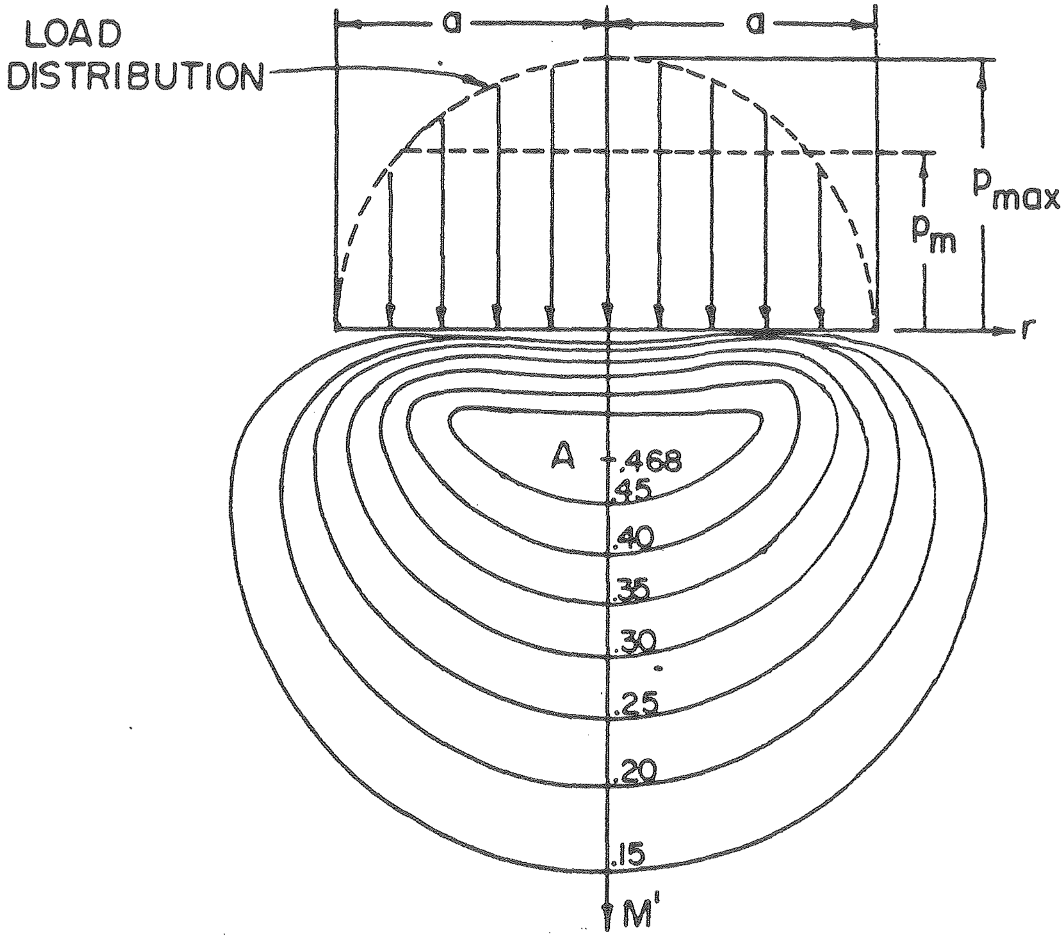

XBL 8010-12305

Fig. 3.14. Lines of constant maximum shear stress (τ/p_m) for a smooth spherical indenter given by the Hertz solution.

stresses on the area of contact obtained by Hertz and the resulting lines of constant shear stress. Numbers designate the normalized values of the local shear stress τ with respect to the mean contact pressure p_m, τ/p_m. According to the Tresca yield condition, plastic flow occurs first at point A when $\tau = S_y/2$, where S_y is the uniaxial flow stress. Substituting the normalized value of shear stress at point A from Fig. 3.14 into the above yield condition gives,

$$p_m = \tau/0.468 = S_y/2(0.468) = 1.07\ S_y \tag{3.10}$$

So, first yielding occurs when p_m is 7 percent higher than the yield strength. As the load is increased, the plastic zone will expand in all directions from point A. Eventually, for a non strain hardening material the surface contact pressure becomes uniform, resembling indentation by a punch, when the entire contact area is plastic. However, due to strain hardening a uniform pressure distribution is never reached, since strains are largest in the center and diminish toward the edge of the contact area. Nontheless, the concept of uniform pressure is a convenient idealization which should not be far from reality. At this stage the problem is similar to a hardness test in which

$$p_m = CS_y \tag{3.11}$$

where C, the constraint factor, depends on the indenter apex angle and the surface elasticity. Experiment and analytical results show that C increases with apex angle. Hill, et al.,[36] with the assumption of rigid-plastic behavior found that for a wedge with a semi-angle of 90°, i.e., when the wedge becomes a flat punch, the indenter pressure was about 2.6 times the pressure at zero angle. For a square flat punch, Shield and Ducker[37] using limit analysis obtained a value of 2.855 for the constant factor C, while Levin[38] studying the flat circular punch reported a value of 3.0. A value of 3.0 is also found for the spherical indenter,[29] which shows the similarity in constraint provided by the surrounding elastic materials when using these different identers.

Marsh[40] showed that the "elasticity" of the surface, defined as the ratio of yield strength S_y to modulus of elasticity E, can influence the constraint factor C. The value of C increases with decreasing S_y/E until it reaches a limiting value of 3.0. For example, for glass, which has a high value of S_y/E, C lies between 1.5-2.0. The result is similar to that obtained in indenting a more ductile material with a sharper indenter.

Mulhearn's[41] picture of deformation associated with the indentation made in hardness testing by a pyramid identer and the study of Kobayashi et al.[42] suggest that the indentation process can be modelled by an expanding spherical cavity. The expansion of the plastic zone produced by increasing the load from the elastic limit, P_e, to $P = 40\ P_e$ as calculated by Hardy[55] is shown in Fig. 3.15. Despite significant changes in stress distribution that occur due to plastic flow, the boundaries of this expanding cavity match very closely the constant shear stress contour lines of the elastic solution as shown in Fig. 3.14. From this type of observation Shaw et al.[43] showed that, by knowing the constraint factor C, the location of the elastic-plastic boundary can be easily approximated. Rewriting Eq. (3.11) as

$$p_m/S_y = p_m/2\tau = C \qquad . \tag{3.12}$$

This expression gives the contour line τ/p_m close to the elastic-plastic boundary. For C = 3, when full plastic deformation has occurred, the elastic plastic boundary would be close to the constant shear stress line with the value of 0.17. Even though this method of estimating the boundary is far from rigorous, it appears to provide reasonably accurate predictions.

The solution for the expansion of a spherical cavity by internal pressure is known, Hill.[44] However, it cannot be applied to this problem where only a partial sphere exists. For this reason, in the present work, to obtain an approximate solution an axisymmetric finite element program was used to calculate the stresses outside the plastic zone.

As shown in Fig. 3.16a, a uniform pressure is assumed to act on the elastic-plastic boundary. Since the boundary is not a complete sphere, the vertical component of the resultant force due to the boundary pressure is equal to the applied load, while the resistance

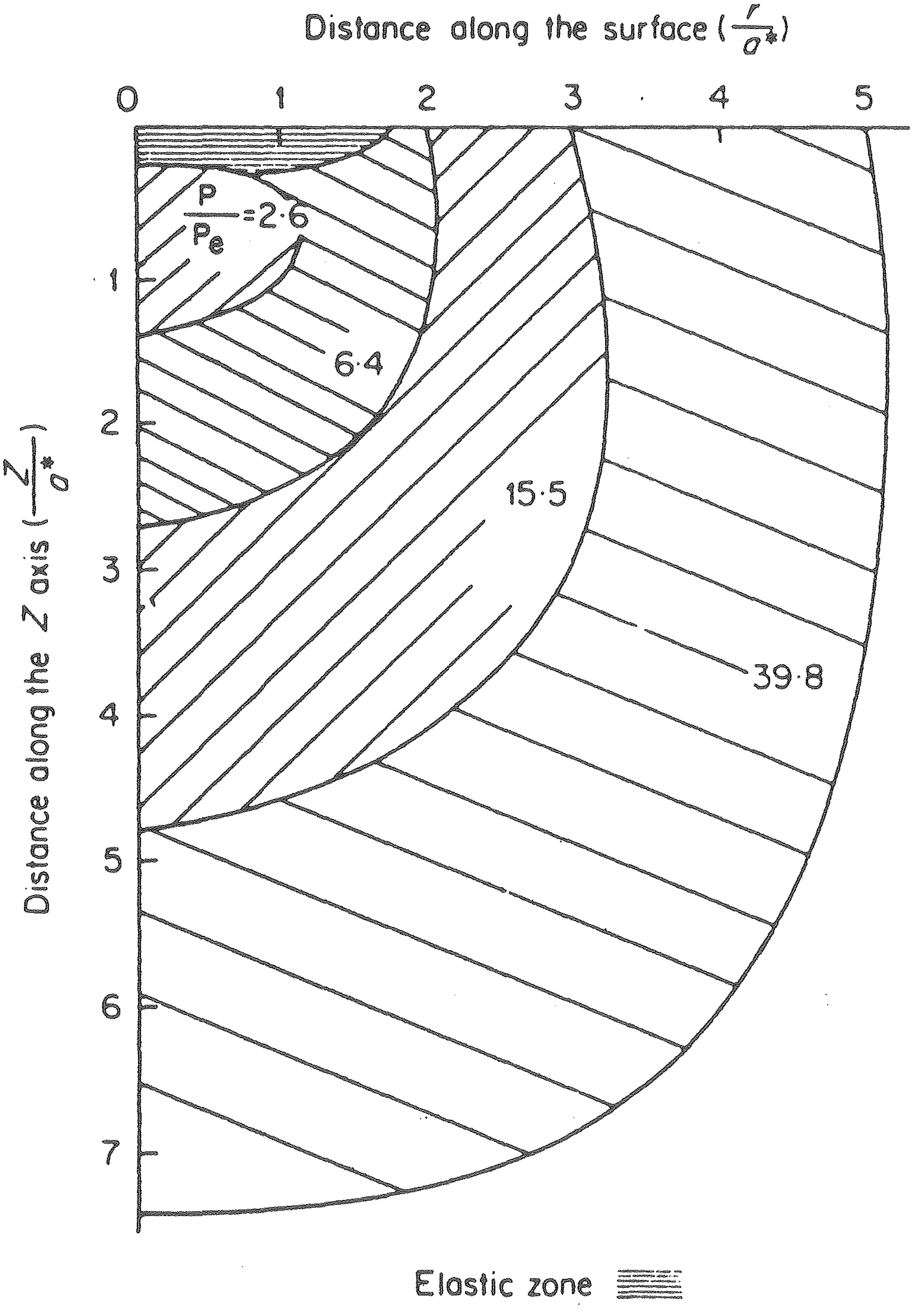

XBL 8010-12304

Fig. 3.15. Progressive yielding of the half space under loading by a sphere. z is the coordinate axis in the direction of the normal load P.[55] a* is contact radius prior to plastic deformation.

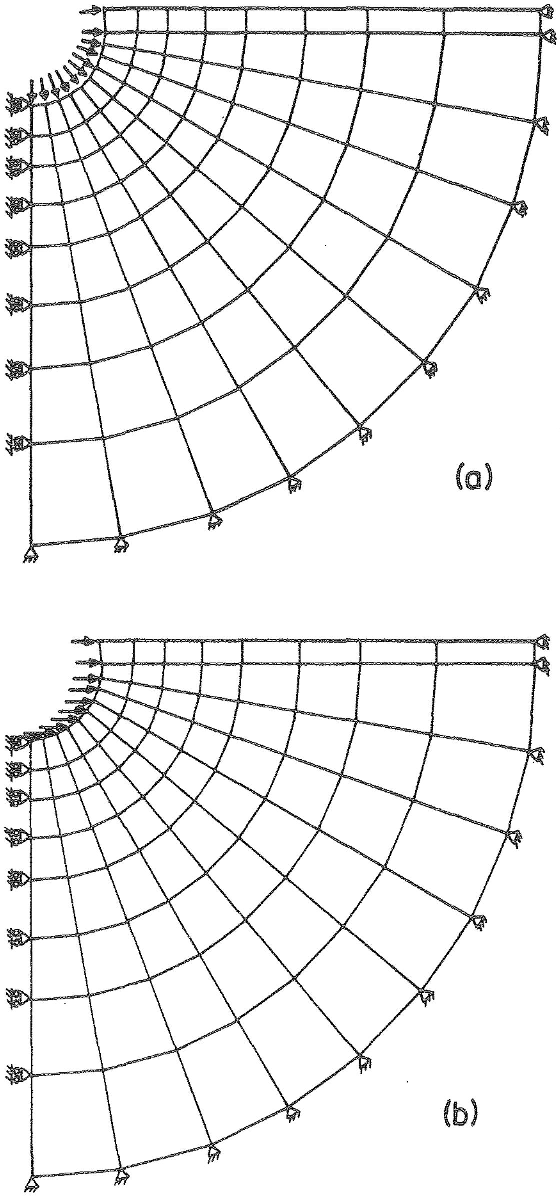

XBL 8010-6208

Fig. 3.16. Boundary conditions at the elastic plastic interface for (a) the spherical cavity expansion, (b) unloading after plastic deformation.

to the horizontal component is provided by the surrounding elastic material. The resulting principal stress trajectories and the magnitude of the largest principal stress σ_{11} are shown in Fig. 3.17 for an internal pressure of 250 Ksi (1.81 Gpa). From these figures it is apparent that the highest stress occurs at the bottom of the elastic-plastic boundary. This is the location at which median vent cracks initiate. They then propagate down along the σ_{22} trajectory, which contains the axis of symmetry, as shown in Fig. 3.10.

Crack initiation will depend on both the stress and the size of the starting flaw. Because of this it is possible that a crack will also initiate from flaws, most likely deformation induced, at some other locations along the elastic-plastic boundary where the stresses are lower. These then would be the starting points for conical-type cracks that are observed to form in situations such as that shown in Fig. 3.8. Comparison of Figs. 3.8 and 3.17b indicates that these cracks, like the median vent, follow the prior principal stress trajectories very closely.

If the load is now removed, elastically displaced material will try to move back to its original location. This would be possible if the contact had been completely elastic. However, in the elastic-plastic case this recovery is resisted by the plastically deformed material. In ductile materials the force exerted by the plastic zone will cause a second plastic flow to occur upon unloading.[43] On the other hand, brittle materials upon unloading respond by fracturing at high tensile stress locations before any reversed plasticity occurs.

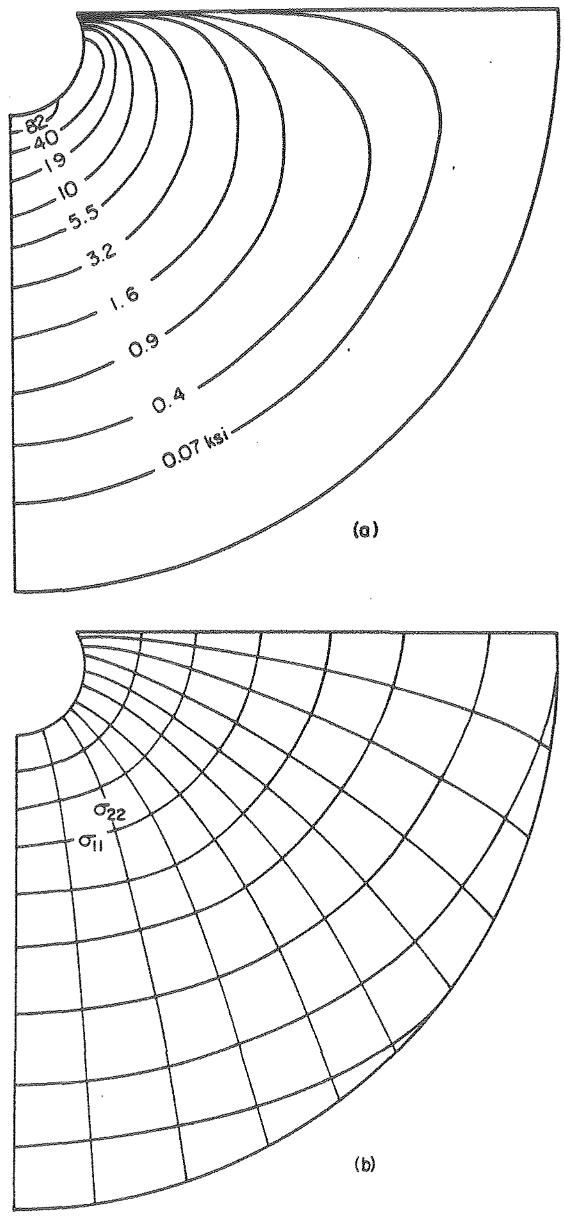

XBL 8010-6209

Fig. 3.17. (a) Magnitude of the maximum principal stress (tension) σ_{11} and (b) trajectories of σ_{11} and σ_{22} for spherical cavity under 250 ksi internal pressure.

As mentioned in the expanding cavity concept, the resulting force due to the vertical component of the stresses on the elastic-plastic boundary is equal to the external load. Removing the load results in unbalanced internal forces. Ideally, in order to compensate for this, all the vertical components of the stresses on the elastic-plastic boundary are removed. Horizontal stress components may change somewhat in magnitude but do remain because the resulting force is internally balanced. This idealized loading is shown in Fig. 3.16b and the resulting magnitude and trajectories of the principal stress σ_{11} are plotted in Fig. 3.18.

Comparison with the expanding spherical cavity problem (Fig. 3.17) shows that the direction of σ_{11} below the plastic zone instead of being parallel is perpendicular to the surface. Also, its magnitude reduces more slowly with depth. These σ_{11} stresses are those responsible for lateral crack formation from the bottom of the elastic plastic boundary, as shown in Fig. 3.10. But since these cracks after propagation effectively separate the plastic zone from the material below it, the stress distribution changes drastically. Therefore, their propagation cannot be predicted from the prior stress trajectories, and would have to be calculated in a stepwise manner, which is by no means an easy task.

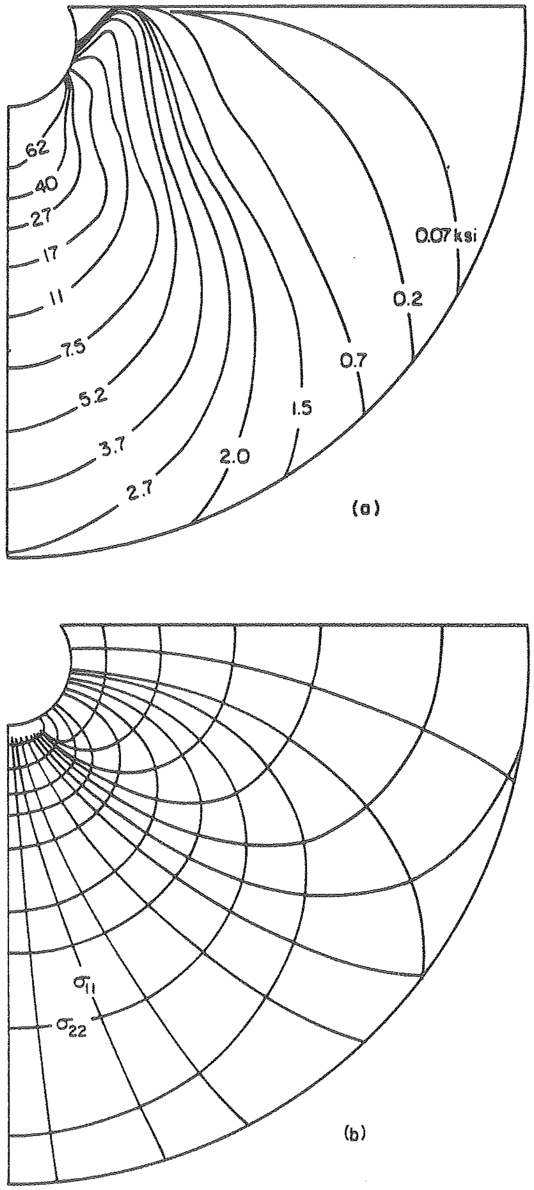

XBL 8010-6210

Fig. 3.18. (a) Magnitude of the maximum principal stress (tension) σ_{11} and (b) trajectories of σ_{11} and σ_{22} upon unloading.

4. INDENTATION OF BRITTLE (ELASTIC) MATERIALS BY SPHERICAL INDENTERS—A REVIEW OF PAST WORK

Hertz provided the solution for the localized stress field that results when spheres or cylinders contact one another or a flat surface and the material behavior is elastic. The solution for a sphere contacting a flat surface is useful in studying indentation or erosion due to relatively large blunt indenters.

Since the elastic stress field around the indenter is well-defined up to the point of fracture, many important surface properties such as residual stress, flaw densities, and size, as well as fracture toughness, can be evaluated from fracture tests once a method has been developed. Strictly speaking, the Hertzian stress field, even though invalid after crack propagation, has been used to estimate the extent of cracking that results from the elastic contact of a sphere with a brittle surface.[45] This has provided a way of estimating the strength degradation of ceramics due to impact.

When materials behave in a brittle manner, in either large-scale bend tests or small-scale indentation tests, their strength is determined by the ever-present flaws. These flaws may be characterized by a strength distribution function. Generally, the flaws are distributed throughout the volume of the material, but in glass they appear to be distributed only on the surface. However, in indentation tests, because the stresses decrease rapidly below the surface, fracture inevitably initiates from a surface flaw. Subsequent propagation of this fracture requires that the energy release rate at any stage be greater or equal to the critical value $_{Ic}$. Alternatively and equivalently, the stress intensity factor K_I must exceed or be equal to the plane strain fracture toughness K_{Ic}.

The cone crack produced by a spherical indenter can be seen easily in materials that behave elastically, at least prior to fracture. But ever since cone formation was studied by Auerbach[46] in 1891, the results have not agreed with the traditional concept that fracture in brittle solids should occur at a certain value of the maximum tensile stress. The aspects of this problem which have led to an extensive and contradictory literature are:

1. There is a "size effect" on strength such that the mean value of the maximum tensile stress in the material increases as indenter size decreases, as shown in Fig. 4.1.

2. The location of fracture, on the average, is not at the location of the maximum stress, as indicated in Fig. 3.4.

3. Both fracture load and fracture location, for a given indenter size, show a great deal of scatter.

In this chapter these aspects which have fundamental importance are examined critically and inadequacies in the present literature are pointed out. Based on this study a new approach is taken to explain the experimental results. This will be presented in the next chapter.

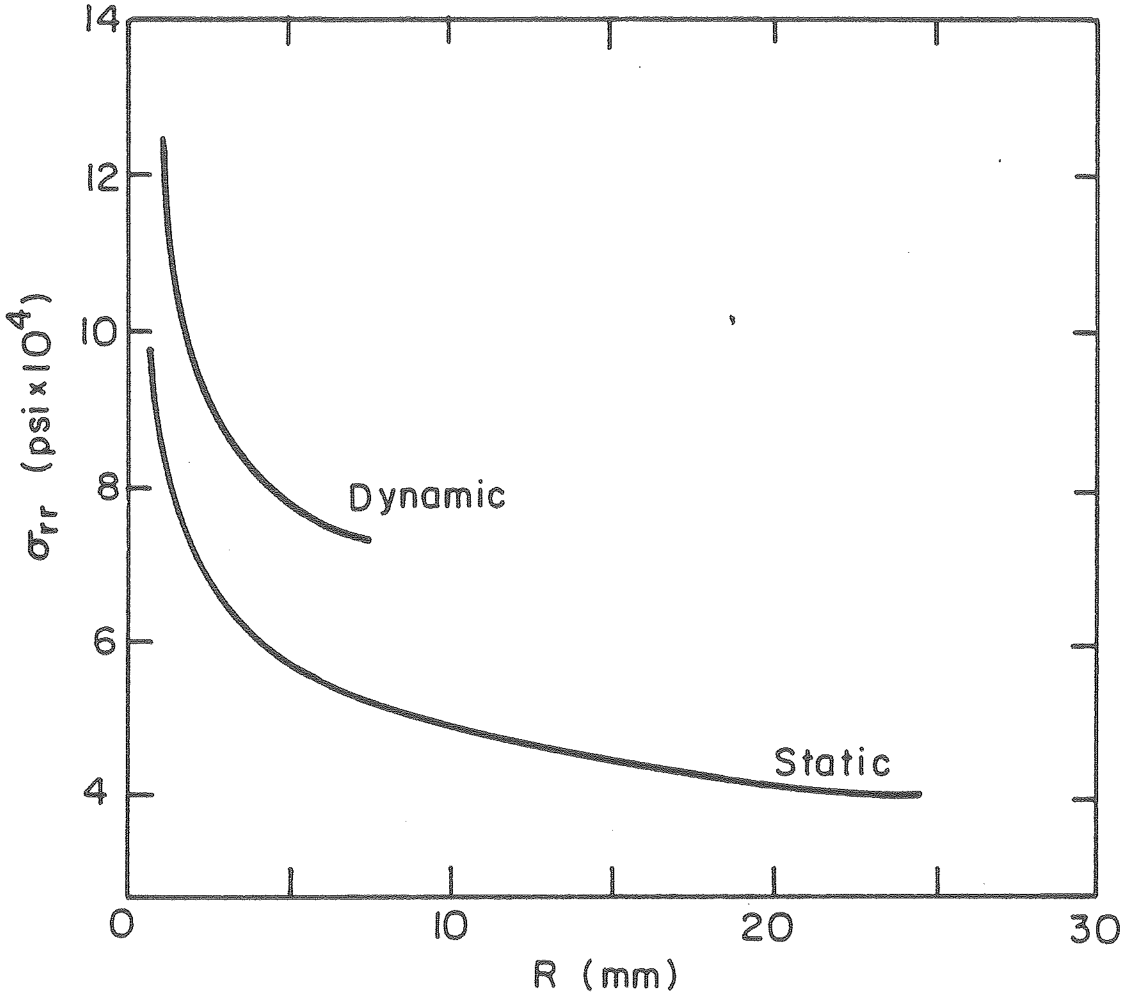

XBL8010-6211

Fig. 4.1. The variation of the mean value of σ_{rr}, the stress at the rim of the contact area, at fracture with the radius of the indenter.[50]

4.1. The Elastic Stress Field

When a spherical indenter or spherical particle is pressed against a plane (specimen), the

radius of the circle of contact a from the Hertzian theory can be related to the applied load P and sphere diameter 2R through the following relation:

$$a = (\lambda PR)^{1/3} \tag{4.1}$$

$$\lambda = \frac{3}{4}\left(\frac{1 - \nu_p^2}{E_p} + \frac{1 - \nu_s^2}{E_s}\right) \tag{4.2}$$

where E_p and E_s are the Young's moduli of the particle and surface, respectively, and ν_p and ν_s are the corresponding values of Poisson's ratio.

The distance of mutual approach of two bodies Z or penetration, in the case of a hard particle indenting a softer surface, from a simple geometric relation can be written as

$$Z = a^2/2R \tag{4.3a}$$

Eliminating a by using Eq. (4.1), a force-penetration relation will result,

$$Z = \frac{1}{2}\left(\frac{\lambda^2 P^2}{R}\right)^{1/3} \tag{4.3b}$$

Strictly speaking, Eqs. (4.1) and (4.3) are invalid after the initiation of fracture, but they can be used as an approximation for loads much higher than that at which the initial fracture occurred.[47] From the load-penetration relation, Eq. (4.3), the strain energy of the system can be written as,

$$U = \frac{(8RZ^5)^{1/2}}{5\lambda} \tag{4.4a}$$

Equivalently, by substituting for Z from Eq. (4.3b), U can be written as,

$$U = \frac{3}{10}\left(\frac{\lambda^2 P^5}{R}\right)^{1/3} \tag{4.4b}$$

The maximum contact load P_{max} produced under impact conditions, following the approach described by Timoshenko,[48] can be written as

$$P_{max} = \left(\frac{5\pi\rho}{3}\right)^{3/5} \frac{R^2 V^{6/5}}{\lambda^{2/5}} \tag{4.5}$$

where ρ and V are the particle density and velocity, respectively. Within the contact circle the applied load is distributed as a hemisphere of compressive stress, varying from a maximum of p_{max} at the center to zero at the periphery of the contact area, Fig. 3.14

$$p_c = p_{max}(1 - r^2/a^2)^{1/2} \quad , \quad r \leq a \tag{4.6}$$

p_c is the contact pressure at a radial distance r along the surface from the center of contact and

$$p_{max} = \frac{3}{2} p_m \tag{4.7}$$

where p_m is the mean contact pressure

$$p_m = \frac{P}{\pi a^2} \tag{4.8a}$$

using Eq. (4.1) to eliminate a, gives p_m as a function of load

$$p_m = \frac{1}{\pi \lambda^{1/3}} \left(\frac{P}{R^2}\right)^{1/3} \tag{4.8b}$$

The stresses in the rest of the body arising from the contact loading were obtained by Huber,[49] who extended the Hertz analysis and expressed the stress in the general form,

$$\sigma_{ij} = p_{max} F_{ij}(L, \nu_s) \tag{4.9}$$

where L is the location of the point of interest in the body. F_{ij} functions, as given in Appendix A, have very complex dependencies on the coordinates. The absolute value of all functions corresponding to principal stresses, $\sigma_1 > \sigma_2 > \sigma_3$, have a stationary value with respect to the z-axis along the surface at $z = 0$. The principal stresses on the surface ($z = 0$) where cracking always initiates, expressed in cylindrical coordinates, are[56]

$$\sigma_1 = \sigma_{rr} \quad , \quad \sigma_2 = \sigma_{\theta\theta} \quad \text{and} \quad \sigma_3 = \sigma_{zz} \quad .$$

For $r < a$.

$$\sigma_{rr} = -1.5\ p_m \left[\left(1 - \frac{r^2}{a^2}\right)^{1/2} + (1 - 2\nu_s)\ \frac{a^2}{3r^2} \left(\left(1 - \frac{r^2}{a^2}\right)^{3/2} - 1 \right) \right] \tag{4.10}$$

$$\sigma_{\theta\theta} = -1.5\ p_m \left[\left(1 - \frac{r^2}{a^2}\right)^{1/2} - (1 - 2\nu_s)\ \frac{a^2}{3r^2} \left(\left(1 - \frac{r^2}{a^2}\right)^{3/2} - 1 \right) \right] \tag{4.11}$$

$$\sigma_{zz} = -1.5\ p_m \left(1 - \frac{r^2}{a^2}\right)^{1/2} \tag{4.12}$$

for $r = a$.

$$\sigma_{rr} = p_m\ \frac{1 - 2\nu_s}{2} \tag{4.13}$$

$$\sigma_{\theta\theta} = -p_m\ \frac{1 - 2\nu_s}{2} \tag{4.14}$$

$$\sigma_{zz} = 0 \quad . \tag{4.15}$$

for $r > a$.

$$\sigma_{rr} = p_m\ \frac{(1 - 2\nu_s)\ a^2}{2r^2} \tag{4.16}$$

$$\sigma_{\theta\theta} = -\sigma_{rr} \tag{4.17}$$

$$\sigma_{zz} = 0 \quad . \tag{4.18}$$

The value of these stresses, from the foregoing equations, normalized with respect to p_m, are plotted in Fig. 4.2 for $\nu_s = 0.25$, which is a typical value for glass and Si_3N_4. It is apparent that among all stresses σ_{rr} is the primary stress responsible for the initiation of fracture from a surface flaw and consequent ring-and-cone crack formation. The other two principal stresses ($\sigma_{\theta\theta}$,σ_{zz}), which are compressive, have no effect. From Eq. (4.16), σ_{rr} has a maximum at the edge of the contact area with a value of

$$\sigma_{rr_{max}} = \frac{1 - 2}{2} p_m \tag{4.19}$$

This equation immediately suggests that materials with higher Poisson's ratio are less susceptible to impact damage at 90° impingement angle than those with lower ν_s, while rubbery-type materials with $\nu_s = 0.5$ should have no tensile stress. So, from this simple expression one can expect higher erosion rate and lower critical load for fracture initiation when materials with lower ν_s are used. But since it is not possible to find two test materials that differ only in ν_s, exact verification of the importance of this material constant is not possible. This same problem exists with the other material properties. This inseparability and the complex interaction between the variables is what has made this problem very challenging.

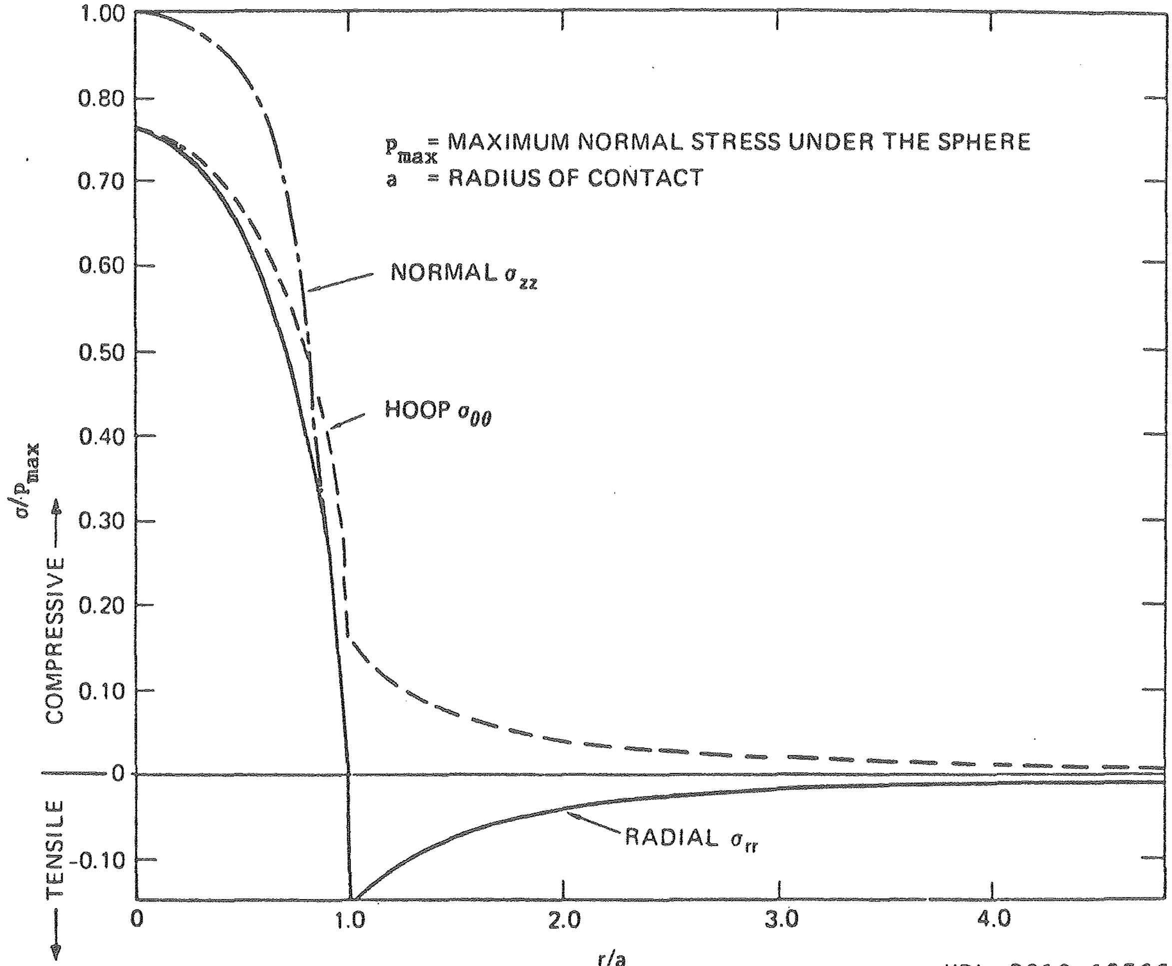

XBL 8010-12566

Fig. 4.2. Surface stress distribution for quasi static elastic contact.

According to Eqs. (4.7) and (4.9), all other stresses are also directly proportional to p_m. Therefore, this quantity can be thought of as the driving force for any damage that might occur by impact, while damage morphology and extent is determined by the hardness and fracture toughness of the surface. The magnitude of p_m, as given by Eq. (4.8b), depends on the modulus of elasticity E and ν of both surfaces. The normalized variation of p_m for a glass surface with respect to p_{gg}, the mean pressure when glass indents glass, as a function of indenter elasticity for similar size and equally loaded spheres is plotted in Fig. 4.3. This figure shows that the influence of the indenter elasticity on p_m, and consequently on all other stresses, reduces beyond the initial rapid rise. Also, significantly higher loads would be required to create the same stress level when indenters of lower modulus are used. For instance, from Eq. (4.8b), using a glass indenter on a glass surface requires three times as much load to achieve the same contact stresses as if a tungsten carbide indenter of the same size was used. However, p_m remains constant regardless of the indenter material, if the surface plastically deforms under loading. In this case, the contact load distribution can be represented by a uniform pressure on the resulting cup-shape impression. This situation was studied in Section 3.6. However, unless very small particles are used the surface will fracture prior to any other process.

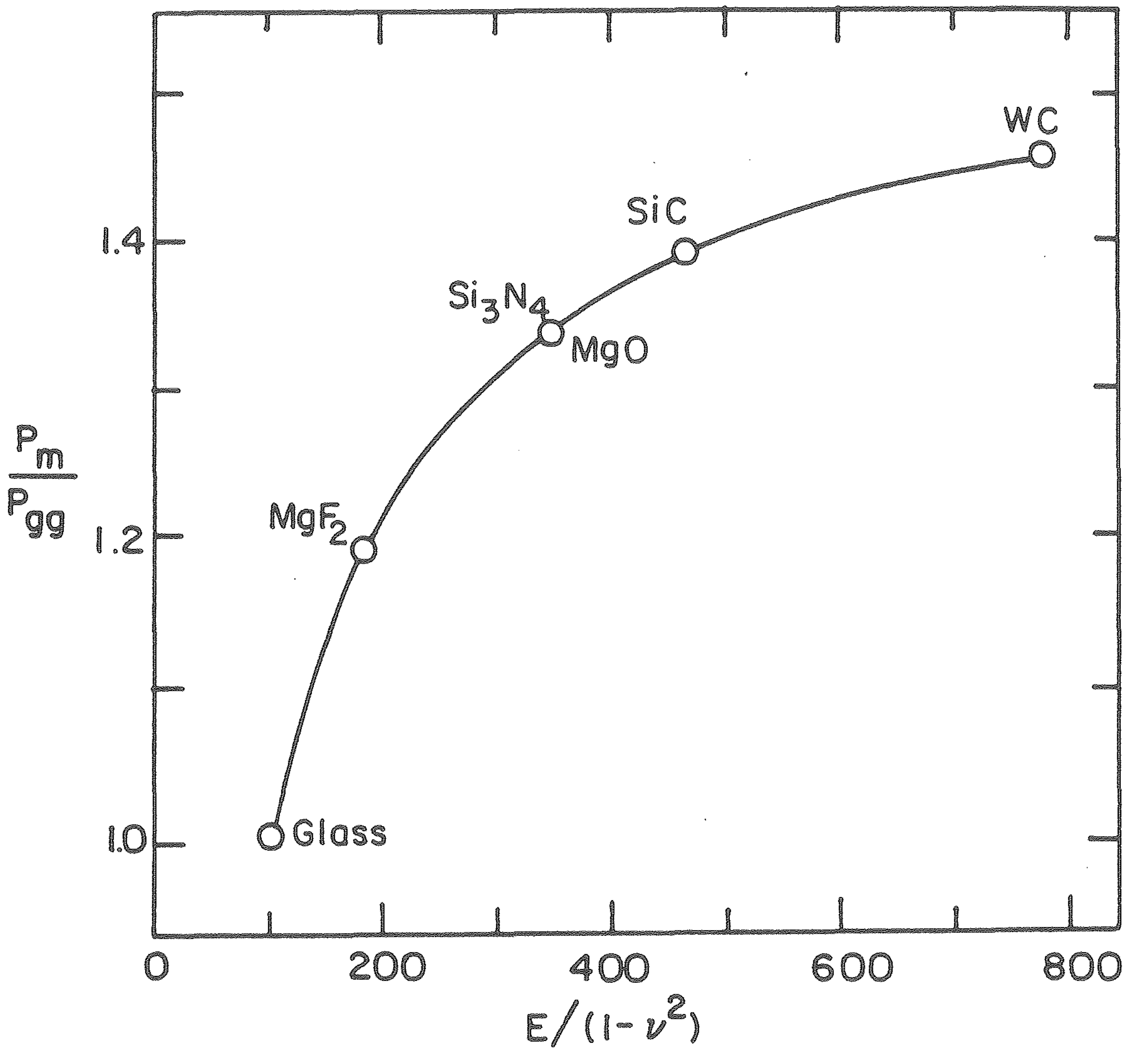

XBL8010-6212

Fig. 4.3. Effect of indenter elasticity ($E/1 - \nu^2$) on the mean contact pressure on glass. Same load is applied on all indenters and p_{gg} is the mean pressure when a glass indenter is used.

Increase of σ_{rr} with load leads to cone formation once a critical load has been reached. The maximum stress corresponding to this load occurs at the rim of the contact area, $r = a$ and is

$$\sigma_{rr_{max}} = \frac{1 - 2\nu}{2\pi} \left(\frac{P_{cr}}{\lambda^2 R^2}\right)^{1/3} \tag{4.20}$$

Since, by measuring P_{cr} the value of the stress can be easily calculated, the indentation test appears to give a convenient method for surface strength determination of brittle materials. But it has been observed consistently that σ_{rr} at the location of fracture may be as low as 25 percent of the maximum given by Eq. (4.20). So the prediction of the location of fracture should be the first step toward determination of the surface strength.

4.2. Comparison Between Experiment and Theory

As was mentioned earlier, from σ_{rr} in Fig. 4.1 it is expected that according to the maximum-stress theory fracture will start at the rim of the contact circle where the tensile stresses are the highest. This would be expected to happen when σ_{rr} reaches a critical value. From linear elastic fracture mechanics, the stress σ_f required to propagate a flaw of depth c is given by

$$\sigma_f \sim 1/c^{1/2} \tag{4.21}$$

where the constant of proportionality will depend upon the fracture properties of the material and the geometry of the cracked part.

In terms of the development of a cone crack in the Hertzian stress field, as discussed in Section 3.3, it is generally agreed that a cone crack forms from a favorable surface flaw and then propagates until it finally becomes arrested in the weakening stress field remote from the contact area. It is sometimes assumed that the flaw which initiates the cone crack is subjected to a stress state closely approximating uniaxial tension. By equating the fracture stress σ_f to the maximum tensile stress $\sigma_{rr_{max}}$ Eqs. (4.20) and (4.21) lead to

$$\frac{P_{cr}}{R^2} \sim c^{-3/2} \tag{4.22}$$

So, if fracture starts at the location of maximum stress, Eq. (4.22) gives the relation between the critical load for initiation, indenter radius, and flaw size. However, from direct observation of the formation of Hertzian cone cracks, it has been well-documented that fracture generally occurs outside the contact circle where stresses are lower, Fig. 3.4. Depending on the indenter size and the material and surface condition of the test specimen, the ring crack that leads to the eventual cone forms in the range of $r^*/a = 1.0–2.0$, where r^* is the radius of the surface ring crack. The lower values of this range are approached when larger indenters are used. According to the maximum-stress theory, fracture should always occur at $r^*/a = 1.0$.

If fracture would occur at a critical value of the maximum tensile stress, the critical load as indicated by Eq. (4.22) would be proportional to the square of the indenter radius R. But experiments, Fig. 3.7, show the mean value of P_{cr} is more nearly proportional to R when spheres with radii smaller than 1.0-3.5 cm are used. That is

$$P_{cr} \approx A\,R \tag{4.23}$$

where the proportionality constant A is named after Auerbach,[46] who was first to report this relation. Eliminating P from Eqs. (4.20) and (4.23) gives

$$\sigma_f = \frac{(1 - 2\nu)}{\pi}\left(\frac{A}{\lambda^2 R}\right)^{1/3} \tag{4.24}$$

This equation implies that the fracture strength of the test material is proportional to $R^{-1/3}$, instead of being a constant as one might have expected.

The attempts that have been made to explain Auerbach's observations and the equally curious feature that the crack forms away from the location of maximum stress are discussed in the next sections.

4.3. Energy Balance Approach

This is a deterministic approach which has been used by Roesler[57] and Frank and Lawn[51] in an attempt to explain the so-called Auerbach relation. Roesler states that crack propagation is a process involving a balance between the supply and demand of energy. Supply of energy comes from a portion (η) of the total stored elastic energy given by Eq. (4.4b), while demand arises from the need to supply surface energy as the crack propagates. It is assumed that the energy required for crack propagation can be written as

$$U_s = \theta\pi a^2\gamma \tag{4.25}$$

where θ like η is a variable that does not depend on P or R. The surface energy γ per unit area is measured in fracture tests. By equating Eqs. (4.4b) and (4.25) the following relation between P and R results:

$$P = \frac{1.57\ \pi\theta\lambda}{2} R \tag{4.26}$$

The proportionality constant in Eq. (4.26) is the Auerbach constant A. Although this derivation appears to be reasonable, it has no sound physical basis. In fact, it is incorrect because basically the problem here is one involving initiation and not propagation. The condition for initiation, like Griffith's criterion, is satisfied when the change in the total energy of the system with crack size is stationary. This condition is not satisfied in Roesler's derivation.

A second approach comes from Frank and Lawn[51] who, by using the techniques of Irwin's fracture mechanics, studied the details of crack propagation from a surface flaw at the rim of the contact area. They found that surface flaws of length $c < 0.0075a$ are subjected more or less to a uniform stress field, and consequently a favorable flaw will initially propagate unstably to a shallow depth. This process is assumed to go undetected. Then, with subsequent loading it propagates stably until it reaches a critical length of $c \approx 0.1a$, where once again unstable downward propagation is assumed to occur spontaneously to form an observable full cone which then grows stably with increasing load. The assumed sequence of events is schematically shown in Fig. 4.4. In the middle range, where cracks grow stably, the following relation was obtained for the energy release rate

$$G = \frac{4}{3\lambda E} F\ (c/a\ ,\ \nu\ ,\ r^*/a)\ \frac{P}{R} \tag{4.27}$$

F is a nondimensional function which just prior to spontaneous cone formation has a constant value because, at this time, according to their assumptions, r^*/a is equal to one and $c/a = c^*/a = 0.1$. Therefore, since at the time of fracture $G = G_{Ic}$, which is a constant for a given material, P/R has to be a constant. Then the Auerbach constant would be,

$$A = \frac{3}{2}\,\lambda E\gamma / F[0.1\ ,\ \nu\ ,\ 1.] \tag{4.28}$$

This equation for tungsten carbide indenting a glass surface with $\gamma = 4\ \mathrm{Jm}^{-2}$, $\lambda E = 0.73$ and $F = 5\times10^{-5}$ gives $A = 8.8 \times 10^4$ N/m (485 lb/in.). This value is about twice that usually obtained from experiment.[58] The over estimation in the above derivation is due to the incorrect choice of the fracture location which is not predictable from the analysis. As shown later by Lawn and Wilshaw[24] a more realistic choice of $r^*/a = 1.2$ leads to a larger value of F. Then, from Eq. 4.28, A would have a lower value. However, for this choice of r^*/a there is no longer the mid stability range which is the essence of the Frank and Lawn derivation.

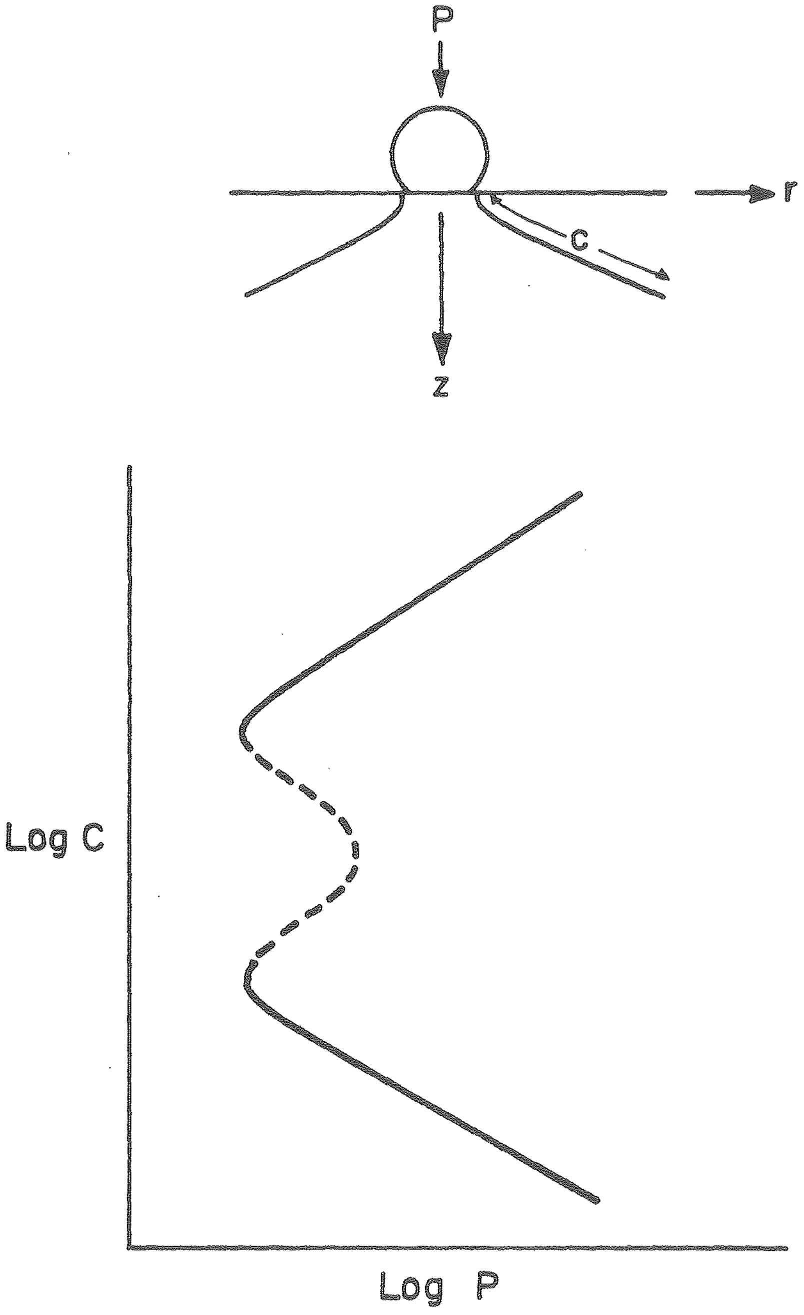

XBL 8011-13334

Fig. 4.4. The effect of applied load P on the length C of the Hertzian crack presented by Frank and Lawn.[51]

4.4. Effects of Friction

In the Hertzian analysis the pressure between the two bodies is assumed to be normal to both surfaces at every point of contact. However, the resulting displacements on the surface have a tangential as well as a normal component. In the absence of friction the tangential displacement of the surfaces are proportional to their respective values of the quantity $(1 - 2\nu)/G$, where G is the shear modulus. For dissimilar materials, the resulting relative displacement may, to some degree, be prevented by friction. Therefore, the true stresses are the summation of those produced by the normal pressure and those due to the frictional tangential tractions. The tangential tractions will act radially inward to the more compliant surface and outward on the more rigid surface. A study of this problem by Spense[52] has shown that the influence of the shear traction on the normal pressure distribution is very small.

Slip may be completely prevented in the center of contact where normal pressure is the greatest. But as the periphery of the contact area is approached the normal pressure approaches zero. Because of this, some slip near the edge of contact is inevitable.[52] A complete solution of this problem where both slipping and locking occurs would be very complicated. However, solutions have been obtained for two extreme situations where either "no slip"[52-54] or "complete slip"[54] are allowed. These solutions show that, for the case of no slip, stresses created by the frictional tangential component are directly proportional to p_m and the elastic mismatch parameter,

$$K = \frac{(1 - 2\nu_s)/G_s - (1 - 2\nu_p)/G_p}{(1 - \nu_s)/G_s + (1 - \nu_p)/G_p} \qquad (4.29)$$

subscripts s and p refer to surface and particle, respectively. The complete slip case is more complicated, but in general the coefficient of friction μ has about the same effect on the resulting stresses as K does on the no-slip situation.

Superimposing the friction-induced stresses on the Hertzian stress field will shift the $\sigma_{rr_{max}}$ from the edge of the contact area to greater radial distances as shown in Fig. 4.5a. Normalized values of these radial distances (r^*/a) for both cases are shown in Fig. 4.5b. In the actual case, where both locking and slip may happen simultaneously, the resulting curve should lie somewhere between the extreme cases shown in Fig. 4.5b. According to these results, the possibility of fracture outside the contact area increases as the elastic mismatch or friction is increased between the two bodies. However, it appears that friction and elastic mismatch are not the only factors in producing fracture outside the contact circle. It has been shown that with glass spheres indenting glass plates, the average value of r^*/a is about 1.2.

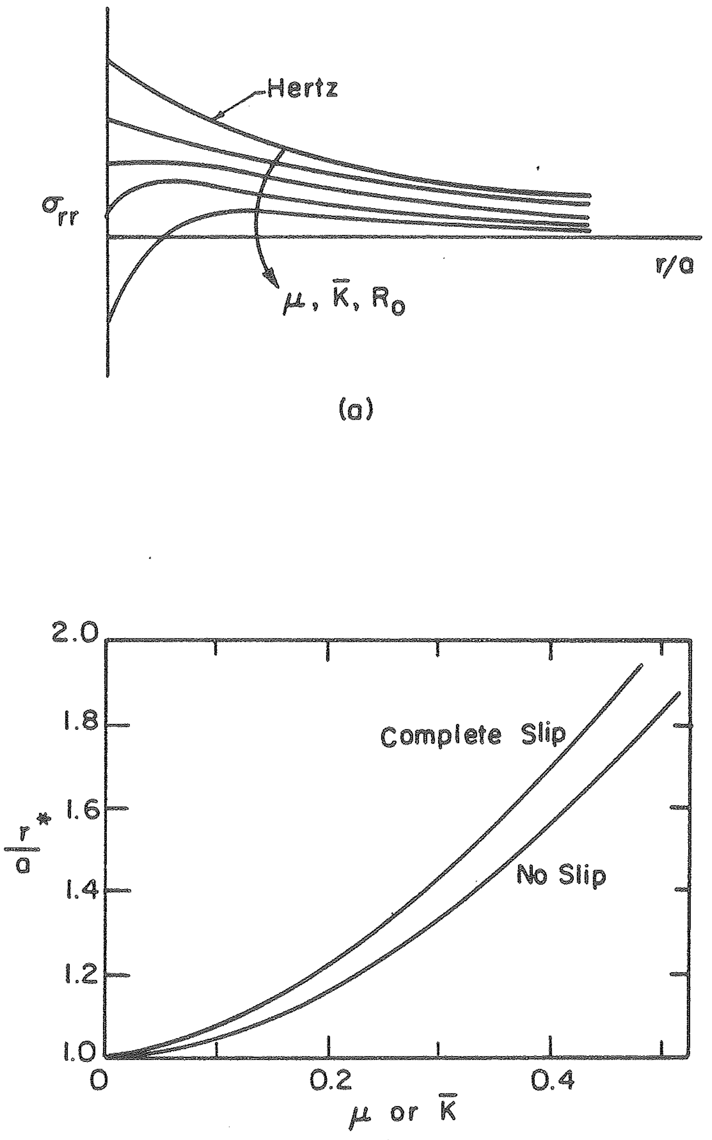

(a)

(b)

XBL 8010-6213

Fig. 4.5. (a) Schematic representation of the effect of the coefficient of friction μ, elastic mismatch parameter $\bar{K}$, and surface toughness R_0 on the surface radial stress σ_{rr}. (b) Location at which maximum σ_{rr} occurs. For complete slip the parameter involved is μ while for no slip, the coefficient of fraction does not enter the analysis and $\bar{K}$ is the important parameter.

4.5. Surface Roughness

Another explanation for the location of fracture comes from the direct use of Greenwood and Tripp's computation[62] of the effective pressure distribution between two elastic spheres as a function of surface roughness. Roughness is described by the density of asperities, their mean-tip radius, and a Gaussian distribution of their heights. The solution shows that the pressure distribution, particularly near the edge of contact, is a strong function of the surface roughness. Using this pressure distribution and assuming no friction, Johnson et al.[54] found that surface roughness reduces the magnitude of the maximum tensile stress on the surface and increases the radius at which it occurs. This is quite similar to results they had previously obtained for the effect of friction.

Variation of the radial stress σ_{rr} along the surface with the friction coefficient (μ), elastic mismatch (K), and increasing surface roughness is shown schematically in Fig. 4.5a. To avoid involvement with the intricate analysis of surface roughness, which is not necessary for the present discussion, it is merely denoted by R_o.

The methods that have been presented so far provide some possible and partial explanation for the experimental observations. Except for Roesler's procedure, which deals with the energy balance, all others use the magnitude of the principal tensile stress on the surface as the only condition for fracture. However, since fracture always initiates from randomly distributed flaws, it may be important to include this aspect in the analysis. This has been done in the probabilistic approaches, where the probability of fracture due to σ_{rr} is weighted by the area or the volume of the stressed region. As a result, some improvement and other explanations have been obtained.[47,61] This topic is discussed in the following section.

4.6. Probabilistic Approaches

There is at least one aspect involved in the indentation of brittle materials that cannot be explained by the deterministic approaches such as those already discussed. This is the scatter in the fracture load which, as shown in Figs. 4.6 and 4.7, has a definite dependency on the indenter radius. Also, as was pointed out in Section 4.4, the friction that arises due to elastic mismatch between the indenter and surface causes the location of fracture to move further away from the contact area. However, indentation of a surface with a similar type of material still shows the location of fracture is outside the contact rim. These observations indicate that consideration may have to be given by flaw statistics.

As a starting point, it is possible to relate the failure probability and the location at which it occurs to the number of flaws in a given volume. The larger this volume the higher the probability of finding a critical flaw. Based upon this, it could be argued that since large indenters are scanning over larger areas the probability of finding a critical flaw closer to the contact is higher than if smaller indenters were used. So that the location of fracture moves closer to the contact area by increasing the size of the indenters. It has been argued that with larger indenters the most critical flaw

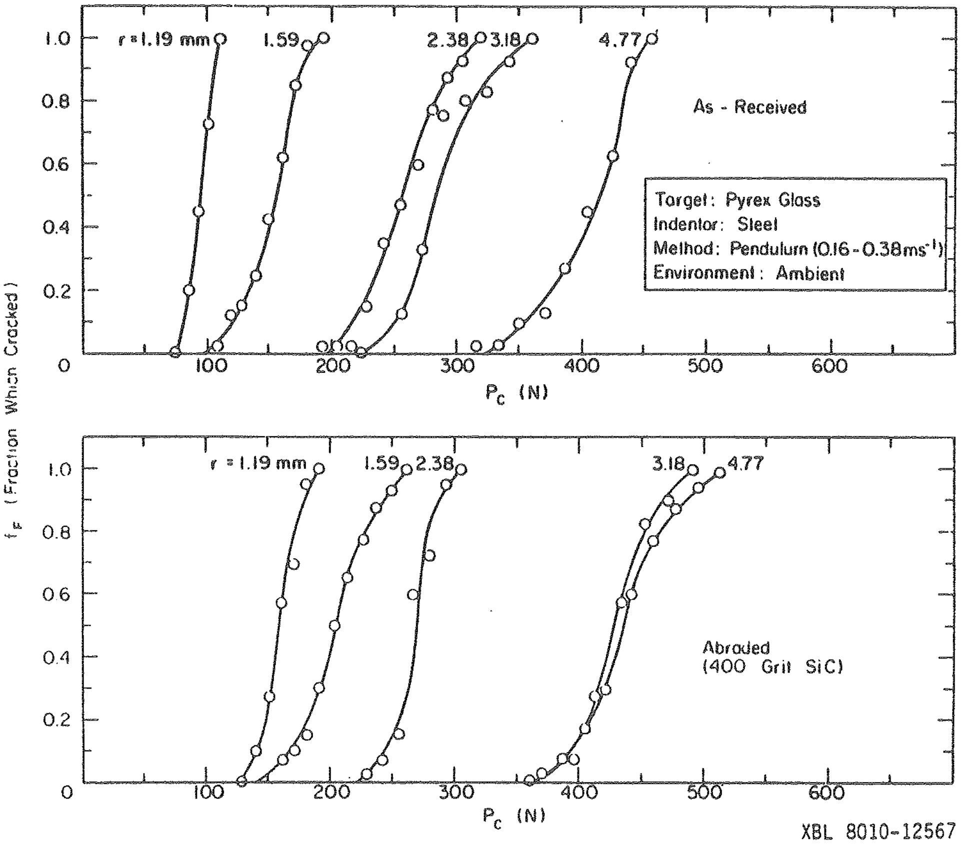

XBL 8010-12567

Fig. 4.6. The fraction of tests at a constant load which produced ring cracks versus the fracture load P_c (Dynamic test).[68]

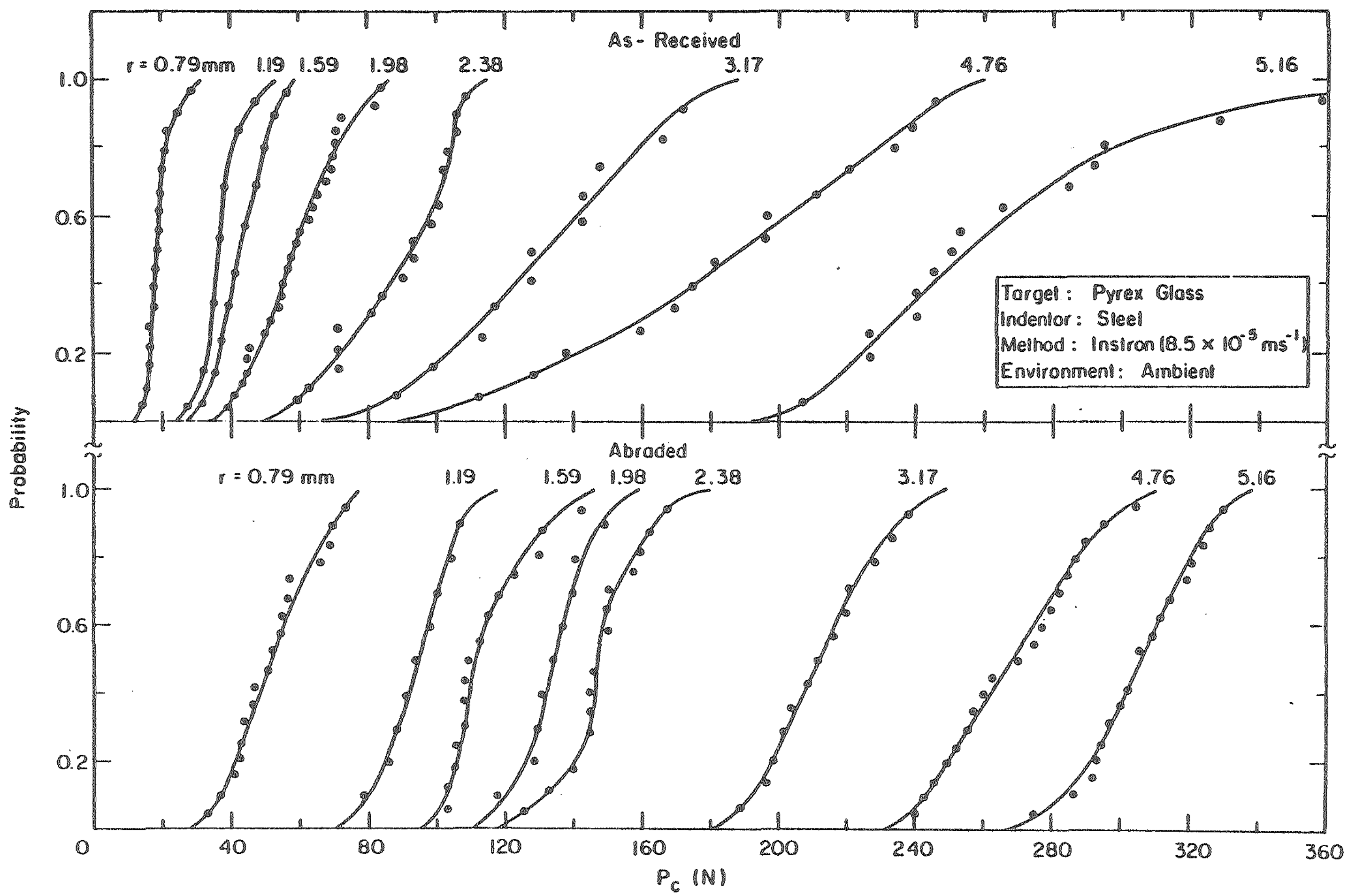

XBL 8010-12565

Fig. 4.7. The cumulative distribution function for failure as a function of load P_c in a quasi-static test.[68]

should be detected more consistently, and hence there should be less scatter in the results.[26] The fact that such behavior is not observed in indentation tests has been used to question the validity of statistical approaches. However, as will be shown later, this argument is erroneous. For tensile states of stress it is assumed in statistical theories that the flaws present in a part may be treated as links in a chain. When the weakest link breaks, the part fractures. On this basis, it may be shown that if the fracture probabilities F_i of individual links are small, the fracture probability of a chain of N links may be written as

$$F = 1 - \exp \; - \sum_{i=1}^{N} F_i$$

Extending this approach to identify a volume element with a link, F_i is replaced by $d\phi(\sigma)$ the probability of fracture for an elemental volume dv at stress level σ.

The probability $P_r(\sigma)$ of fracture due to unstable growth of nonintersecting cracks can thus be related to the state of stress σ by replacing the summation F_i by an integration to obtain

$$P_r(\sigma) = 1 - \exp - \int_V d\phi(\sigma) \qquad (4.30a)$$

The quantity $d\phi(\sigma)$ is given by

$$d\phi(\sigma) = dv \int_0^{\sigma} g(\sigma)\, d\sigma \qquad (4.30a)$$

where $g(\sigma)\,d\sigma$ is the number of flaws in unit volume that extend unstably when subjected to the stress range σ to $\sigma + d\sigma$. Therefore, $d\phi(\sigma)$ is the total number of flaws with strength in the range from 0 to σ in volume dv. Replacing σ by σ_m, the maximum tensile stress experienced by a part, Eq. (4.30b) becomes

$$P_r(\sigma m) = 1 - \exp\left[-\int_v\int_0^{\sigma_m} g(\sigma)\,d\sigma\ \ dv\right] \tag{4.31}$$

The probability of failure $P_r(\sigma_m)$ can be determined experimentally by testing a batch of similar specimens. Therefore, by knowing the geometry and stress distribution from Eq. (4.31) the only unknown $g(\sigma_m)$ can be found.[65] Based upon both surface and volume flaw distribution assumptions, Evans and Jones[66] have calculated values of the strength distribution function $g(\sigma_m)$ for some conventional fracture strength testing methods for ceramics. From their experimental results they found that in many ceramic materials failure is controlled by surface flaws at high strength levels, while volume flaws control fracture at lower strengthlevels. So that, strictly speaking, when predicting fracture probabilities the strength distribution should be obtained for the pertinent strength range.

The distribution $g(\sigma)$ obtained by this method can be used to obtain the fracture probability of components fabricated from the same material. However, the labor and computation involved in this method may cometimes be more than should be necessary for approximate solutions. Because of this, the following less accurate but more mathematically convenient Weibull function is often used,

$$\int_0^{\sigma} g(\sigma)\, d\sigma = \left(\frac{\sigma - \sigma_u}{\sigma_o}\right)^m \tag{4.32}$$

where σ_u is the lower limit of strength and σ_o and m are the scaling and shape parameters, respectively. These parameters by using Eq. (4.31) can be deduced easily from fracture strength data. By putting $\sigma = \sigma_{rr}$ from Eq. (4.16) into Eqs. (4.30) and (4.32), Oh and Finnie[61] derived equations for the mean (P_m) and standard deviation (P_{sd}) of fracture load

$$P_m = \frac{2\pi\lambda^2\sigma_u^3}{1 - 2\nu} F\left(\frac{\sigma_a}{\sigma_u}, m\right) \tag{4.33}$$

$$P_{sd} = P_m g(\sigma_a/\sigma_u , m) \tag{4.34}$$

where $\sigma_a = \sigma_{rr_{max}}$ is the stress at the contact rim given by Eq. (4.13). Also, based upon similar derivations they obtained a relation for the location of fracture as a function of strength parameters. The relations obtained by Oh and Finnie give the same trend as observed experimentally for the variation of P_m, location of fracture, and the scatter of fracture load P_{sd} with the indenter radius R, and in most cases good correlations were obtained.

The reason Oh and Finnie used the three parameter Weibull distribution rather than the computationally simpler two parameter distribution ($\sigma_u = 0$) was that the two parameter distribution leads to[67] the relation

$$P \sim R^{\frac{2(m-1)}{m+2}} \tag{4.35}$$

Thus it is unable to predict the transition from $P \sim R$ to $P \sim R^2$ as indenter size is increased. Typically $m \approx 8$ for a two parameter distribution and hence $P \sim R^{1.4}$ which at best expresses the overall trend of the data. For the three parameter distribution the value of m is lower and hence lower values of the exponent are predicted for small indenters. For large indenters the strength levels approach the constant value σ_u and the three-parameter distribution predicts $P \sim R^2$.

As we have seen, two completely different approaches—one deterministic and one probabilistic—have been used to explain the size effect. It will be pointed out later in more detail that both approaches have limitations. For this reason, a new approach will be taken to the problem of ring cracking since this draws upon both probabilistic and deterministic considerations; in essence, it reconciles the two approaches in the literature.

5. INDENTATION OF BRITTLE MATERIALS: A NEW APPROACH

As was discussed previously, almost all theories of Hertzian cracking use the magnitude of the surface stresses as a condition for crack initiation. Frank and Lawn,[51] by taking the stress gradient near the surface into consideration, found that the flaws on "as received" surfaces are subjected to varying stresses but the mean value of these stresses are tensile. On this basis, they assumed that cracks initially propagate unstably downward to very shallow depths. Then, because of diminishing stress the subsequent propagation becomes stable. Their calculation for cone crack initiation is based upon the sequence of processes that occurs after this initial unstable growth. Since this propagation to shallow depths has never been observed experimentally, it is important to examine the criterion for propagation of a flaw more critically in order to evaluate both the Frank and Lawn assumptions and the validity of calculations based upon surface stresses.

In the following calculations tangential surface stresses due to friction and roughness effects are neglected. While these factors strictly should be included they greatly complicate any analysis. Since the approach that will be taken here is quite different from these in the literature it appears best to emphasize the physical assumptions and main results without including the additional complicating factors of friction and roughness. At a later stage if the present, or some other approach to Hertzian cracking is accepted, the frictional and other correction factors could be included.

5.1. Criterion for Propagation of a Flaw

Stresses applied on the surfaces of a crack or a flaw situated in an inhomogeneously stressed body can be taken to be approximately uniform if their variation over the crack length c is very small. Therefore, for an infinitestimal flaw it is reasonable to assume a uniform stress. Hence, if such a flaw is extended it should, at least initially, grow unstably. But depending on the stress gradient, there exists a critical flaw size beyond which the uniform stress approximation is no longer valid.

The regions loaded by spherical indenters are geometrically similar when the ratio of R/a is the same, where R is the indenter radius and a, as given by Eq. (4.1), is the contact radius. The magnitude of the stresses at any location are proportional to the mean contact pressure, p_m while the spatial dimension of the stress field is proportional to a, which can be taken as a characteristic length. Thus, a critical value of the dimensionless ratio c/a can be determined beyond which the uniform stress assumption is no longer valid.

In order to express a fracture condition solely in terms of the surface stress and flaw size, it is required that the stress variation over that flaw be very small. Equivalently, the c/a ratio must be very small, otherwise the gradient has to be taken into account. The size of flaws on a typical as-received glass or ceramic varies from a few Angstroms to about 25 μm or larger.[80,69] For the present analysis the inherent flaws are idealized as shallow "thumbnails" protruding into the surface. That is, semi, ellipses with a depth (semi minor axis) much less than the major axis. For a steel ball (R = 1 mm) indenting glass, typical value of a at the time of fracture is about 50 μm. As it will be shown, for the largest crack that might be expected, with $c \simeq 25$ μm, a considerable variation of stress will exist over the crack. Hence, the c/a ratio of 0.5 for this case is too large for the assumption of uniform stress. The variation of $\sigma_1 = \sigma_{rr}$, near the surface, as a function of both the radial distance from the periphery of the contact area and the depth below the surface is plotted in Fig. 5.1. The stress gradient with depth is very large so that even the smallest flaws responsible for fracture will be exposed to varying stress.* In view of this observation, the discrepancy that arises from the theories that use the surface stress as a condition for failure and neglect the stress gradient is not surprising.

As the distance of the flaw from the contact area increases, the radial stresses decrease but remain tensile to a greater depth below the surface. To account for this variation we will follow the procedures of linear elastic fracture mechanics and load the faces with the varying stress distribution. At this stage, for the c/a ratios we are concerned with, only normal stresses are seen by the crack face.

---

*In fact, the faces of a flaw will see no normal stress in a tensile stress field. However, to calculate the stress intensity factor we apply the stresses that would exist on the plane of the crack in the uncracked solid to the faces of the crack.

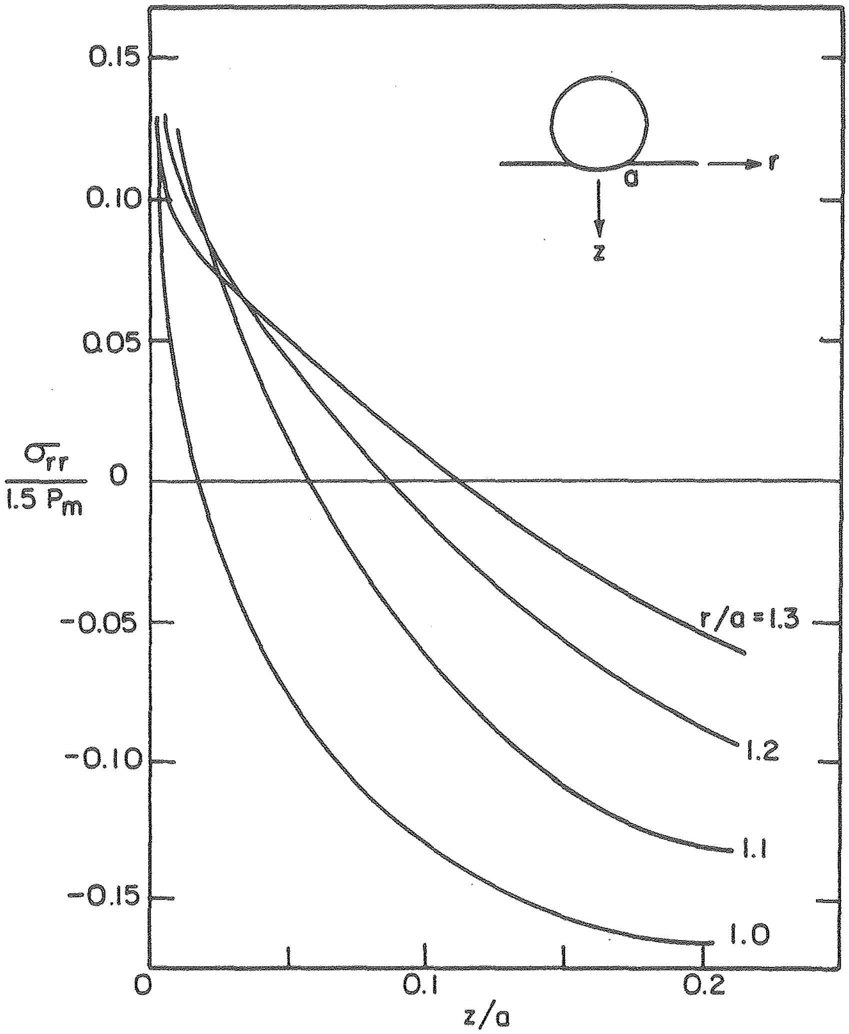

XBL 8010-6221

Fig. 5.1. Variation of σ_{rr} with depth z and radial distance r from the center of the contact area.

5.2. Effect of Stress Gradient

It is well-known that the stress intensity factor K_I for a crack in a variable stress field may be determined from the preexisting stress field. The stress intensity factor K_I for an internal crack of length 2c in an infinite body subjected to the distribution of prior normal stresses σ across the prospective crack plane can be written as

$$K_I = 2(c/\pi)^{1/2} \int_0^c \sigma(\xi)/(c^2 - \xi^2)^{1/2} \, d\xi \qquad (5.1a)$$

or equivalently[45]

$$K_I = 1/(\pi c)^{1/2} \int_{-c}^{c} \sigma(\xi)((c + \xi)/(c - \xi))^{1/2} \, d\xi \qquad (5.1b)$$

where ξ is the coordinate measured from the center of the crack and along the crack direction. The stress intensity factor K_I for an edge crack with length c in a semi-infinite solid is about 12 percent higher than that given by Eq. (5.1) due to the free surface.

In the Hertzian stress field σ is the magnitude of the principal stress σ_1, at the surface and at shallow depths below it, outside the contact area. At the time of fracture, for all practical purposes the σ_1 trajectory is parallel to the surface, and depending on c/a and r/a remains as such along the length of a surface flaw. So flaws or cracks, as also observed experimentally, propagate initially downward before turning into a cone. Substituting σ_{rr} from Eq. A3 for σ in Eq. (5.1) yields

$$K_I = K_I(c, P, R, r, M) \qquad (5.2)$$

where M is a constant related to the elastic constants for both surfaces. Due to the complexity of the integrand, obtaining a closed form solution for K_I is not possible. Because of this, each case needs to be dealt with separately by using the procedure that follows. For the present calculations, the case of a spherical steel particle indenting a glass surface with a uniform flaw distribution will be considered. Then, from the results that will be obtained, the effect of using materials other than glass will be pointed out.

Equation (5.2) shows that K_I as well as being a function of P and R also depends on the distance r of the surface flaw from the contact area and the flaw size c. For the time being it is assumed that the surface flaws have an arbitrary distribution and are of all sizes up to a limiting size c_1. The stress intensity factor was evaluated by numerical integration of Eq. (5.1) for the typical case of R = 2.5 mm for different size flaws located at various distances from the contact area on the surface. It is convenient to present the results in terms of the nondimensional geometrical parameter Y defined in the following equation

$$K_I = 1.12\, \sigma_a\, Y\, c^{1/2} \tag{5.3}$$

where σ_a, as given by Eq. (4.19), is the radial stress at the rim of contact area. Y for flaws corresponding to several c/a values is plotted in Fig. 5.2. An interesting feature of this plot is that for

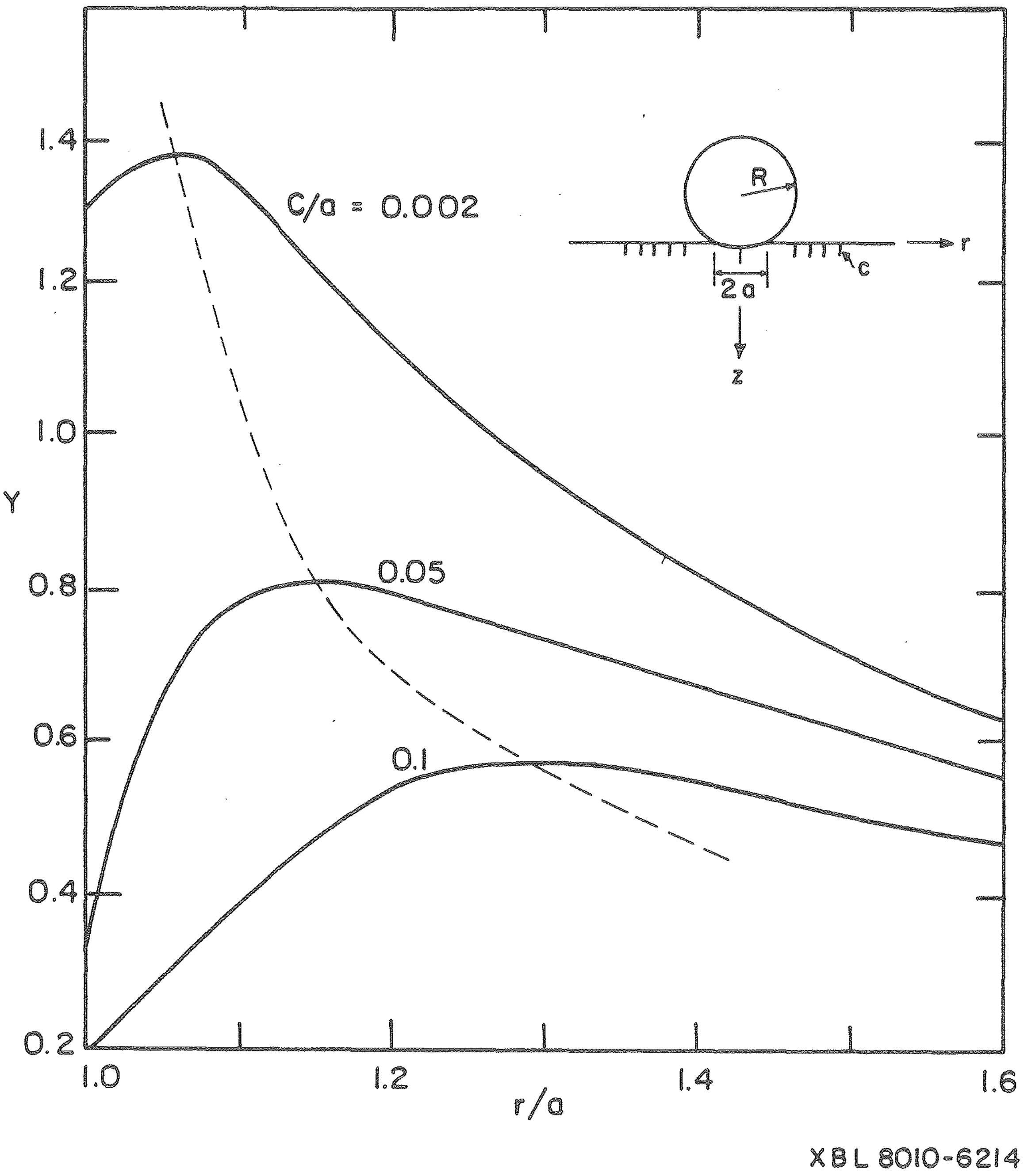

Fig. 5.2. The effect of the location of a surface flaw with several e/a ratios on the parameter y.

any normalized flaw size, Y increases with the distance from the contact area up to a critical distance r*/a which depends on c/a. Beyond r*/a, Y reduces with r/a and eventually goes to zero. It is also interesting to note that large flaws located near the contact area would have very small or even negative stress intensities and hence would not propagate.

The existing flaws should have a negligible effect on the stress distribution in the Hertzian contact field since stresses are mostly compressive. Flaws located in the compressive region are of no interest. But those located in the region of tensile stress are not fully exposed to the stresses calculated from the Hertzian solution. These flaws get partially "shielded" by other flaws in their vicinity against stresses they would experience if the other flaws were absent. An exact calculation of the stress intensity factor for randomly distributed cracks is very difficult if not impossible, since even their distribution is not known. However, solutions for simpler cases such as that shown in Fig. 5.3 can be used to obtain a rough estimate of how much K_I reduces due to the existence of other flaws. Examination of this figure reveals that it would not be unreasonable to drop the 1.12 factor from Eq. (5.3) for better accuracy.

5.3. Location of Fracture

The peaks of the curves in Fig. 5.2 which represent the most probable location for fracture, r*/a, are plotted for the corresponding c/a values in Figs. 5.4 and 5.5. Results for c/a > 0.2 become uncertain because the exact modification of the stress field around those

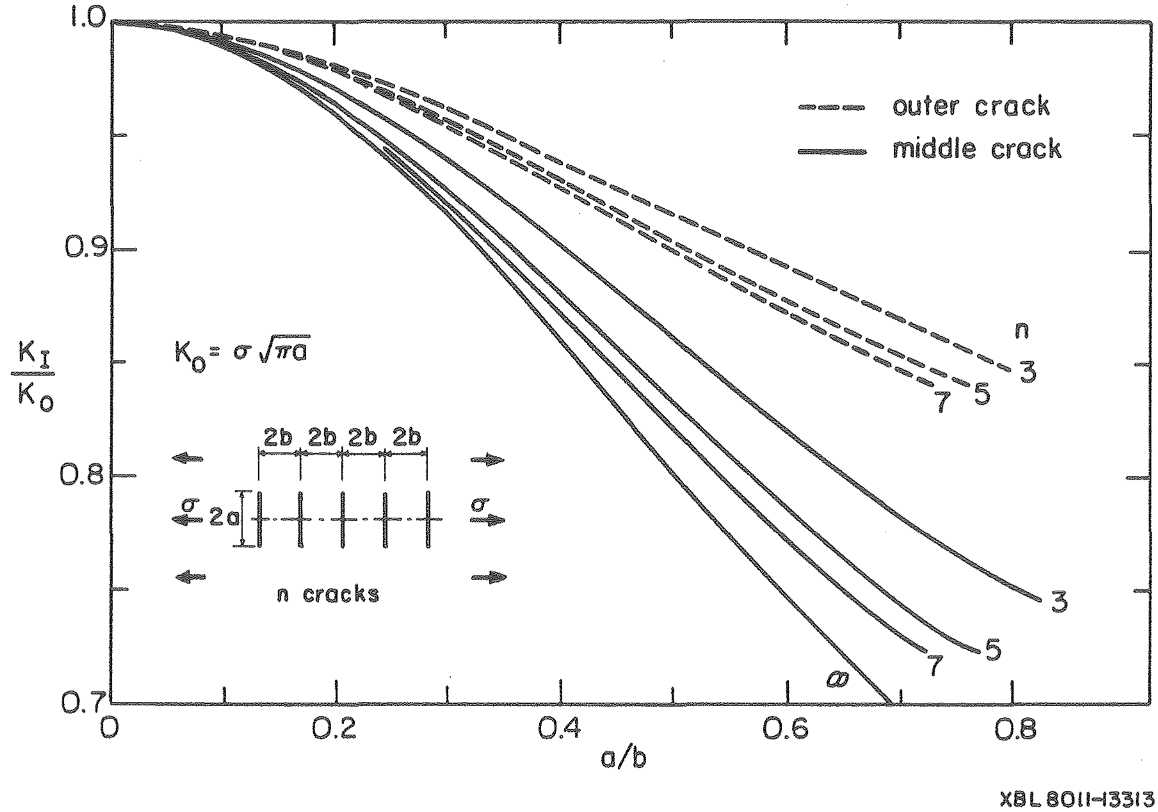

Fig. 5.3. K_I for the middle and outer crack of n parallel cracks in a sheet subjected to a uniform uniaxial tensile stress.[63]

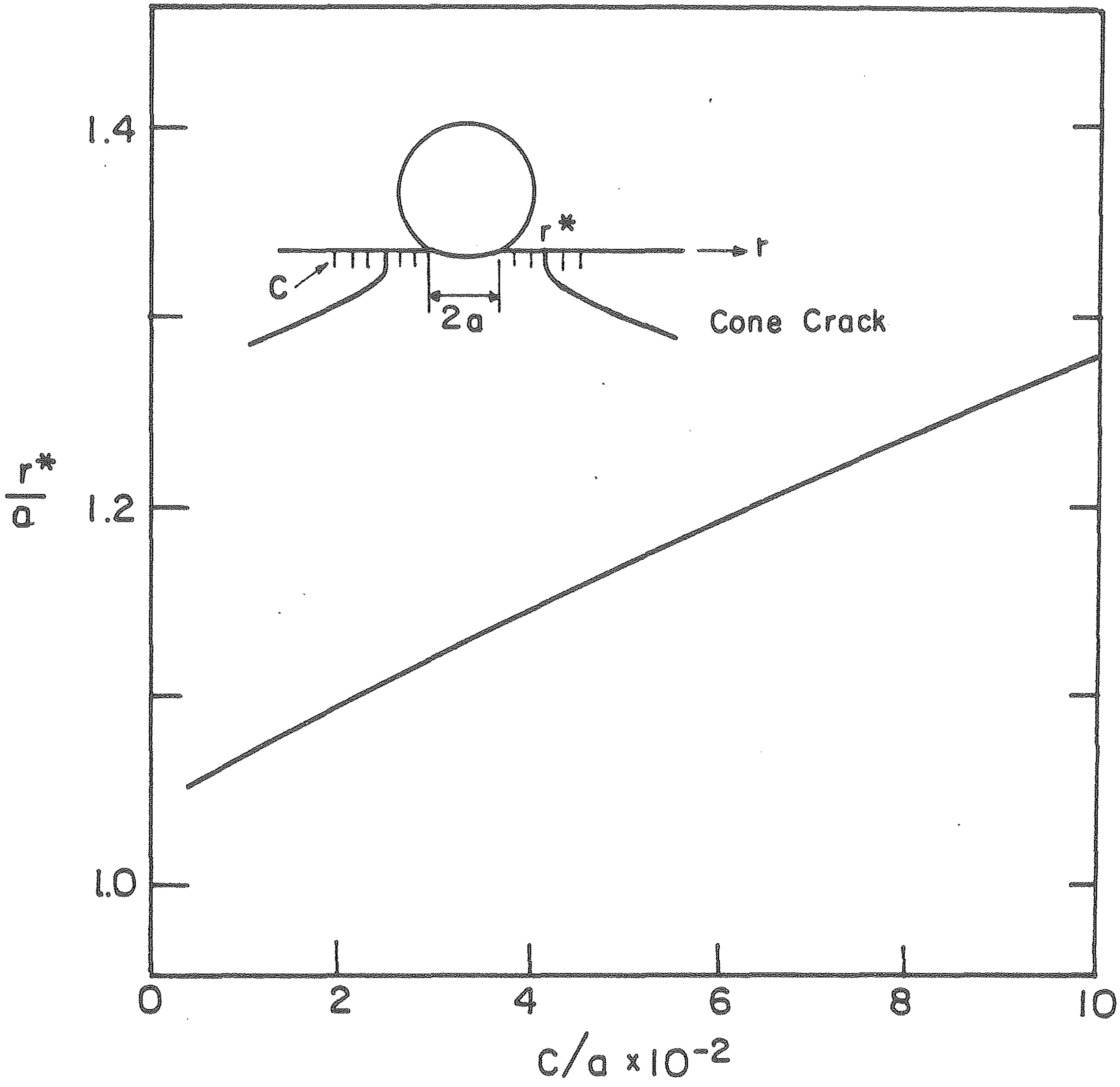

XBL8010-6222

Fig. 5.4. The location along the surface r*/a at which a flaw of size c/a has the highest value of the parameter Y.

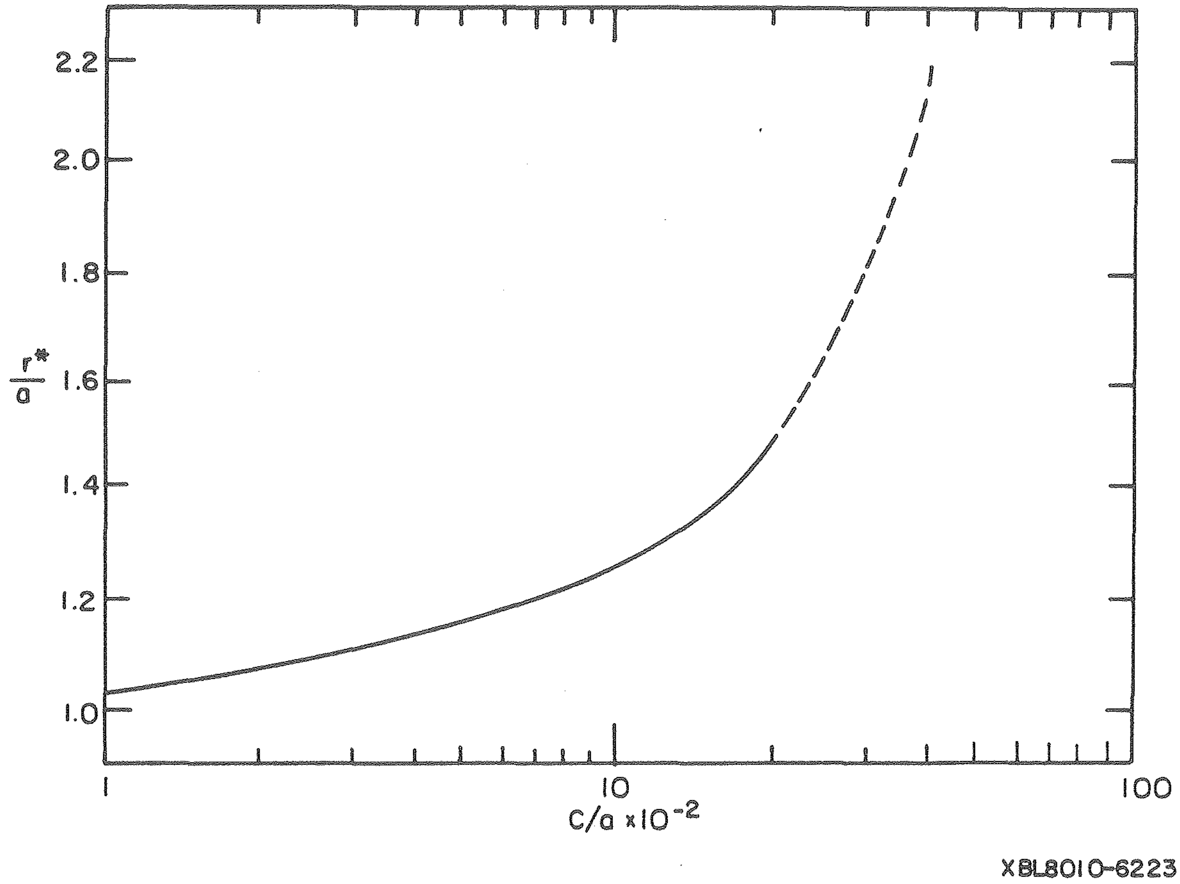

Fig. 5.5. A presentation similar to Fig. 5.4 but for a wider range of c/a values. The calculations for c/a > ~0.1 are unreliable and are shown by dashed lines.

long cracks is not known. Therefore, these results are shown by a dashed line in Fig. 5.5. However, in most indentation tests on undamaged surfaces c/a prior to unstable fracture is between 0.01 and 0.1,[51] and in this range the stress intensity values obtained from Eq. (5.1) by using the Hertzian stresses, can be used with confidence.

As Figs. 5.4 and 5.5 show, r*/a varies almost linearly with c/a in the range $0 < c/a < 0.1$. For larger values, its rate of change increases rapidly with c/a. This indicates that on surfaces containing mostly large flaws, or as smaller indenters are used fracture should start further away from the contact area, because of larger c/a ratios. Verification of this is provided by indentation experiment[60] on as-received and polished float glasses with various indenter sizes as shown in Fig. 5.6. As-received surfaces would be expected to have more and larger flaws than polished surfaces, and hence should exhibit larger r*/a values for the same indenter radius.

Figures 5.4 and 5.6 show the variation of r*/a with c/a. By invoking the Hertz solution, Eq. (4.1), and the Auerbach relation, Eq. (4.23), it may be shown that c/a is proportional to $cR^{-2/3}$, However, one should not attempt to use this result to relate r* to R. As will be shown later the size c of the flaw which leads to fracture increases with the indenter radius R. Thus making the variation of c/a or equally r*/a is insensitive to R. In section 5.7 it will be shown that some statistical treatments based upon the availability of certain size flaws are necessary for the explanation of the variation of r*/a with R.

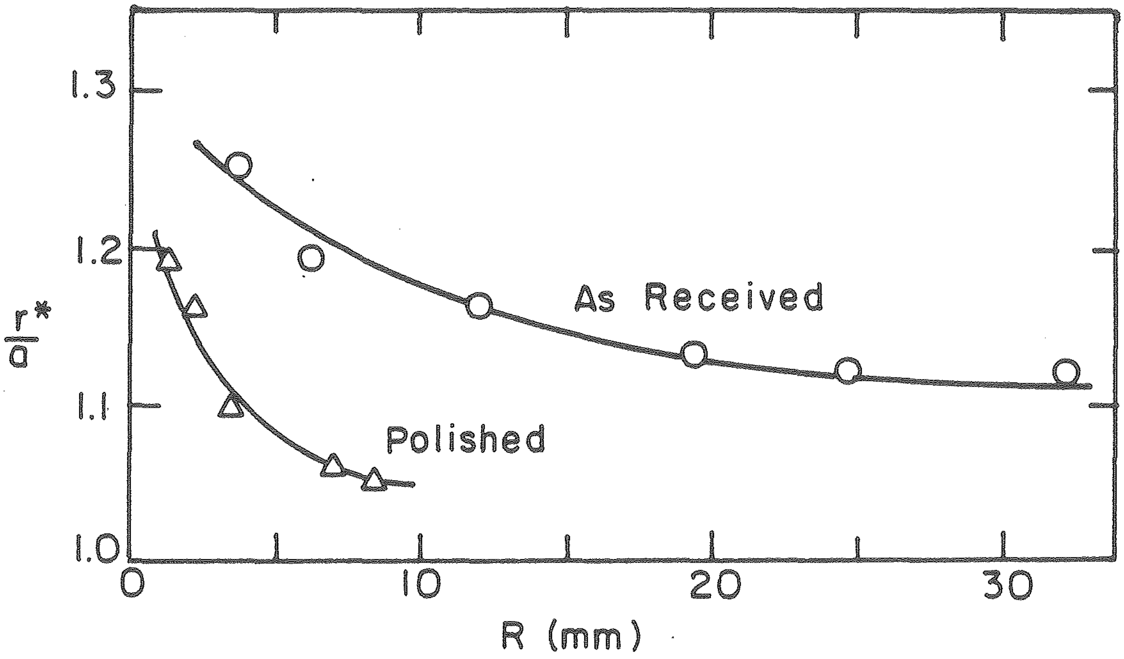

XBL8010-6215

Fig. 5.6. Effect of surface condition and indenter radius on the location of fracture r* on glass surface.[60]

5.4. Determination of Fracture Toughness by Indentation

Equation (5.2) shows that the stress intensity factor K_I depends on the flaw size c and its radial distance from the contact area r, or equally on c/a and r/a, as well as other factors. But as discussed in the previous section for the peaks of the curves in Fig. 5.2 there exists a definite relation between c/a and $r/a = r^*/a$. Therefore, the variable r in Eq. (5.2) by writing $r = r^*$ as a function of c can be eliminated, and K_{Imax} can be written as

$$K_{Imax} = K_{Imax}\ (P,c,R,M) \tag{5.6}$$

Again, this equation cannot be written in a closed form and numerical methods are required for its solution.

K_{Imax} values from Eq. (5.6) versus P for R = 2.5 mm and various flaw sizes are plotted in Fig. 5.7, and the general trend is shown in Fig. 5.8. Those figures show that at low loads the K_I of a small flaw is higher than that of a larger one. This situation, however, reverses at higher loads, so that at each load level a different size flaw will have the highest stress intensity factor. For instance, on a surface with K_{Ic} as shown in Fig. 5.8 fracture will start from a flaw with size of $c = c_2$ rather than any other flaw size.

If for each indenter size the minimum load for fracture, from Fig. 5.7, is plotted against the corresponding K_I value, a series of curves such as those shown in Fig. 5.9 will result. Each of these curves represents the envelope of a series of curves for a given value

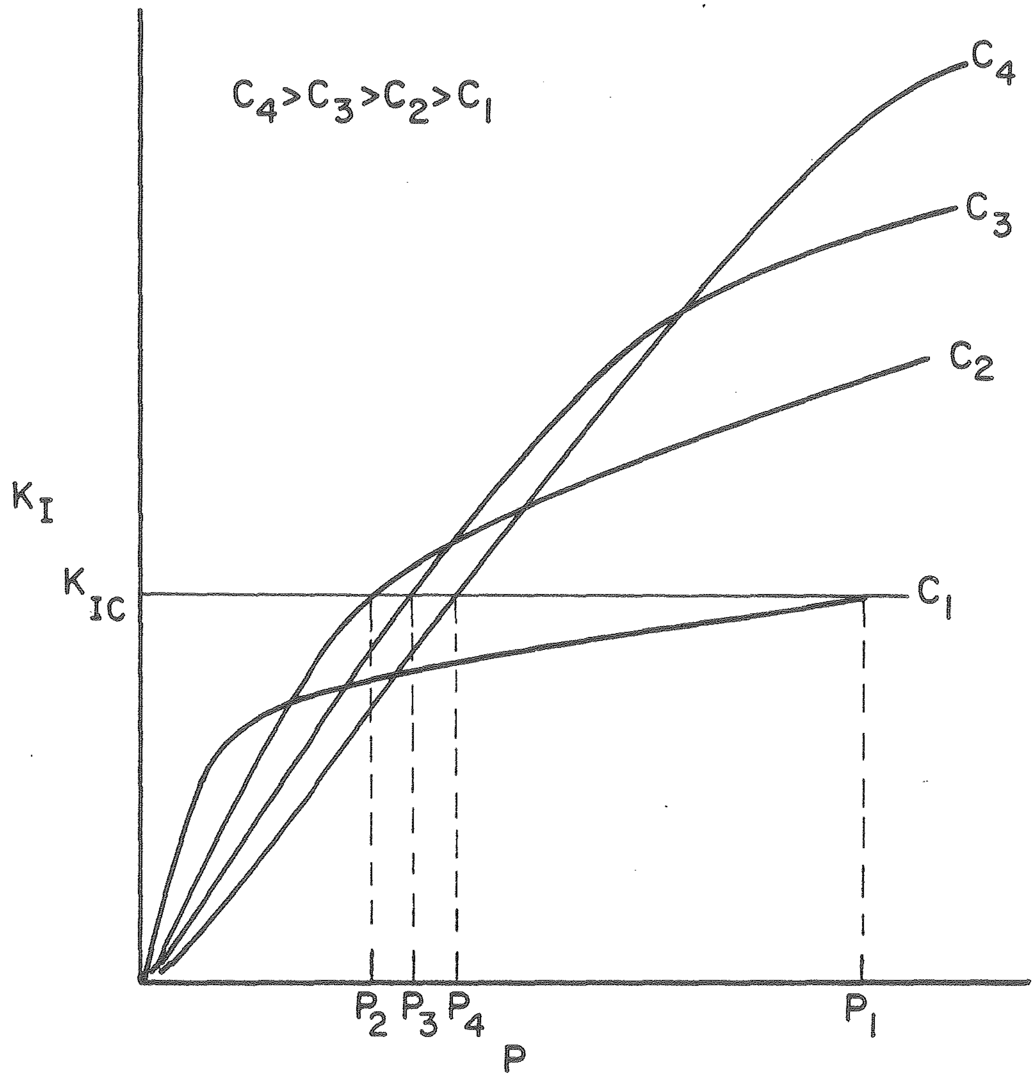

XBL8010-6225

Fig. 5.8. Schematic representation of the effect of the indenter load on the stress intensity factor for flaws of varying size.

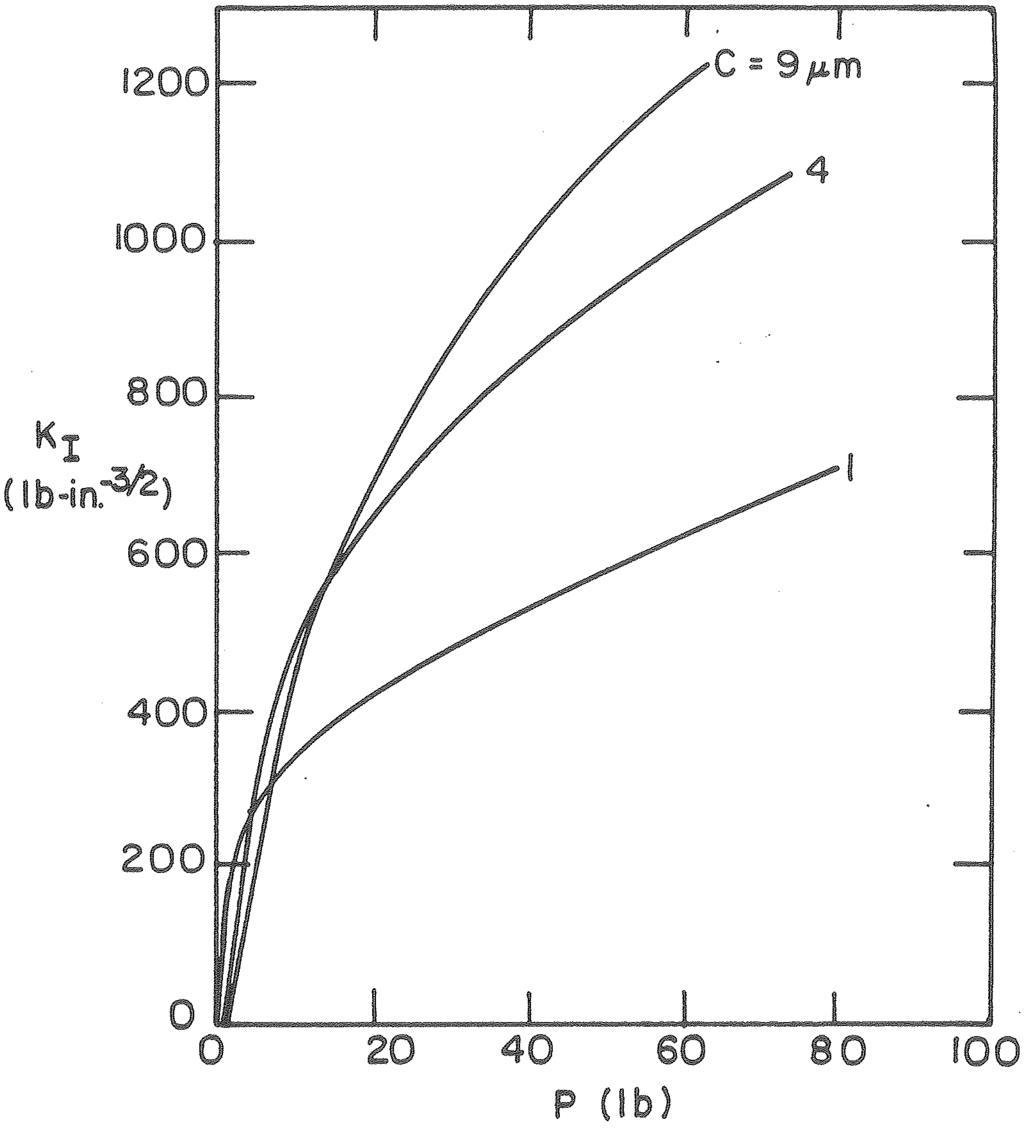

XBL 8010-6224

Fig. 5.7. Variation of the stress intensity factor with load for flaws of varying size. The load is applied by a R = 2.5 mm indenter.

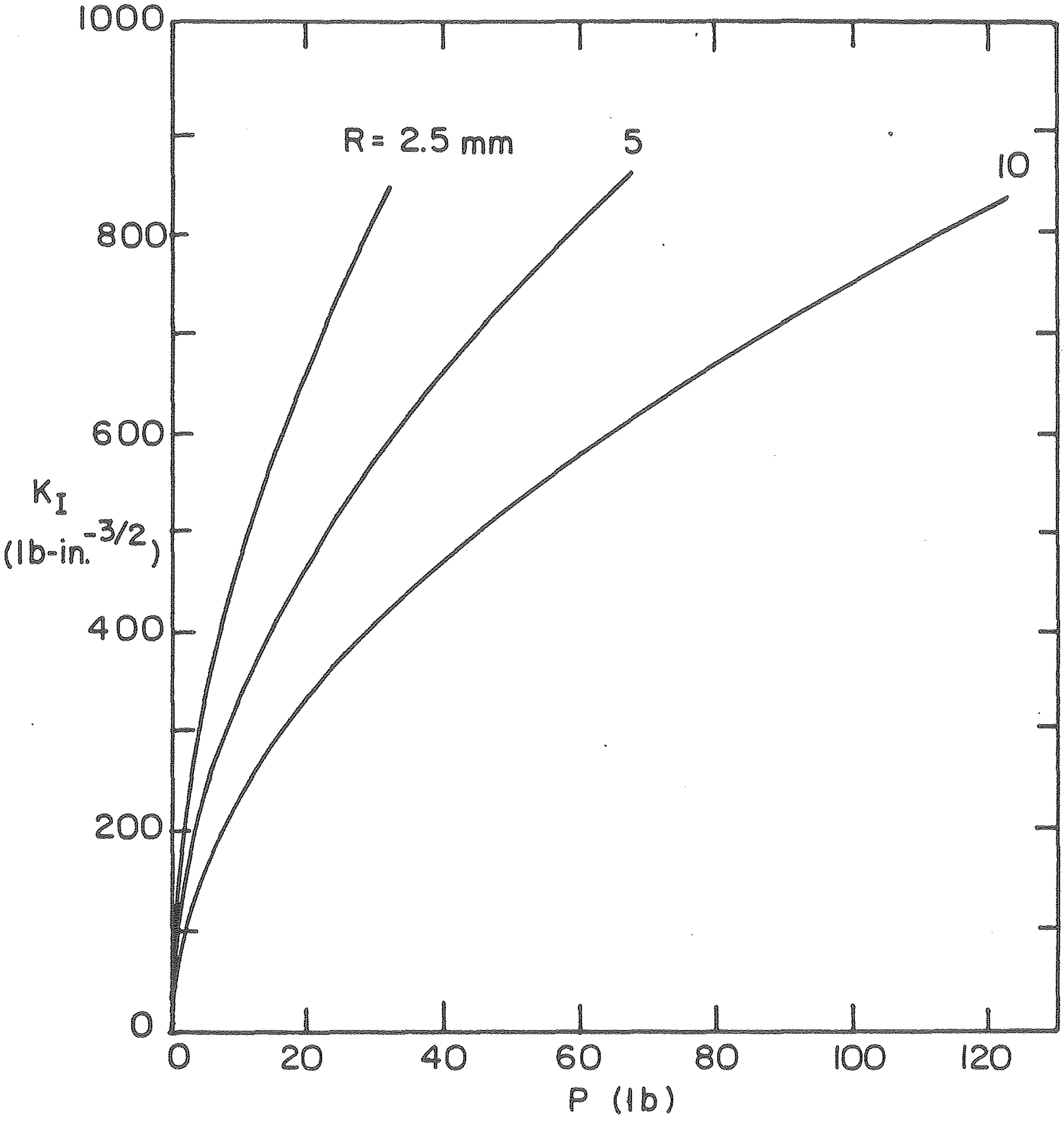

XBL8010-6226

Fig. 5.9. Variation of the maximum stress intensity factor on a glass surface with load P exerted by indenters of varying size.

of R such as those in Fig. 5.8. By plotting these curves for each surface-indenter combination and indenter size, the fracture toughness of a surface can be estimated by measuring the load at which fracture starts. However, because we are plotting the minimum load assuming that the right size flaw always exists at the right location $r = r^*$, and since on the real surface the existence of many flaws may reduce the stress intensity of the critical flaw, this procedure may overestimate the fracture toughness.

Strain rate is another variable that may influence the strength or fracture toughness. This is demonstrated by the indentation tests on pyrex glass shown in Figs. 4.6 and 4.7. Comparison between these figures shows about a 2.5 times increase in strength, with five orders of magnitude increase in strain rate. From Fig. 4.7, which represents a low rate of loading, P_c for $R = 2.4$ mm at 50 percent probability is about 20 lb (90 N) which from Fig. 5.9 corresponds to K_{Ic} of 690 $\text{lb/in.}^{-3/2}$ (0.76 $\text{mn/m}^{-3/2}$) or equivalently a surface energy of 4.3 J/m^2. This value is slightly greater than 4.0 J/m^2 obtained by Roesler[57] and Adler,[71] but is still within the range of reported values.

Because K_I changes rapidly with load, especially when smaller indenters are used, for better accuracy in obtaining K_{Ic} it is better to use as large an indenter as practicable. However, it will be shown later that the size of the indenter should be in the range where the predicted flaw sizes are present. Estimation of the flaw size from which cracks initiate and its effect on the fracture load which eventually leads to an explanation of the Auerbach relation is discussed in the following section.

5.5. Load-Crack Size Relation

Plots such as those shown in Fig. 5.7 can be used to obtain an estimate of the flaw size from which fracture will start. For instance, fracture most likely initiates from a 9 μm flaw when a glass surface with fracture toughness of 690 lb/in.$^{-3/2}$ (0.79 MP_a-$m^{1/2}$) is indented with a R = 2.4 mm spherical indenter. This happens because any smaller or larger flaw would yield lower K_I values. However, a 9 μm flaw might not exist or be favorably oriented at $r = r^*$ which is the distance from the contact area where the critical flaw must exist for a minimum fracture load. Because of this, higher loads would be required to propagate a favorable crack located at any other distance than r^* from the contact center. Also, lower loads might result in propagation of some other shaped flaws which yield higher K_I than the flaw shape assumed here. So, the number and availability of different size flaws play important roles in the scatter of the fracture load P_c. This topic is dealt with in Section 5.7. In this section, however, the variation of P_c with the surface flaw sizes, assuming that they do exist at $r = r^*$, is examined. Therefore, the results are expected to provide an estimate of the mean value of P_c that would be obtained experimentally.

To a first order of approximation when surface flaws are very small in comparison with the contact radius a, i.e., $c/a << 0.01$, the stress gradient along the crack trajectory may be considered to be small. This would prompt an unstable growth of a flaw located at the location of highest stress, $r^*/a \sim 1.0$, until a position of stability is once again attained remote from the contact surface. Integrating Eq. (5.1) for $c/a << 0.01$, $r^*/a = 1$ and using $\sigma = \sigma_{rr_{max}}$ from Eq. (4.19) gives[51]

$$K_I = \frac{PE^2}{R^2} F(\nu)\ ^{1/3} c^{1/2}$$

$$F(\nu) = 7.75 \frac{[3(1 - \nu_s^2)(1 - 2\nu_s)^2/32\pi]^{3/2}}{(1 - \nu_s^2) + (1 - \nu_p^2)\left(\frac{E_s}{E_p}\right)^2} \qquad (5.7)$$

where subscripts s and p refer to the surface and particle, respectively. Solving Eq. (5.7) for P gives

$$P = \frac{K_I^3 R^2}{F(\nu)\ E^2} c^{-3/2} \qquad (5.8)$$

Since this relation is only valid for $c/a << 0.01$ it can be used only when the surface contains extremely small flaws or when very large indenters are used. Neither case is normally encountered in indentation or erosion testing. Unfortunately, no closed-form solution such as the above can be obtained for larger c/a ratios.

The relation between flaw size c and load P from numerically integrating Eq. (5.1) for the particular case of a R = 2.5 mm steel ball indenting a glass surface with K_{Ic} = 690 lb-in.$^{-3/2}$ (0.79 MP_a - $m^{1/2}$) is shown in Fig. 5.10. By contrast to the Frank and Lawn assumption of r*/a = 1, here the value of r*/a for a given c/a is obtained from Figs. 5.2 and 5.4. Because of the uncertainty in accuracy, results for c/a > 0.1 are shown as dashed lines. Again, the minimum load requires that the surface have a large number of 9 μm flaws. Both load P and its rate of change dP/dc increase sharply if the fracture is to initiate from flaws less than 5-6 μm. On the other hand, if the smallest flaw size is larger than 10 μm, the increase of load for fracture would be very small up to c = 15-20 μm. Beyond this range, P again increases with c because of diminishing stresses at the location of fracture. But since the surface always contains a variety of flaw sizes, fracture will start from the one requiring a minimum load. As indicated in Fig. 5.10, the minimum load corresponds to a c/a ratio of 0.06. This value is insensitive to the elastic constants and corresponds to a r*/a ratio of 1.2; but c/a and consequently r*/a could vary from 0.04 to 0.1 and 1.1-1.3, respectively, with only 10 percent increase in the load. This increase might be necessary because of the nonexistence of the right flaw at the right location. This may explain why the radius of fracture is usually 10-30 percent larger than the contact radius.

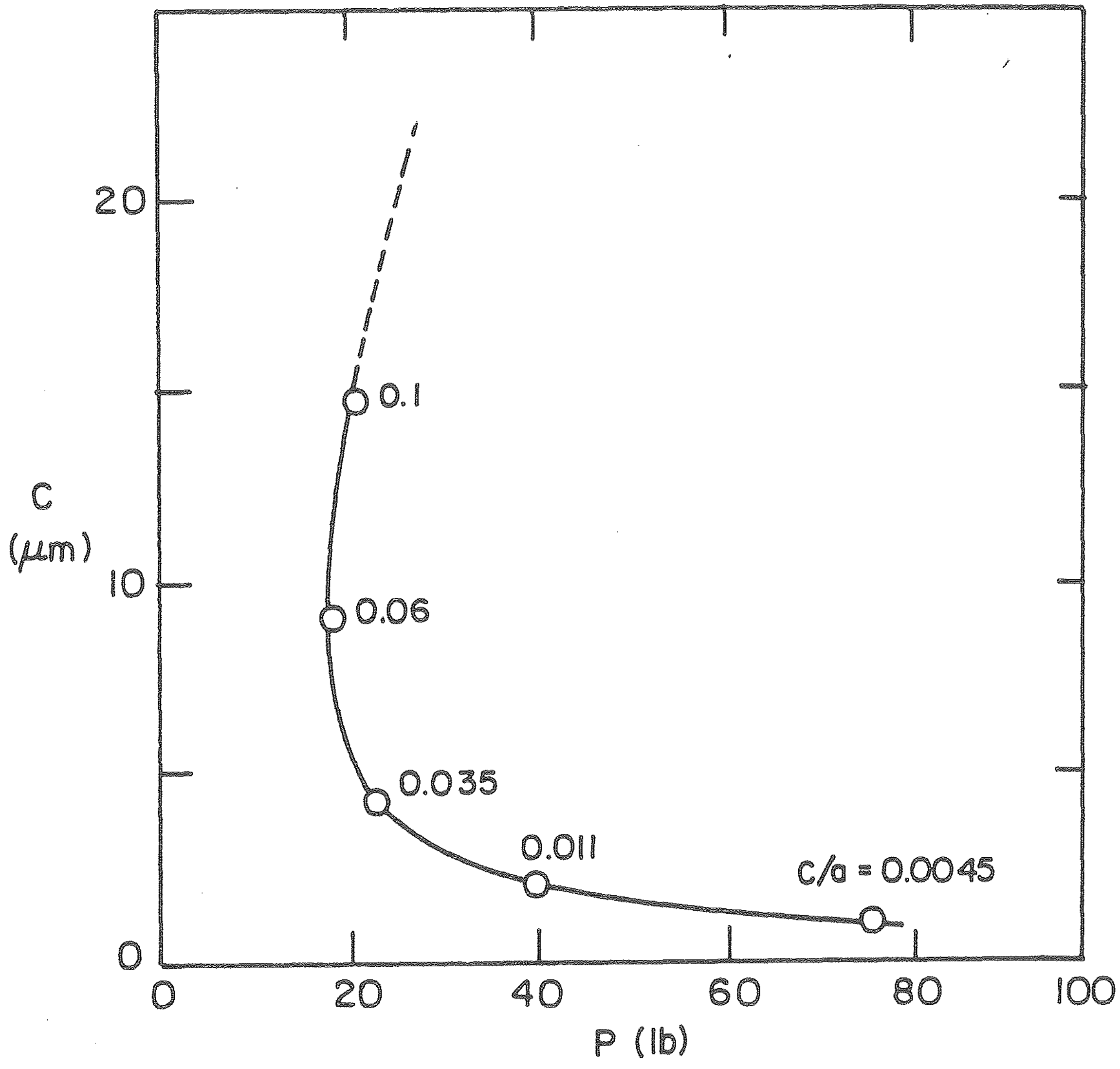

XBL 8010-6216

Fig. 5.10. Load P required to initiate fracture from different size flaws on a glass surface with K_{Ic} = 690 lb-in.$^{-3/2}$ and R = 2.5 mm.

For $c/a = 0.06$ and by invoking the Hertz solution, Eq. (4.1), and the Auerbach relation, Eq. (4.23), the preferred crack size for a given indenter size is

$$c_p = 0.06\ (A\lambda)^{1/3} R^{2/3} \tag{5.9}$$

The value of c_p from the above equation, for a given R, gives the size of the flaw that has the highest stress intensity. If the largest indenter for which the Auerbach relation holds is R_L, Eq. (5.9) can be used to obtain the size of the largest flaw c_L on the surface. For instance, if R_L is 1 in. (25 mm) and A = 200 lb in. (36360 Nm), Eq. (5.9) gives $c_L = 40$ μm.

In Section 5.8 it will be shown that A is proportional to the surface energy γ of the indented material. So, according to Eq. (5.9) the size of the flaw from which fracture initiates is larger on a surface with higher A, or equivalently with higher fracture toughness, or when larger and less rigid indenters are used. However, no conclusions can be drawn on the effect of these variables on the size of the largest flaw on the surface. As was demonstrated above, c_L for a given A and λ, can be predicted from Eq. (5.9) only by knowning R_L.

Equation (5.9) by making use of the Auerbach relation can be written in terms of the fracture load P as

$$c_p = 0.06\ (\lambda/A)^{1/3} P^{2/3} \tag{5.10}$$

So that by knowing A and measuring P the size of the starting flaw can be estimated.

Equations (5.9) and (5.10) were derived by generalizing the information from the particular c versus P curve shown in Fig. 5.10. However, they can also be obtained by plotting many such curves for various values of R and K_{Ic}. By doing so a relation between c and R for two values of K_{Ic} as shown in Fig. 5.11 was obtained. Very close agreement between the predictions of Eq. (5.9) and Fig. 5.11 further verifies its validity.

Another point that is evident from Fig. 5.10 is the absence of the intermediate range $0.01 < c/a < 0.1$ of stability for crack propagation as was assumed to exist by Frank and Lawn[51] in order to explain the Auerbach relation, Fig. 4.4. Crack propagation for $c/a > 0.06$ is stable, but a slight increase in load leads to large crack extension. It will be shown in the next section that no range of stability is necessary to explain the Auerbach relation. Rather it is just a consequence of the effect of the Hertzian stress field produced by different indenter sizes on various surface flaws.

5.6. Auerbach Phenomenon and Its Range of Applicability

In the previous section a relation between R and c was obtained, Fig. 5.11. This relation can be used to eliminate c from Eq. (5.6). Then for a given K_{Ic} a relation between the two variables, P and R, can be obtained. For two values of K_{Ic} the relations between P and R are plotted in Fig. 5.12, assuming that the necessary size flaws do exist on the surface. Linear relation between P and R, as indicated

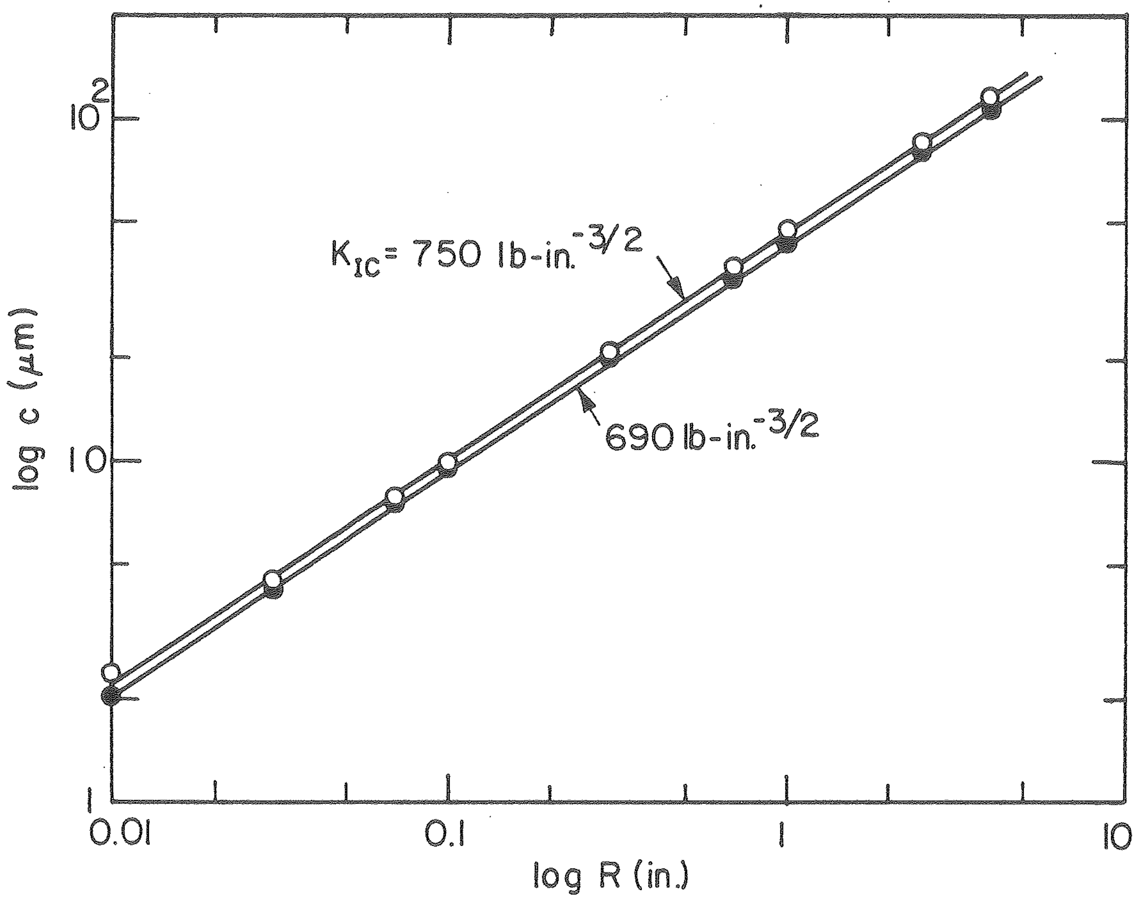

XBL8012-13407

Fig. 5.11. Crack size c from which fracture initiates versus indenter radius R.

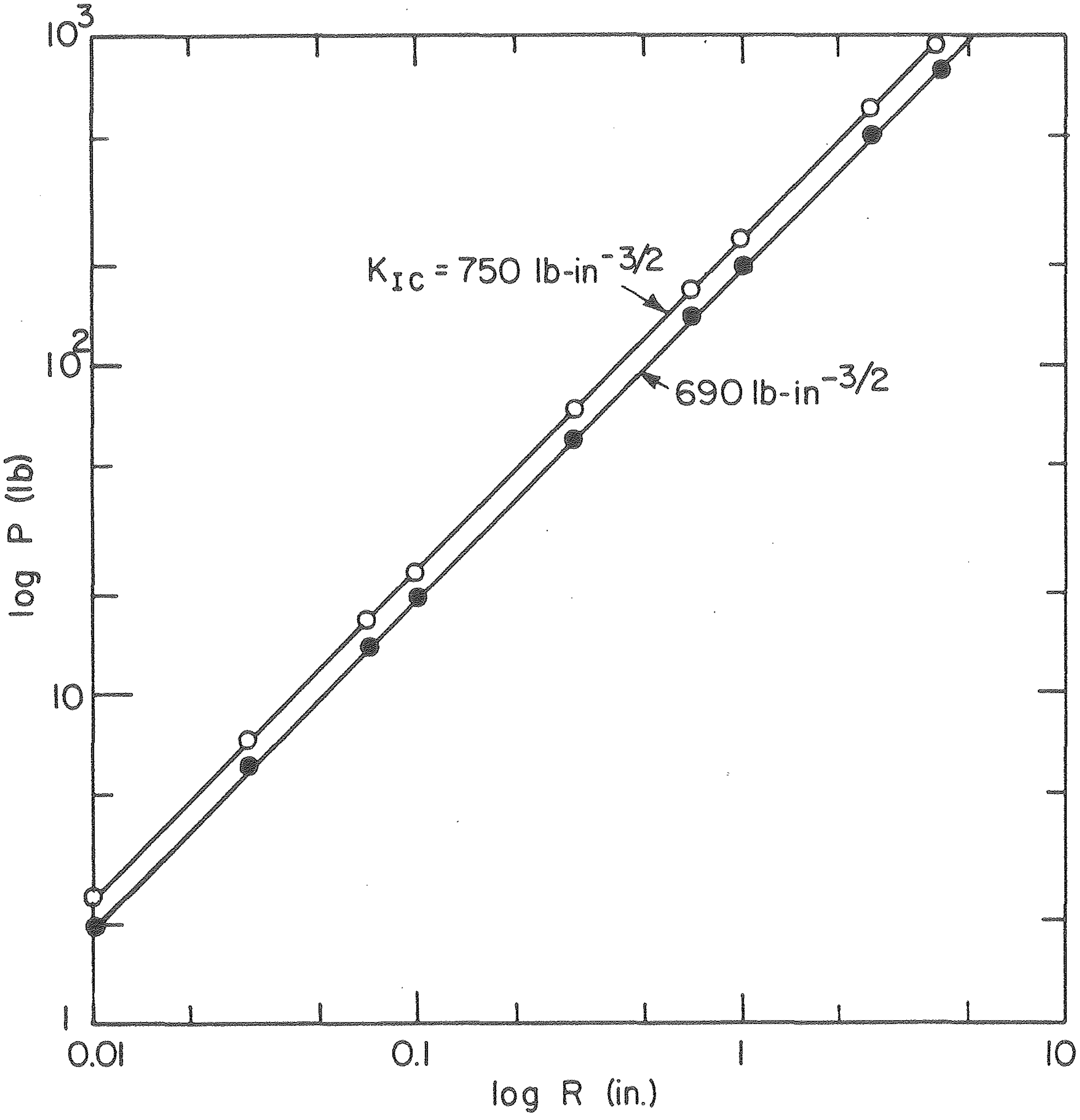

XBL8012-13406

Fig. 5.12. Minimum fracture load P for a indenter of radius R.

by Fig. 5.12, shows the trend of experimental results found by Auerbach and others. However, in Section 5.7 it will show that as R is increased the number of flaws with the required size decreases. Thus higher loads would be necessary for fracture. This leads to gradual deviation from linearity between P and R as R is increased.

Linear proportionality of P and R can also be shown by an indirect method. In order to do this, the stress intensity of the most severe flaw was calculated for various values of R. It is assumed that the surface contains flaw sizes in the range of 1-10 μm and the load for each indenter was assumed to follow the Auerbach relation and was taken to be 200 lb-in. times greater than its radius in inches. The results are shown in Fig. 5.13. According to these results the Auerbach constant of 200 lb-in. (36,360 Nm) corresponds to a surface fracture toughness of about 690 lb-in.$^{-3/2}$.

For indenters larger or smaller than 0.5-5 mm the stress intensity factor K_I reduces and consequently higher loads than $P \sim AR$ would become necessary. For any R larger than R_L, the largest R for which the Auerbach relation holds, there does not exist a large enough flaw for P to remain proportional to R. This causes the exponent of R, in the Auerbach relation, to increase slowly from close to 1 to values approaching 2, as R is increased beyond R_L. On the other hand, 1 μm which is the size of the smallest flaw, on this surface is too large for a very small indenter to cause fracture. In order that these indenters propagate a flaw, the load P must be increased considerably to bring the c/a ratio as close as possible to 0.06, the most likely

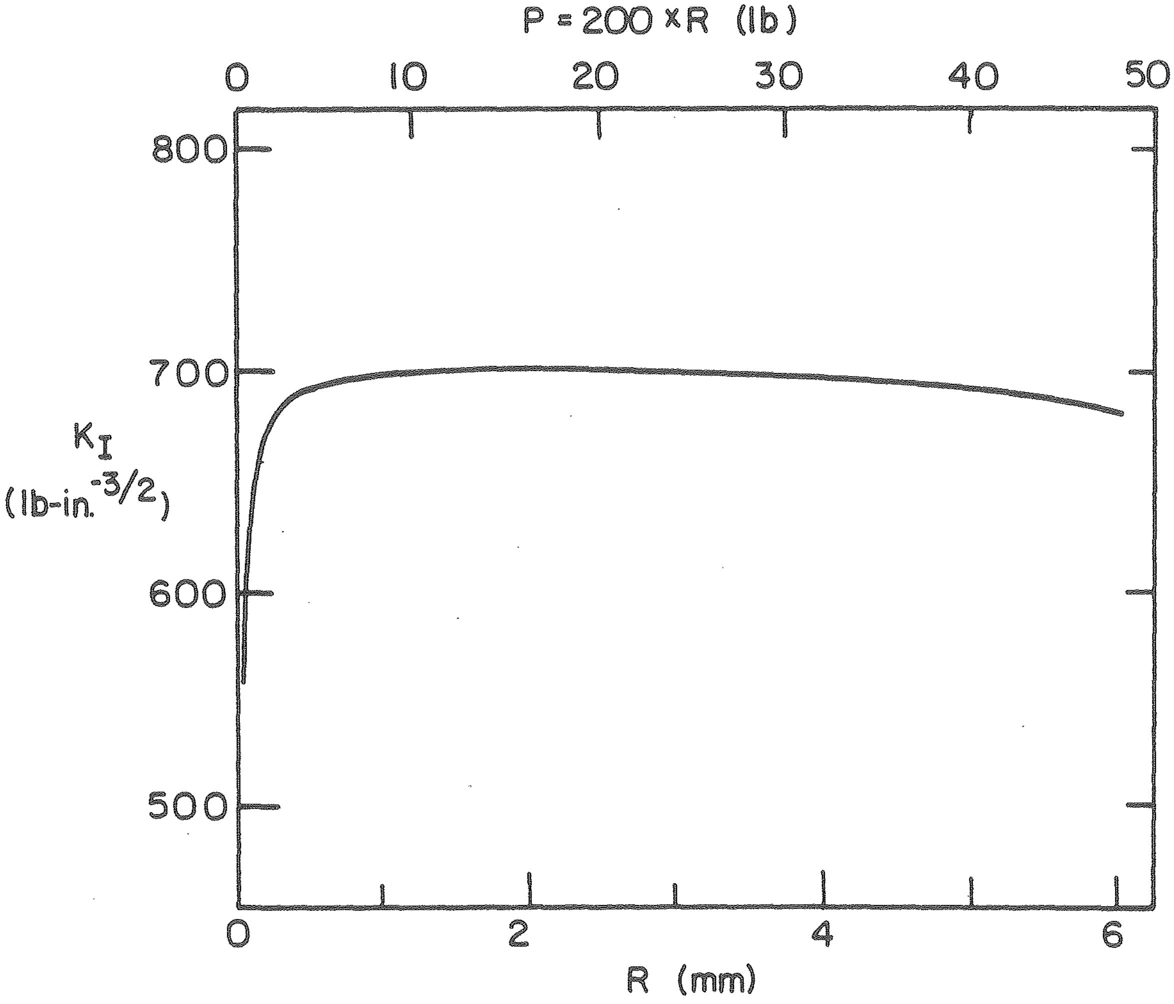

XBL 8010-6227

Fig. 5.13. Stress intensity factor for the most severe flaw on a glass surface containing flaw sizes in the range of 1-10 μm indented with various size indenters.

value at fracture. In doing so p_m might reach the hardness of the surface before K_I reaches K_{Ic} and then ductile behavior would be observed. Clearly, from these discussions it is apparent that the range of applicability of the Auerbach relation should depend on the range of available flaw sizes.

The large difference in the variation of K_I with P or R at the upper portion (large R) and lower portion (small R) of the Auerbach range, as shown in Fig. 5.13, may be better explained by the difference in the sensitivity of large and small indenters to the size of the available flaws. Figure 5.14 shows the variation of K_I with the size of the surface flaws for different indenter sizes. As can be seen, the peak of each curve becomes sharper as R is reduced. Thus, the peak regions correspond to a smaller range in c. For larger indenters a wider range of crack sizes give about the same K_I and, therefore, if the flaw size c_p that corresponds to the highest K_I does not exist, propagation from any other flaw close in size to c_p would require a minimal increase in load P. Quite the opposite is true for the smaller indenters.

Since, for any R larger than R_L all fractures start from the largest flaws on the surface, c_L, the c/a ratio decreases with increasing R. According to Fig. 5.4, this reduction of c/a causes the location of fracture to move closer to the contact area. This is also what the experiment shows, Fig. 5.6. No accurate calculations for $0.1 < c/a < 2$ are possible. But it is clear that small particles may be incapable of propagating large flaws. Also, in this case because of higher c/a ratios fracture will start further away from the contact area (large r^*/a), where the surface stresses are lower.

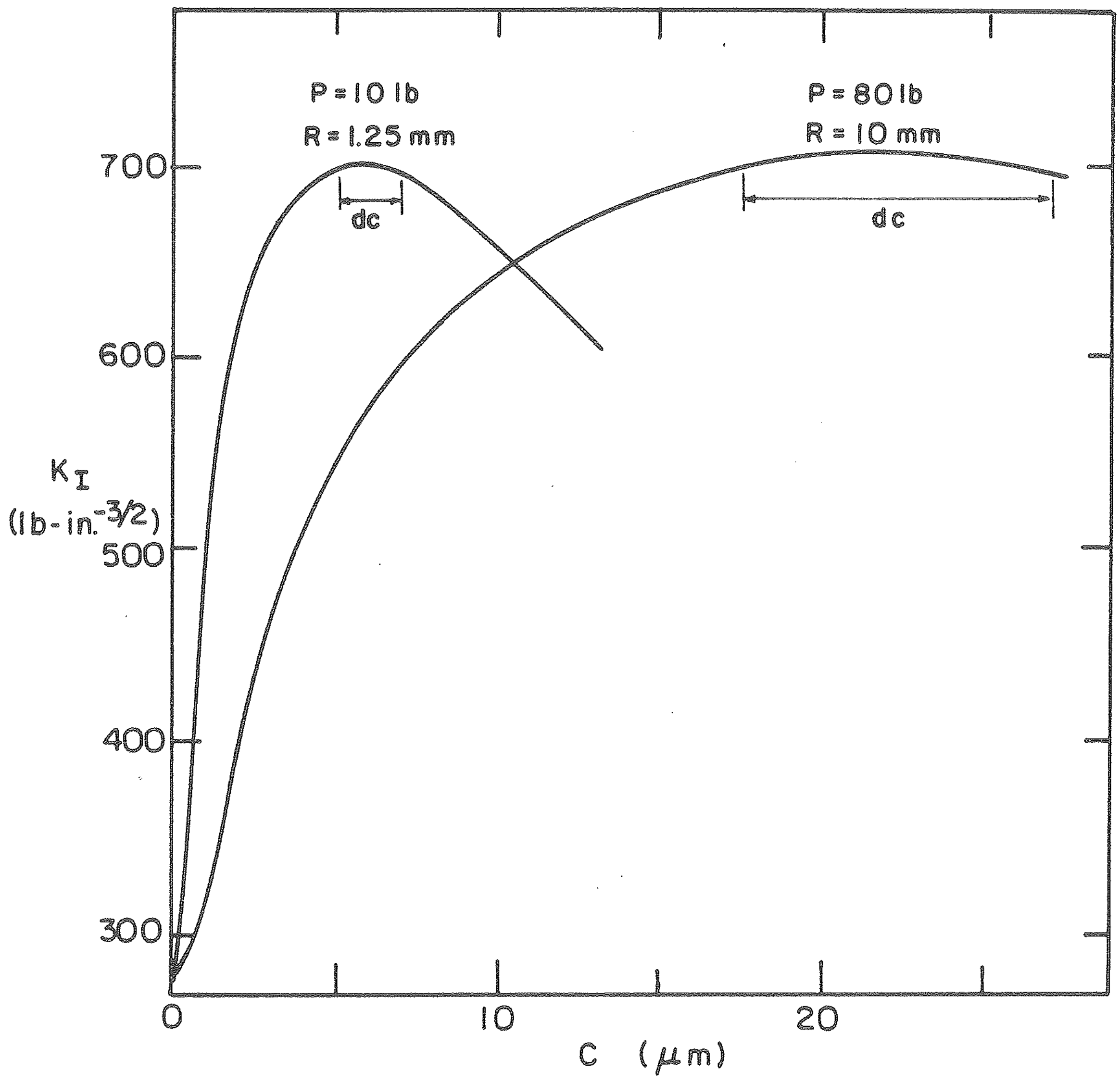

XBL 8010-6217

Fig. 5.14. The stress intensity factor as a function of flaw size. For smaller indenters the stress intensity factor is very sensitive to the size of the available flaws.

As was mentioned, the range of validity of Auerbach's law will depend on Δc, the difference between the size of the largest and smallest flaws present. This has been shown schematically in Fig. 5.15a. If the size of the smallest flaw c_s is taken to be zero, then Δc would be equal to c_L. Assuming that c_L is known, from Eq. (5.9) the largest radius for which Auerbach's relation holds is

$$R_L = \frac{68}{(A\lambda)^{1/2}} c_L^{3/2} \tag{5.11}$$

In Section 5.8 it will be shown that A is proportional to the surface energy γ of the surface. Then Eq. (5.11) suggests that the range of Auerbach behavior should decrease with the square root of γ or equivalently with K_{Ic}. Reduction of this range with K_{Ic} can be seen by comparing the two curves in Fig. 5.16, plotted for two surfaces with the same $\Delta c = 10$ μm but having different fracture toughness. The general trend is schematically shown in Fig. 5.15b.

5.7. Scatter in the Results

It was shown that the size of the surface flaws, even though very small, become comparable to the dimensions of the highly inhomogeneously stressed area. Because of this the complete stress gradient over the flaw had to be taken into account. As a result, it was found that, contrary to the approach often taken in the literature, fracture does not necessarily initiate from the largest flaw. Rather, depending on the materials involved and the indenter size, there is a specific size of flaw c_p from which fracture will start. In the calculations, one

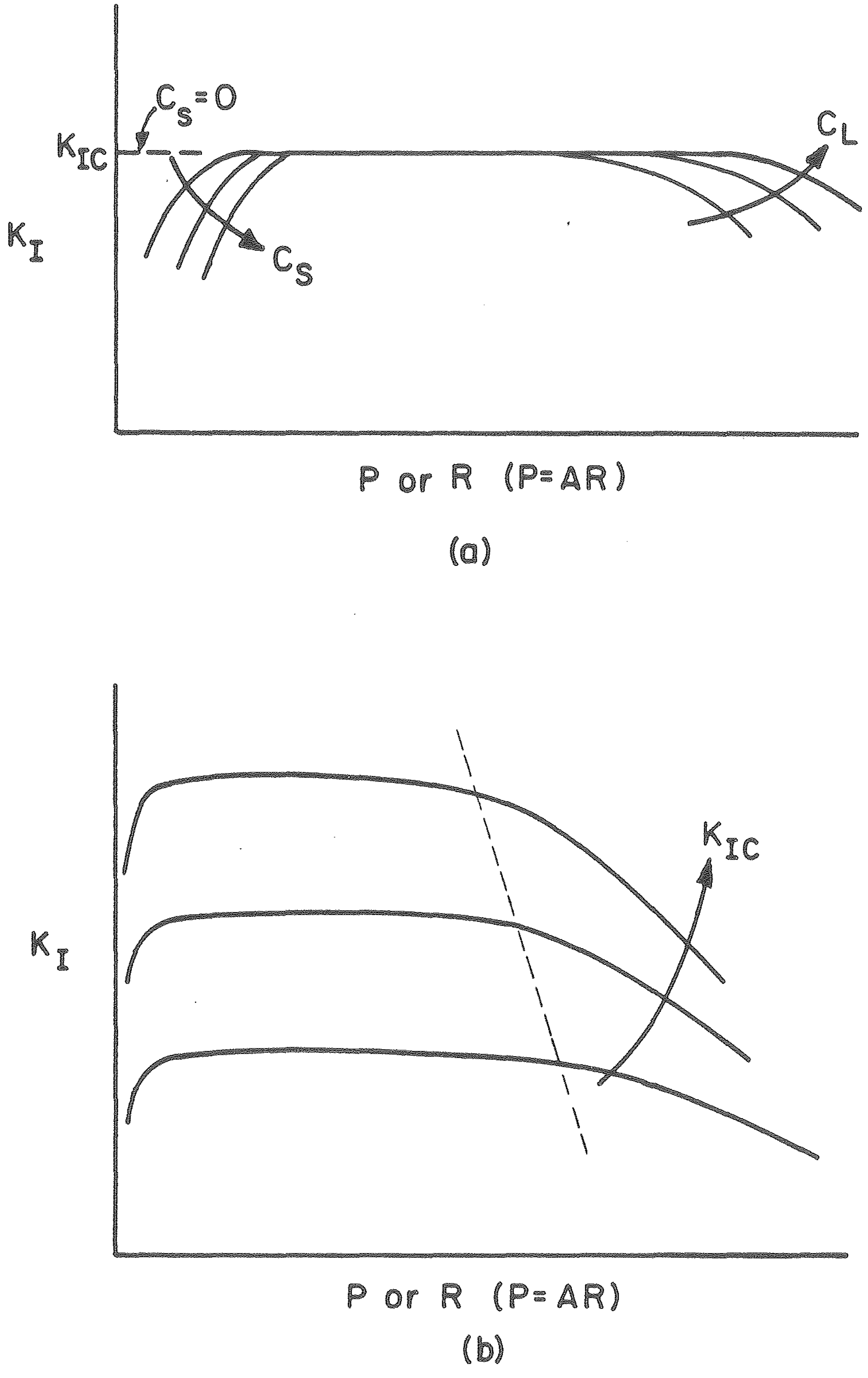

XBL 8010-6219

Fig. 5.15. Schematic variation of the range of validity of the of the Auerbach law showing: a) The effect of the sizes of the smallest and largest flaws, b) the effect of fracture toughness for the same flaw distribution.

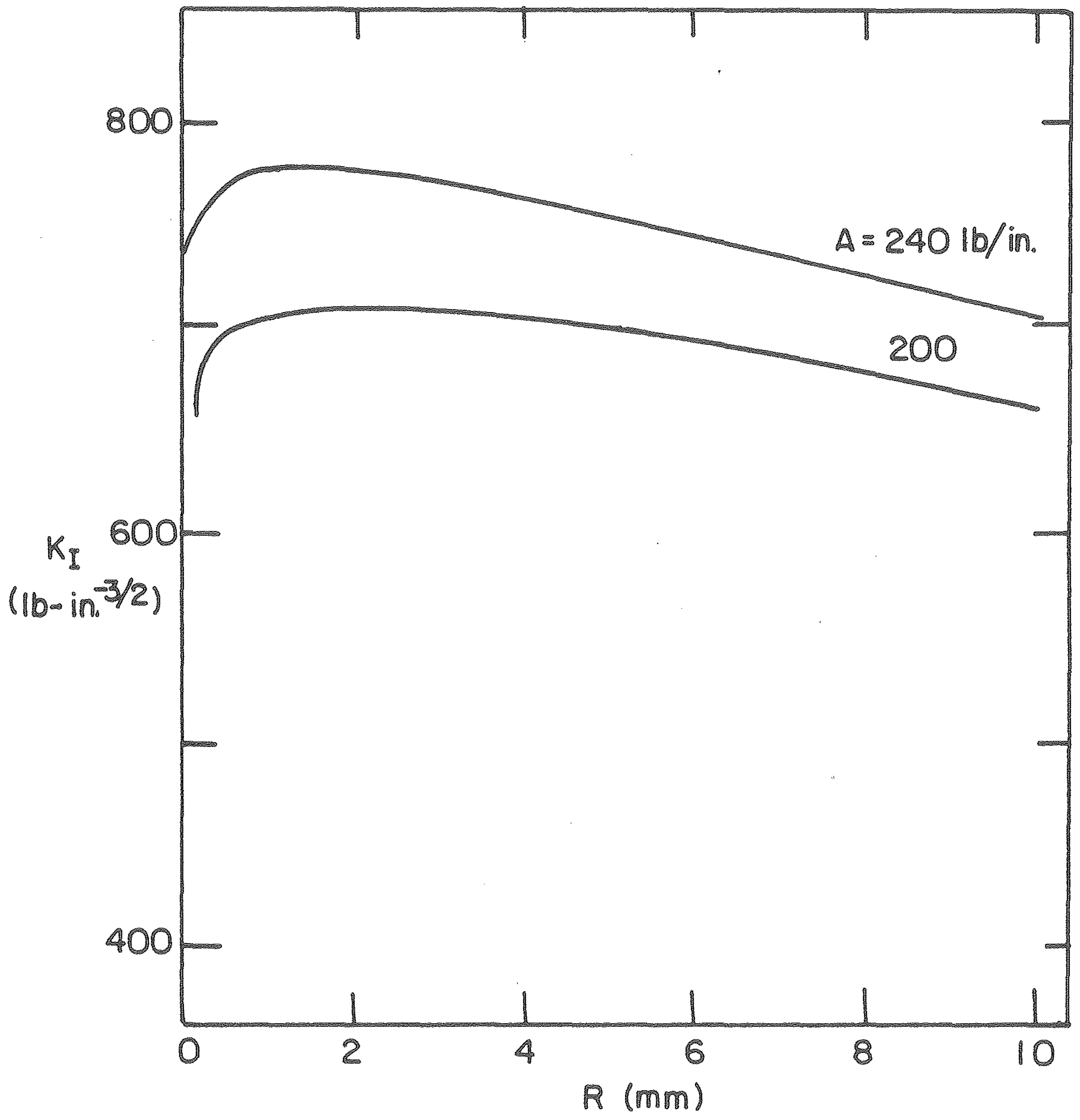

XBL8010-6218

Fig. 5.16. The effect of the Auerbach constant A or equivalently fracture toughness on the range of validity of the Auerbach phenomenon.

assumption was that the favorable or critical size flaw always existed at the location $r = r^*$, where the potential for its propagation was greatest. Using this condition, an expression for the location of fracture r^* and critical fracture load P_c, which eventually leads to the explanation of the Auerbach relation, was obtained.

If, as assumed, the right size flaw could always be found at the desired location, P_c and r^* for a given indenter-surface system would be constants. However, as Figs. 4.7 and 5.6 show, there is a large scatter in P_c and r^* is not always 20 percent larger than the contact radius a. An explanation for the scatter in P_c is not possible by deterministic approaches. Therefore, statistical methods have to be used to account for the fact that the number and location of flaws are randomly distributed on the surface.

The general procedures presented in the literature using Eqs. (4.30) through (4.32) were discussed in Section 4.6. However, in order to apply these equations to any problem the fundamental assumption used in them must be met at all times. That is, the condition for failure at any subdomain must be specifiable solely in terms of the stress and volume elements in the body. This condition would be met if the number of flaws in each uniformly stressed sub volume dv is very high or equivalently their size is very small compared to the dimensions of dv. If so, a constant stress σ at any given point can be held directly responsible for the propagation of flaws in that region. On the other hand, application of these equations is not justified if the size of flaws compared to the dimensions of dv are so large that the criterion for propagation cannot be specified by any given local stress.

We encounter this very rare situation in indentation testing where, because of the very steep stress gradient and small stressed volume, stress alone does not provide an adequate description for failure. This situation necessitated the use of the critical stress-intensity factor, rather than the maximum stress, for specification of a condition for fracture. Therefore, strictly speaking, at each subdomain both stress and flaw size must be known. But if the flaw sizes were known, the use of statistical methods would not be necessary. Fortunately, in this problem, inclusion of all possible flaw sizes and their distribution in the analysis is not necessary. Because, as was discussed in Section 5.5 and shown in Fig. 5.14, fracture for a given indenter radius and surface fracture toughness initiate from only a specific flaw size, c_p. Other flaws with size differing considerably from c_p have a much lower stress intensity and should play no role in fracture. So, the scatter in P_c and the probability of fracture at any given location depends only on the availability or density of flaws with size equal to or close to c_p.

Equation (4.30b) gives the number of flaws N in volume v or, for the case of surface controlled fracture, in area S with strength between 0 and σ. Equation (4.32) for $\sigma_u = 0$ gives

$$N = S(\sigma/\sigma_o)^m \tag{5.12}$$

N can be obtained, for example, from a series of bend tests on similar specimens. Substituting the value $K_{Ic}/Yc^{1/2}$ for σ, from Eq. (5.3) into Eq. (5.12) yields

$$N = S\left(\frac{K_{Ic}}{Y\sigma_o c^{1/2}}\right)^m \tag{5.13}$$

Then the number of flaws n with the size between c and c + dc is,

$$n = S\left(\frac{K_{Ic}}{Y\sigma_o}\right)^m \left[\frac{1}{c^{m/2}} - \frac{1}{(c + dc)^{m/2}}\right] \tag{5.14}$$

Using Taylor series expansion on the above, and neglecting terms of higher-order, results in

$$n \approx S\left(\frac{K_{Ic}}{Y\sigma_o}\right)^m c^{-\left(\frac{m}{2} + 1\right)} dc \tag{5.15}$$

Substituting for c from Eq. (5.9) gives a relation between n and R

$$n \approx S\left(\frac{K_{Ic}}{Y\sigma_o}\right)^m [0.06(Ak)^{1/3}]^{-\frac{m}{2} + 1} R^{-\frac{(m+2)}{3}} dc \tag{5.16}$$

Here, dc is the range of flaw sizes that for a given R would result in about the same stress intensity as the critical flaw. According to Figs. 5.14 and 5.17, the range of crack sizes dc corresponding to 5 percent variation in K_{Ic} increases almost linearly with the radius R So, Eq. (5.16) becomes

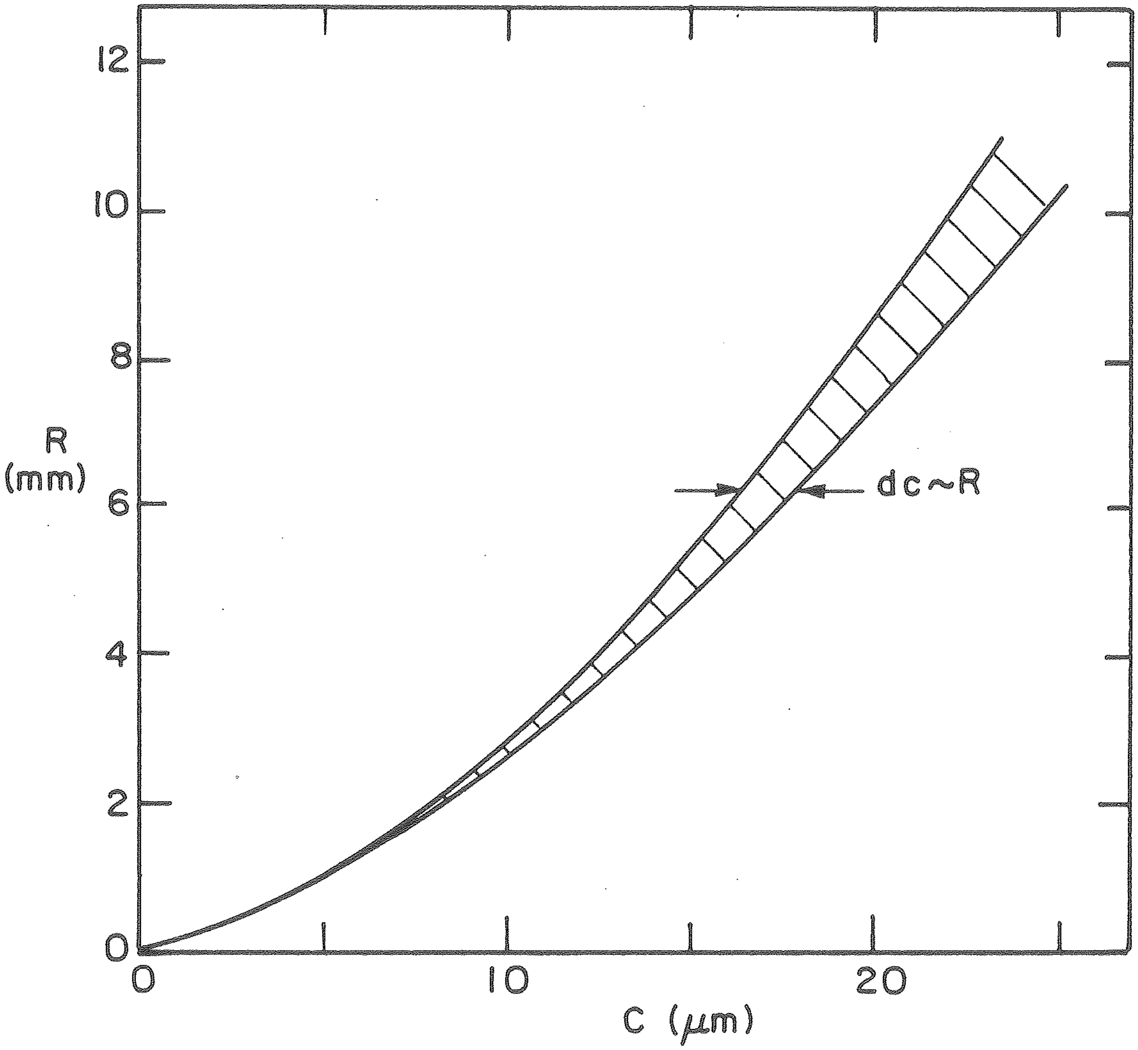

XBL 8010-6220

Fig. 5.17. The range of flaw sizes dc that for a given indenter radius R give a stress intensity factor of about 600 lb-in.$^{-3/2}$.

$$n \approx S\,B\,R^{-\frac{m-1}{3}} \tag{5.17}$$

where B is the product of terms in Eq. (5.16) not involving R. Since m is a number that is usually greater than at least 3,[47] Eq. (5.17) shows that the density of critical flaws for larger indenters is lower than that for the smaller ones.

If we assume that the area involved is

$$S = 2\pi a dr \tag{5.18a}$$

Using Eqs. (4.1) and (4.23) to eliminate a results in

$$S = 2\pi\lambda^{1/3}R^{2/3}\ dr \tag{5.18b}$$

Substituting S into Eqs. (5.17) gives

$$n \approx B'R^{-\frac{m}{3}+1}\ dr \tag{5.19}$$

Then, for a constant radial distance along the surface dr, and $m > 3$, the number of critical flaws or the probability of finding one decreases as R is increased. Reduction in the probability of finding the right flaw reflects itself in a high scatter of P_c. Also the lack of large enough flaws, in the average, makes it necessary that higher loads than $P \approx AR$ to be required for fracture as larger R are used. This means that the power or R in $P \approx AR$ relation will gradually become larger than one as indenters of larger radii are used. Finally, outside the Auerbach region where the probability of finding c_p becomes zero, the power of R becomes two. Also, due to higher mean loads the c/a ratio and consequently r*/a reduces.

These predictions agree quite well with the experimental results, which further emphasizes the validity of the arguments used.

5.8. Development of the Cone Crack

So far, the focus of this study has been centered around initiation of ring cracks under quasistatic loading conditions by spherical indenters in the elastic response regime. Most importantly, relations between the fracture load and surface variables for different size indenters were obtained. These relations can also be used for low velocity impact testing, where wave propagation effects can be neglected. In this section propagation subsequent to initiation of fracture from a surface flaw to form a full cone crack is examined, and a complete load-crack-size diagram is obtained. As a result, the value of the Auerbach constant A and consequently the critical velocity for initiation of fracture are calculated.

General experimental observations regarding formation of cone cracks were discussed in Section 3.3. The direction along which the cone propagates needs to be known to calculate the extent of propagation. If cracks propagate along or close to the prior principal stress trajectories (PST), the effort for calculating the stress intensity factor would be significantly reduced. Observation of cone cracks and calculations of PST from the Hertz equations show that the crack makes a somewhat greater angle θ with the Z axis than the angle of PST starting from the same location. In Table 3, values of θ obtained from PST, which depend only on the value of the surface Poissons ratio ν, are compared with those obtained experimentally.

As Table 3 shows, for all cases the observed values of θ are somewhat above those expected from the PST unless very large values of Poisson's ratio are invoked. The reason for this deviation can be traced to the fact that during propagation only one side of the crack is stressed, while the other side is stress free. This lack of symmetry in loading will cause shear stresses to develop across the crack plane, and since maximum energy release rate is associated with mode I propagation rather than a mixture of mode I and Mode II, cracks will propagate in the direction of the new principal stress trajectory which appears to make larger angles with the Z axis. The maximum angle of deviation as given in Table 3 is about 10°. The relation between K_I, K_{II}, and the angle β that the maximum hoop stress at the crack tip makes with the direction of the crack, namely[72]

$$K_I/K_{II} = \frac{3\cos\beta - 1}{\sin\beta} \tag{5.20}$$

can be used to obtain an estimate of the magnitude of the shear stresses that exist. From Eq. (5.20) a deviation of 10° from propagation in the direction of the crack requires a shear stress of about 8 percent of the normal stress. This magnitude of shear stress, however, as shown by Erdogan and Sih,[72] even though it causes noticeable

Table 3.

By	Material	ν	θ	PST (no friction)
Roesler	Steel Punch on glass	0.25	68.5	59.5
Finnie and Vaidyanathan	W. C. Punch on pyrex	0.22	72	57
Finnie and Vaidyanathan	Same as above but lubricated	0.22	68	57
Finnie and Vaidyanathan	Steel sphere on glass	0.25	68	60.2
Wilshaw	Steel sphere on glass	0.25	71	60.2

change in the direction of propagation, does not effect very much the magnitude of the normal stress required for propagation of the crack. So, the condition for propagation can still be satisfied by considering only the prior normal stresses and ignoring the newly developed shear stresses. Such a method was first used by Frank and Lawn[51] to obtain the load crack length relation. But, as mentioned earlier, their deriation suffers from the assumption that initiation occurs on the surface on the location of maximum stress. Other than for very small c/a values, this assumption is inaccurate and leads to inconsistent results. Evans[45] showed that for $1 < c/a < 3$ the location of fracture has a significant effect on the c vs P curve. In view of this fact, the most likely value for r*/a, namely 1.2, will be used here.

Figure 5.12 shows a P vs c relation plotted for a specific value of R and K_{Ic}. However, as shown in Fig. 5.18, it can be generalized by non-dimensionalizing c and c/a and P as $P/R\lambda K_I^2$. For $c/a > 2$ it has been found[3] both experimentally and analytically that the length of the cone crack increases with load as $P^{2/3}$. For the range of $0.1 < c/a < 2$ since the crack drastically changes its direction calculations are more difficult. Therefore, the curve for this range is plotted by extrapolation. From this figure it is apparent that a flaw, depending on its location on this curve, can either propagate unstably or stably.

Unstable growth occurs when at the time of fracture c/a is less than 0.025. The region in which this unstable growth occurs is marked I in Fig. 5.18. After propagation, cracks finally become arrested due to diminishing stresses when they reach a depth equal to that shown in

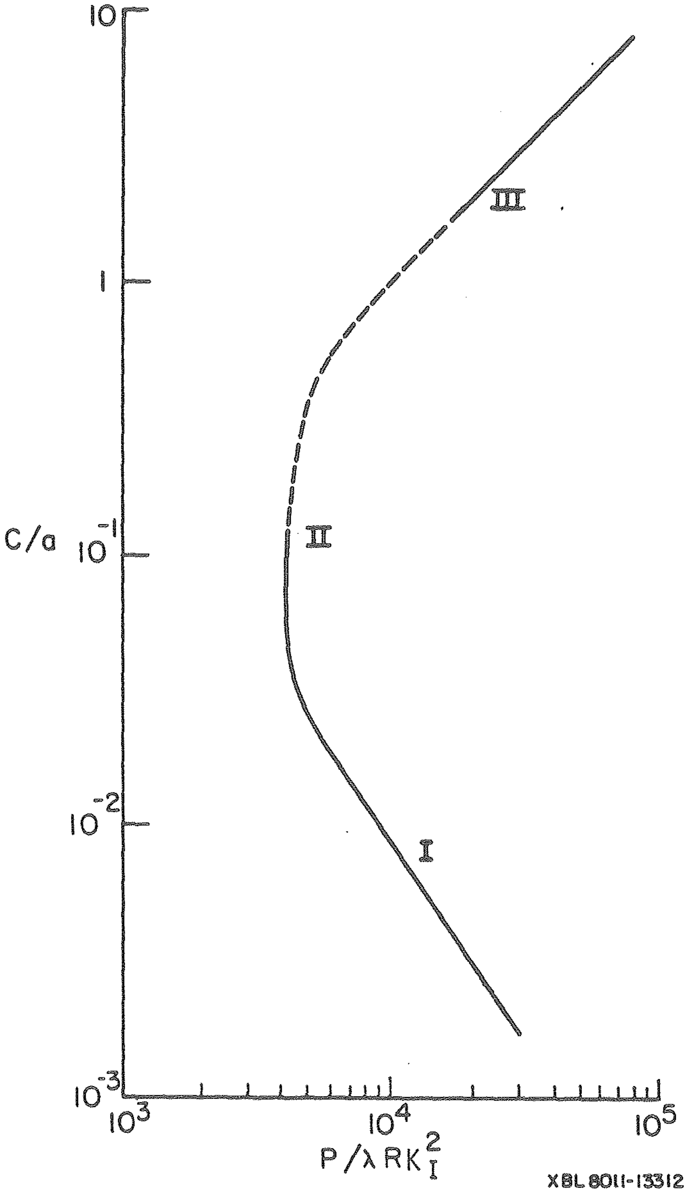

Fig. 5.18. Dimensionless crack length parameter, c/a, versus dimensionless load parameter, $P/(\lambda RK_I^2)$.

region III, corresponding to the same $P/R\lambda K_I^2$ value at which fracture started. Beyond this stable cracks grow slowly and stably with increasing load. However, the onset of fracture on an as-received surface occurs for c/a values between 0.03–0.10, which corresponds to the lower portion of region II. As shown in Fig. 5.18, depending on c/a, crack growth in region II is stable but a slight increase in load leads to extensive crack propagation. In this region a flaw with normalized size of $c/a \approx 0.06$ has the highest probability for propagation because it corresponds to the lowest load. So the minimum possible load for propagation of a flaw is

$$P/R\lambda K_I^2 \approx 4100 \tag{5.21}$$

This equation shows that the critical load for fracture P_{cr} is proportional to the radius and the constant of proportionality, the Auerbach constant A, is

$$P_{cr}/R = A \approx 4100\ \lambda\ K_{Ic}^2 \tag{5.22}$$

Equation (5.22) indicates that there exists a linear proportionality between A and the value of surface energy γ. Eliminating P from Eqs. (4.5) and (5.22) gives the lower bound on the particle velocity for onset of damage

$$V_{cr} \approx 450\left(\frac{\gamma}{\rho_p}\right)^{1/2}\left(\frac{\lambda K_{Ic}^2}{R}\right)^{5/6} \tag{5.23}$$

Equations (5.22) and (5.23) which show no dependency on c are valid for undamaged surfaces where the c/a ratio lies somewhere between 0.03-0.10. However, as shown in Figs. 4.6 and 4.7, abrading the surface results in a significant increase in A. There are two reasons for this observation. First, abrading effectively shifts the range of c/a to higher values on region II of Fig. 5.16. In this region $P/R\lambda K_{Ic}^2$, for a narrower range of c/a values, can still be considered a constant, but of larger magnitude. Second, the flaw geometry parameter Y, given by Eq. (5.3), is smaller for wedge-type scribing marks produced by abrading the surface than for flaws. Therefore, higher loads must be applied to compensate for loss of "sharpness" of the surface flaws.

6. ANALYSIS OF THE EROSION OF BRITTLE MATERIALS— A HISTORICAL BACKGROUND

Literature on this subject dates back to the 1800's when attention was given to determining the force due to impact of two bodies and the critical velocity beyond which irreversible damage occurs. Until late in the 19th century impact studies considered mainly the motion of the centers of gravity of the bodies and very little attention was paid to what actually happens at the point of contact. In 1873, Reynolds[73] studied the contact between two elastic bodies and came to the following conclusions:

1. The intensity of the pressure between bodies on first impact is independent of the size of the bodies.
2. A soft body may cause pressure sufficient to crush a hard body.

These conclusions which were derived from the incompressible fluid laws and every approximate elastic stress analysis are crude and do not precisely represent the contact forces and stresses of two impacting elastic bodies. Later, in 1881, Hertz,[35] as discussed in Chapter 4, solved the contact problem of two spherical elastic bodies. However, extensive analytical modeling of the erosion process using these and other solutions was not attempted until the mid 1960's.[47] After this period a great deal of elaborate theoretical and experimental work appeared in the literature which provided more insight into the problem as well as creating more questions. Prior to this time more emphasis was placed on experimental evaluation of the effect of variables, such as particle type, shape, velocity and radius as well as target material properties on erosion. Early investigators recognized that all of these factors were of importance in wear.

Haworth's (1949)[74] investigation on the resistance of iron and steel to the cutting and rubbing action of quartz and alumina abrasives showed that both the shape and the hardness of the abrasive particles were important. Angular particles were found to be more abrasive than rounded particles of the same material. Abrasiveness increased with hardness for particles with similar shapes.

Stoker (1949)[75] who was concerned with erosion of fluid type catalytic cracking plants observed a pronounced dependency of erosion rate on particle velocity and impingment angle. He found that the erosion rate of a brittle gypsum plaster target varied as the cube of the velocity of the air which entrained the particles. The maximum erosion rate occurred at a 90° impingment angle for gypsum while for black iron eroded with silica particles the maximum was at 20°.

Finnie (1956),[76] employing photographic techniques with a high speed light source, was the first to measure the velocity of eroding particles. He found that the weight loss of an annealed steel target was approximately proportional to the square of the speed of the eroding particles. As a consequence of his studies, he developed a mathematical model to predict the erosion of ductile materials.

From these and other studies that followed it was generally agreed that material removal rate W (grams removed per gram of eroding particle) varies with the particle radius R and velocity V as

$$W = QR^{a}V^{b} \qquad (6.1)$$

where a, b, and Q are constants which depend on the material properties of both the particle and the surface and most importantly the type of contact response as discussed in Chapter 2. Values reported for these constants by different investigators vary. But generally for brittle materials, a lies between 3 and 4.5 and b between 2 and 3.3. Various responses arising from impact and quasi static indentation were discussed in Chapter 2. Those responses relevant to brittle materials, namely elastic and elastic-plastic, will be further discussed here.

6.1. Elastic Response

Complete elastic interaction may occur by low velocity impact of relatively large blunt particles on brittle surfaces. It was shown by Sheldon and Finnie[77] that the particle radius has to be greater than a certain value so that plastic deformation does not precede fracture. Using the present notation it may be shown that this radius is $A/\lambda(\pi H)^3$. Also, the particle velocity should be greater than V_c, given by Eq. (5.23), as derived in Chapter 5, for the initiation of fracture. In this case erosion damage initiates by ring crack formation like those shown in Fig. 3.5.

Sheldon and Finnie (1965)[47] using the Weibull formulation estimated the radius a^* to which fracture extends on the surface. Then, erosion was related to the cylindrical volume described by the radius a* and the maximum depth of particle penetration. For spherical indenters they found

$$a = \frac{3m}{m - 2} \quad , \quad b = 2.4 \frac{m}{m - 2} \tag{6.2}$$

and for angular particles

$$a = 3.6 \frac{m}{m - 2} \quad , \quad b = 2.4 \frac{m}{m - 2} \tag{6.3}$$

where m is the flaw parameter of the Weibull fracture strength distribution and is assumed to be constant for a given material. The general agreement between prediction and experiment is surprisingly satisfactory considering the various assumptions made in the analysis.

Oh et al. (1972)[78] extended the approach suggested by Sheldon and Finnie and related the erosion to the damaged volume enclosed in the spherical cap of radius R* and depth S.

$$W \sim S^2 R^* \tag{6.4}$$

where R* is considered to be the radius of a much larger indenter than the actual particle which on the average produces a ring crack at radius a*. For Eq. (6.4) S was assumed to be proportional to the depth of indentation. However, based upon observations of single indentation they suggested a better approximation for the depth of the cone crack was

$$S \sim \frac{P^{5/6}}{R^{1/3} K_{Ic}^{2/3} E_s^{1/6}} \tag{6.5}$$

Using Eq. (6.5) and their derivation for R*, Eq. (6.4) can be expressed in the following form

$$W \sim \frac{\rho\lambda V^{\left(2+0.8\,\frac{m+2}{m-2}\right)} R^{\left(\frac{8}{3}+\frac{m+2}{m-2}\right)}}{K_{Ic}^{4/3} E_s^{1/3}} \qquad (6.6)$$

The predictions of radius and velocity exponents from Eq. (6.6) are close to those obtained by using S proportional to the depth of indentation and, except for glass, are again close to the experimental values reported by Sheldon and Finnie[47] for a wide range of materials. Also, the effect of K_{Ic} on erosion indicated by this approximate relation is the same as that Evans and Wilshaw (next section) obtained for the elastic plastic response regime.

Up to the late 1960's eroded surfaces were examined mostly with light microscopy. The development of the scanning electron microscope (SEM) provided a much better tool for further study of the erosion mechanisms which may vary substantially from one material to the other. Adler (1974)[71] using both light microscopy and SEM studied the events that occur during particle impact on glass and found that, as expected, the diameter of the ring cracks and the geometry of the conical fracture extending into the bulk material depends on particle size, velocity and surface material properties. Additional impacts in the vicinity of this region produced some subsurface damage as well as other cone cracks. It is only after a number of impacts have occurred that removal of material exterior to the conical frustrums take place. Both Adler and more recently Sargent et al. (1979)[68] developed similar models based on material removal by cone crack interaction.

Sargent et al. derived the following equations for particle size and velocity effects on erosion

$$W \sim R^{\frac{2}{3}i} (R^{4/3} - Ro^{2/3} R^{2/3})^{j} \qquad (6.4)$$

where $i + j = 3$ and

$$Ro = A\lambda^{2/3} \frac{5}{3} r\rho^{3/5} V^{6/5}$$

A is the Auerbach constant, and i and j exponents depend on the particle radius and velocity, but no specific values were given.

Removal of the interstitial material between the cones leaves a dense distribution of solid frustrums protruding from the surface. The material contained in the frustrums formed by conical fracture is more resistant to erosive attack than the highly fractured interstitial material. Thus erosion rate slows down during this stage after high rate of removal of the interstitial material. Finally, in the steady state phase removal of highly fractured and irregular surface of bulk material takes place at a uniform rate. Thus, erosion rate is very slow during initial stages when cone cracks are forming, then increases sharply due to interestitial material removal when cones start to interact with one another. Removal of the cone frustrum slows down the erosion rate until the steady state stage is reached.

To study this removal process experiments were carried out using pyrex glass impacted with 280 and 660 μm steel shot at 40 m/sec. The results are shown in Fig. 6.1. In other experiments, surfaces already eroded with 280 μm particles at 40 and 60 msec were again eroded with 660 μm particles at 40 m/sec to find the effect of surface condition on erosion and its mechanism. As shown in Fig. 6.2, contrary to previous results, the erosion rate is very slow and increases gradually until it reaches the steady state phase. These results indicate that cone crack formation may not play a significant role in materials removal when the surface is highly damaged. So, these erosion models that are based upon cone interaction and interstitial material removal while describing initial behavior may not be realistic for the steady state phase of erosion of bulk brittle materials. On the other hand, the study of the erosion of NiO by Zambelli and Finnie (1978)[81] clearly shows the importance of cone crack formation and interaction to material removal. Unfortunately, no information is available on the complicated mechanism of removal of highly fractured surface.

6.2. Elastic-Plastic Response

The possibility of plastic deformation in brittle materials which was clearly demonstrated after the development of SEM and TEM was discussed in Chapter 2. Based upon an extensive study of the details of damage under both static and dynamic conditions Evans and Wilshaw[31,32] and Evans et al.[22] formulated two semi-empirical relations for the upper bound on material removal per particle. These relations are obtained

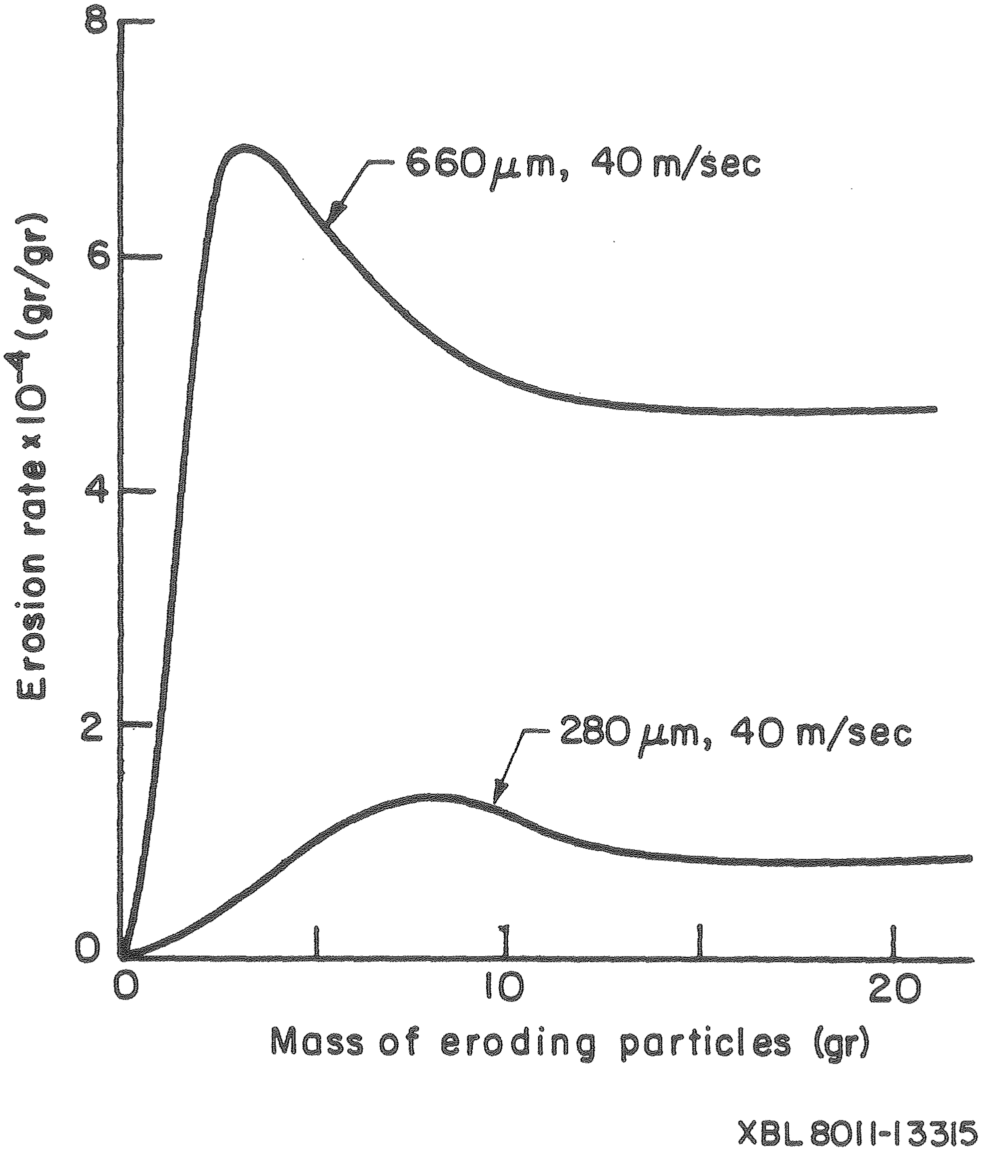

Fig. 6.1. Erosion of Pyrex glass with steel shot.

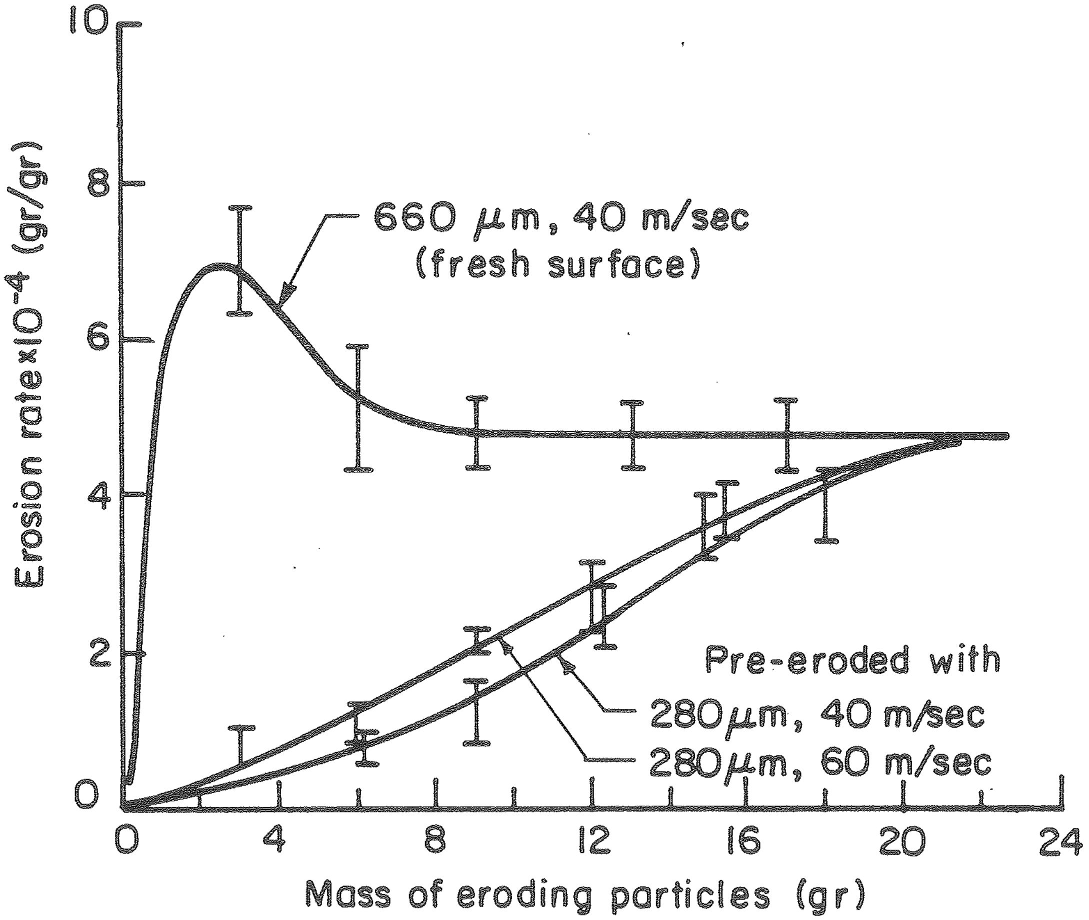

XBL 8011-13314

Fig. 6.2. Effect of surface condition on the erosion of Pyrex glass with 660 μm steel shot at 40 m/sec.

from dimensional analysis, the approximate nature of the stress field, and fracture consideration of the indentation process. Also an approximate analysis of the impact dynamics and fracture mechanics was done for high velocity impacts where quasi-static approximations no longer suffice.

The upper bound for material removal due to low or high velocity impact is assumed to be

$$W \sim c_1^2\, h \tag{6.5}$$

where c_1 is the length of lateral cracks located at an average depth h below the surface. For quasistatic conditions, c_1 is given by Eq. (3.9) and h was found to be nearly proportional to the radius of contact a in Eq. (3.3). By substituting these values into Eq. (6.5) the following results

$$W \sim \frac{P^2}{K_{Ic}^{3.2} H^{1/2}} \tag{6.6}$$

For impact velocities where the resulting force is less than 10 times the load at which fracture initiates, Eq. (3.2), a relation between impact load P and velocity was obtained

$$\frac{P}{R^2 G} = 4.6\left(\frac{\rho V^2}{G}\right)^{3/5} \tag{6.7}$$

where G is the shear modulus of the target material, and ρ is the density of the impacting particle. By Substituting P from Eq. (6.7) into Eq. (6.6), the weight loss for N impacts is predicted to be

$$W \sim NR^4G^{4/5}V^{12/5}\rho^{6/5}/K_{Ic}^{3/2}H^{1/2} \tag{6.8}$$

Due to high strain rates under impact condition dynamic values of K_{Ic} and H should be used in Eq. (6.8).

For high impact velocities it was found that the dimensions of the lateral cracks are nearly proportional to the radial crack size given by Eq. (3.8) and the following relation was derived for their mean depth,

$$h \sim (R^2V\ \rho/H)^{1/2} \tag{6.9}$$

Then Eq. (6.5) becomes

$$W \sim \frac{V^{19/6}R^{11/3}\rho^{1/4}}{K_{Ic}^{4/3}H^{1/4}} \tag{6.10}$$

Ruff and Weiderhorn (1979)[82] suggested the following relation for the depth of the lateral cracks

$$h \sim \left(\frac{\rho R^3V^2}{H}\right)^{1/3} \tag{6.11}$$

and by using $C_l \sim C_r$ from Eq. (3.8) they obtained

$$W \sim \frac{\rho^{11/9}R^{11/3}V^{22/9}}{K_{Ic}^{4/3}}\ H^{1/9} \tag{6.11}$$

Even though hardness appears as a rather weak parameter in Eqs. (6.10) and (6.12) a contradiction about its effect exist. Gulden's data,[79] however, indicate that Eq. (6.10) provides a better representation of the effect of K_{Ic} and H on erosion. But the exponents of R and V from all above equations, considering their approximate nature, are very close to those found experimentally.[47] The exponents of these variables in the erosion equations are summarized in Table 4.

Radius exponents obtained by eroding MgO, Al_2O_3, graphite, glass, and hardened steel with SiC particles lie between 3.7–4.1. while the velocity exponents are between 2.65–3.0.[47] These values are reasonably close to the theoretical predictions and their variation,

Table 4. The exponents of R and V for elastic response are calculated for m = 5 and 15. Higher values correspond to m = 5.

	Type of Response	R	V	K_{Ic}	H
Sheldon, Finnie[47]	elastic	5 3.46	4.0 2.77		
Oh, et al.[78]	elastic	4.33 3.3	3.47 2.65		
Modified, Oh, et al.	elastic	4.9 3.9	3.87 3.04	-1.33	
Evans, Wilshaw[32]	elastic-plastic (quasistatic)	4.0	2.4	-1.5	-0.5
Evans, et al.[22,31]	elastic plastic (dynamic)	3.67	3.16	-1.33	-0.25
Wiederhorn, Ruff[82]	elastic-plastic	3.67	2.45	-1.33	0.11

considering the scatter of the experimental results, is not very large. So, in most cases, a reasonable expression for erosion can be obtained by using 4 and 3 for the radius and velocity exponents, respectively.

The effect of elastic properties of materials predicted by the proposed equations is complicated. However, examination of these equations reveal that they have a second order effect compared to fracture toughness. Therefore, as far as material properties are concerned, the erosive resistance of a brittle material is primarily determined by its fracture toughness.

7. SUMMARY AND CONCLUSIONS

An examination of the behavior of brittle materials reveals that their brittleness is only a state rather than a property. When used as components of large structures they fail in a brittle manner, while ductile behavior may be observed when the size of the stressed area becomes small. The critical size at which this transition occurs is determined by two factors: hardness and the state of stress in the material. The first variable is a material property while the state of stress, on the other hand, is determined by external factors such as the shape of the indenter or particle. Plasticity occurs whenever sharp indenters are used. With blunt indenters there exists a transition zone between elastic and plastic responses with changing hardness and its range increases with increasing indenter size.

This transition in behavior has necessitated the development of elastic and elastic-plastic analyses when studying indentation or erosion. The Hertz solution has been used extensively for the elastic contact problem and it has been found consistently that its application, with a maximum tensile stress theory of failure, leads to incorrect prediction of both the fracture load and the fracture location. Because of the importance of the problem there have been many attempts, as discussed in Chapter 4, to resolve the differences that exist between the theoretical predictions and experimental results. Almost all treatments by various investigators have used the magnitude of the surface radial stress as a condition for fracture. In this study it was found that the application of the maximum stress theory for fracture to the indentation problem can be erroneous due to the large variation of stresses over a typical surface flaw. Thus, the maximum stress intensity failure criterion was used to allow for the variation of the surface flaw sizes and the stress gradient that flaws are exposed to.

It was found that for every flaw with size c there is a critical distance r* from the contact center where the stress intensity factor is highest. The distance r* increases with increasing c. However, fracture on a surface having various size flaws initiates from a flaw with the size of $c \approx 0.06a$ at $r^* \approx 1.2a$, where a is the radius of contact. This condition corresponds to the minimum load required for fracture which was shown to be proportional to the indenter radius. These results allow indentation testing to be used to measure surface properties such as fracture toughness and flaw size. Also, the analysis could be used as a basis for predicting the resistance of materials to damage by low velocity particle impact and indentation in the elastic response regime. However, the rate of material removal after initiation of damage needs a separate analysis.

Sequential photography shows that the material removal by particle impact is a very complicated process. Since not all the events that occur can be accounted for erosion analyses are usually based upon the most likely and significant types of cracking that occur during single particle impact on undamaged surfaces. Therefore, by relating the impact load to an assumed damaged volume produced by the extension of these cracks a qualitative prediction of material removal can be presented. However, there is no solid evidence available to indicate that any of the proposed models represent or remain valid during the steady state phase of erosion. In fact, from the indentation and erosion experiments that were done on both glass and alumina no significant resemblance between the eroded and indented surfaces was found.

Erosion experiments reveal that the rate of material removal from an undamaged surface is much higher than that of a damaged one when the contact is elastic. However, to a lesser degree, quite the opposite results for the elastic-plastic contact.[84] This again emphasizes the significant difference that exist between these two types of response. Since the analysis for either case relates the material removal to the maximum damaged volume caused by single impacts, usually an upper limit of material removal can be expected. From these analysis the general conclusion that can be drawn on the effect of material properties on the erosive resistivity of brittle materials is that the fracture toughness plays the most important role. Hardness for the elastic-plastic response and elastic properties for either response have a second order effect to that of fracture toughness.

APPENDIX A

The stresses associated with a Hertzian loading situation (expressed in Cartesian Coordinates) along the plane x = 0 (plane containing z and r axis shown in Fig. 5.1). We note that $\sigma_{yy} = \sigma_{rr}$.

$$\sigma_{xx} = -1.5\ \mathrm{Pm} \left\{ \frac{(1-2\nu)a^2}{3r^2} \Big[1 - \left(\frac{z}{\sqrt{u}}\right)^3 + \frac{z}{\sqrt{u}} \right.$$

$$\left. \left[2\nu + \frac{(1-\nu)u}{a^2+u} - \frac{(1+\nu)\sqrt{u}}{a} \ \mathrm{arc\ tan}\ \frac{a}{\sqrt{u}} \right] \right\} \qquad \text{(A-1)}$$

$$\sigma_{yy} = 1.5\ \mathrm{Pm} \left\{ \frac{(1-2\nu)a^2}{3r^2} \left[1 - \left(\frac{z}{\sqrt{u}}\right)^3 \right] + \left(\frac{z}{\sqrt{u}}\right)^3 \frac{a^2u}{u^2+a^2z^2} \right. \qquad \text{(A-2)}$$

$$\left. + \frac{z}{\sqrt{u}} \left[\frac{(1-\nu)u}{a^2+u} + \frac{(1+\nu)\sqrt{u}}{a} \ \mathrm{arc\ tan}\ \frac{a}{\sqrt{u}} - 2 \right] \right\} \qquad \text{(A-3)}$$

$$\sigma_{zz} = 1.5\ \mathrm{Pm} \left(\frac{z}{\sqrt{u}}\right)^3 \frac{a^2u}{u^2+a^2z^2}$$

$$\sigma_{yz} = 1.5\ \mathrm{Pm}\ \frac{rz^2}{u^2+a^2z^2}\ \frac{a^2\sqrt{u}}{a^2+u} \qquad \text{(A-4)}$$

where

$$u = \frac{1}{2}\left(r^2 + z^2 - a^2 + \sqrt{(r^2z^2-a^2)^2+4a^2z^2} \right)$$

The values of σ_{rr} near the surface where fracture starts from a flaw are equal to σ_{yy}.

REFERENCES

1. Weibull, W., "A Statistical Theory of the Strength of Materials," Ing. vetenskaps Akad. Handl., No. 151 (1939).
2. Shandl, E. B., Glass Engineering Handbook, 2nd Edition, McGraw Hill, New York (1958).
3. Roesler, F. C., "Brittle Fracture near Equilibrium," Proc. Phys. Soc. B69, 981 (1956).
4. Griffith, A. A., "The Phenomena of Rupture and Flaw in Solids," Phil. Trans. of the Royal Society A221, 163 (1920).
5. Dalladay, A. J., and Twyman, F., "Some Measurements of the Stress Produced at the Surface of Glass by Grinding with Loose Abrasives," Trans. Opt. Soc. 23, 170 (1921).
6. Holland, A. J., and Turner, W. E. S., "The Effect of Transverse Scratches on the Strength of Sheet Glass," J. Soc. Glass Tech. 21, 383 (1937).
7. Yust, C. S., Oak Ridge National Lab., private communication.
8. Mayville, R., "Erosion of Ductile Materials," M. S. Thesis, University of California, Berkeley (1977).
9. Gohlhoff, G., and Thomas, M., The Physical Properties of Glass, Z. Tech. Phys. 7, 105 (1926).
10. Joos, P., Uber die Mikroharte von Glasoberflachen, Z. Angew Phys. 9, 556 (1957).
11. Bridgeman, P. W., Simon, I., "Effect of very High Pressures on Glass," J. Appl. Phys. 24, 405 (1953).
12. Hutchings, I. M., "Strain Rate Effects in Microparticle Impact," J. Phys. D: Appl. Phys. 10, 179 (1977).

13. Hockey, B. J., and Wiederhorn, S. M., "Erosion of Ceramic Materials," Proc. 5th Intern. Conf. on Erosion by Solid and Liquid Impact (1979).

14. Recht, R. F., "Catastrophic Thermoplastic Shear," J. Appl. Mech. 86E, 189 (1964).

15. Yust, C. S., and Crouse, R. S., "Melting at Particle Impact Sites during Erosion of Ceramics," Wear 51, 193 (1978).

16. Gilman, J. J., and Johnson, W. G., "Dislocations and the Mechanical Properties of Crystal," Wiley, New York (1957).

17. Stokes, R. J., Johnson, T. L., and Li, E. H., "Effect of Surface Condition on the Initation of Plastic Flow in Magnesium Oxide," Trans. Met. Soc. AIME 215, 437 (1959).

18. Hockey, B. J., "Plastic Deformation of Alumina Oxide by Indentation and Abrasion," J. Am. Cer. Soc. 54, 223 (1971).

19. Lankford, J., "Compressive and Indentation Damage in Alumina," ONR Tech. Report (1977).

20. Finnie, I., "The Mechanism of Erosion of Ductile Metals," Proc. of the 3rd U. S. Natl. Congress of Appl. Mech. 527 (1958).

21. Capesius, M., "Crack Formation in Glass Under Spherical Indenters," M. S. Project, University of California, Berkeley (1970).

22. Evans, A. G., Gulden, M. E., and Rosenblatt, M., "Impact Damage in Brittle Materials in the Elastic-Plastic Response Regime," Proc. R. Soc. London A. 361, 343 (1978).

23. Lawn, B. R. and Wiederhorn, S. M., "Strength Degradation of Glass Impacted with Sharp Particles," J. Am. Cer. Soc. 62, 66 (1979).

24. Lawn, B., and Wilshaw, R., "Review of Indentation Fracture: Principles and Applications," J. of Mat. Sci. 10, 1049 (1975).

25. Hamilton, G. M., and Goodman, L. E., "The Stress Field Created by A Circular Sliding Contact," J. Mat. Sci. 33, 371 (1966).

26. Langitan, F. B., and Lawn, B. R., "Hertzian Fracture Experiments on Abraded Glass Surfaces as Definite Evidence for an Energy Balance Explanation of Auerbach's Law," J. of Appl. Phys. 40, 4009 (1969).

27. Hirst, W., and Howse, M. G., "The Indentation of Materials by Wedges," Proc. Roy. Soc. A311, 429 (1969).

28. Lawn, B. R., Wilshaw, T. R., and Hartley, N. E. W., "A Computer Simulation of Hertzian Cone Crack Growth," Int. J. Fract. Mech. 10, 1 (1974).

29. Tabor, D., "The Hardness of Metals," Claredon Press, Oxford (1951).

30. Lawn, B. R. and Fuller, E. R., "Equilibrium Penny-Like Cracks in Indentation Fracture," J. Mat. Sci. 10, 2016 (1975).

31. Evans, A. G., and Wilshaw, T. R., "Dynamic Solid Particle Damage in Brittle Materials," J. Mat. Sci. 12, 97 (1977).

32. Evans, A. G., and Wilshaw, T. R., "Quasistatic Solid Particle Damage in Brittle Materials," Acta Met. 24, 939 (1976).

33. Lawn, B. R., Marshall, D. B., "Residual Stress Effects in Sharp Contact Cracking," J. Mat. Sci. 14, 2001 (1979).

34. Gilman, J. J., "Strength of Ceramic Crystals," Mechanical Behavior of Crystalline Solids, National Bureau of Standards Monograph 59, (1963).

35. Hertz, H., "Uber die Beruhrung Fester Elasticher Korper," 1881; reprinted in "Gesammelte werke von Heinrich Hertz," 1, 155, Leipzing (1895).

36. Hill, R., Lee, E. H., and Tupper, S. J., "The Theory of Wedge Indentation of Ductile Materials," Proc. Roy. Soc. A188, 273 (1947).

37. Shield, R. T., and Drucker, D. C., "The Application of Limit Analysis to Punch-Indentation Problems," J. of Appl. Mech. 20, 483 (1953).

38. Levin, E., "Indentation Pressure of a Smooth Circular Punch," Quarterly Appl. Mech. 13, 133 (1954).

39. Smith, F. W., Emery, A. F., and Kobayashi, A. S., "Stress Intensity Factors for Semi Circular Cracks," J. Appl. Mech. 34, Ser. E, 953 (1967).

40. Marsh, D. M., "Plastic Flow in Glass," Proc. Roy. Soc. A 279, 420 (1964).

41. Mulhearn, T. O., "The Deformation of Metals by Vickers Type Pyramidal Indenter," J. Mech. Phys. Solids 7, 85 (1959).

42. Lee, C. H., Masaki, S., and Kobayashi, S., "Analysis of Ball Indentation," Int. J. Mech. Sci. 14, 417 (1972).

43. Shaw, M. C., Hoshi, T., and Henry, O., "Reverse Plastic Flow Associated with Plastic Indentation," ASME Publication, Paper No. 78-WA/PROD-19.

44. Hill, R., "The Mathematical Theory of Plasticity," Oxford (1950).

45. Evans, A. G., "Strength Degradation by Projectile Impacts," J. Am. Cer. Soc. 56, 405 (1973).

46. Auerbach, F., "Absolute Härtemessung," Ann. Phys. Chem. 43, 61 (1891).

47. Sheldon, G. L., and Finnie, I., "The Mechanism of Material Removal in the Erosive Cutting of Brittle Materials," Trans. ASME 88B, 393 (1966).

48. Timoshenko, S. P. and Goodier, J. N., "Theory of Elasticity," McGraw Hill (1951).

49. Huber, M. T., "Theorie der Beruhrung Fester Elastischer Korper," Ann. Physik 14, 153 (1904).

50. Tillett, J. P. A., "Fracture of Glass by Spherical Indenter," J. Mat. Sci. B69, 47 (1956).

51. Frank, F. C. and Lawn, B. R., "On the Theory of Hertzian Fracture," Proc. Roy. Soc. London A299, 291 (1967).

52. Spense, D. A., "Self Similar Solutions to Adhesive Contact Problems with Incremental Loading," Proc. Roy. Soc. London A305, 55 (1968).

53. Goodman, L. E., "Energy Dissipation in Contact Friction: Constant Normal and Cyclic Tangential Loading," J. Appl. Mech. E84, 55 (1962).

54. Johnson, K. L., O'Connor and, J. J., and Woodward, A. C., "The Effect of the Indenter Elasticity on the Hertzian Fracture of Brittle Materials," Proc. R. Soc. London A334, 95 (1973).

55. Hardy, C., Baronet, C. N., and Tordian, G. V., "The Elastic-Plastic Indentation of a Half-Space by a Rigid Sphere," Intern. J. for Num. Meth. in Engr. 3, 451 (1971).

56. Dao, K. C., and Shockey, D. A., "Particle Impact Damage in Si_3N_4" SRI Intern. Annual Report, Part III (1979).

57. Roesler, F. C., "Indentation Hardness of Glass as an Energy Scaling Law," Proc. Phys. Soc. 69B, 55 (1956).

58. Sargent, G. A., Mehrotra, P. K., and Conrad, H., "Multiparticle Erosion of Pyrex Glass," ASTM STP 664, 77 (1979).

59. Johnson, K. L., "The Correlation of Indentation Experiments," J. Mech. Phys. Solids 18, 115 (1970).

60. Hamilton, B. and Rawson, H., "The Determination of Flaw Distribution on Various Glass Surfaces from Hertz Fracture Experiments," J. Mech. Phys. Solids 8, 127 (1970).

61. Oh, H. L. and Finnie, I., "On the Location of Fracture in Brittle Solids. I-Due to Static Loading," Int. J. of Fract. Mech. 6, 287 (1970).

62. Greenwood, J. A., and Tripp, J. H., "The Elastic Contact of Rough Surfaces," J. Appl. Mech., Trans. ASME E89, 153 (1967).

63. Cartwright, D. J. and Rooke, D. P. "Compendium of Stress Intensity Factors," London (1976). H.M.S.O.

64. Wiederhorn, S. M., and Lawn, B. R., "Strength Degradation of Glass Resulting from Impact with Spheres," J. Am. Cer. Soc. 60, 451 (1977).

65. Mathews, J. R., McClintock, and Shack, W. J., "Statistical Determination of Surface Flaw Density in Brittle Materials," J. Am. Cer. Soc. 59, 304 (1976).

66. Evans, A. G., and Jones, R. L., "Evaluation of a Fundamental Approach for the Statistical Analysis of Fracture," J. Am. Cer. Soc. 61, 156 (1978).

67. Fisher, G. M. C., "The Auerbach Range in the Hertzian Fracture of Glass," J. Appl. Phys. 38, 1781 (1967).

68. Sargent, G. A., Mehrotra, P. K., and Conrad, H., "A Model for Multiparticle Erosion of Brittle Solids by Spherical Particles," Proc. 5th Intern. Conf. on Erosion by Solid and Liquid Impact, Cambridge, England (1979).

69. Argon, A. S., "Surface Cracks on Glass," Proc. of the Roy. Soc. 250A, 472 (1959).

70. Chandhri, M. M., aand Walley, S. M., "Damage of Glass Surface by Impact of Small Glass and Steel Spheres," Phil. Mag. A 37, 153 (1978).

71. Adler, W. F., "Analysis of Multiparticle Impacts on Brittle Materials," Quart. Prog. Report 4. Air Force Material Lab, Project 7342 (1974).

72. Erdogan, F., and Sih, G. C., "On the Crack Extension in Plates Under Plane Loading and Transverse Shear," J. Basic Engr. Trans. ASME 88B, 393 (1966).

73. Reynolds, O., "On the Action of a Blast of Sand in Cutting Hard Materials," Phil. Mag. 46, 337 (1873).

74. Haworth, R. D., "The Abrasion Resistance of Metals," Trans. of ASM 41, 819 (1949).

75. Stocker, R. L., "Erosion Due to Dust Particles in a Gas Stream," Indust. and Engr. Chem. 41, 1196 (1949).

76. Finnie, I., "The Mechanism of Erosion of Ductile Materials" Proc. 3rd U.S. Nat. Congress of Applied Mech., 527 (1958).

77. Sheldon, G. L., and Finnie, I., "On the Ductile Behavior of nominally Brittle Materials in Erosive Cutting," Trans. ASME 88B, 387 (1966).

78. Oh. H. L., Oh, K. D. L., Vaidyanathan, S. and Finnie, I., "On the Shaping of Brittle Solids by Erosion and Ultrasonic Cutting," NBS Specl. Pub. 348 (1970).

79. Gulden, M., "Study of Erosion Mechanisms of Engineering Ceramics," ONR Contract No. N00014-73-C-0401 (1979).

80. Gordon, J. E., Marsh, D. M., and Parratt, M., "On the strength and structure of Glass," Proc. Roy. Soc. of London 249A, 65 (1959).

81. Zambelli, G., and Finnie, I., "Particulate Erosion on NiO Scales," Proc. 5th Intern. Conf. on Erosion by Solid and Liquid Impact, Cambridge, England (1979).

82. Ruff, A. W. and Wiederhorn, S. M., "Erosion by Solid Particle Impacts," Treatise on Materials Science and Technology 16, Material Erosion, New York: Academic press (1979).

83. Gulden, M. E., "Solid Particle Erosion of High-Technology Ceramics," ASTM STP 664, 101 (1979).

84. Gulden, M. E., "Effect of Number of Impacts on Erosion of Polycrystalline MgF_2 in the Elastic-Plastic Response Regime," J. Am. Cer. Soc. 63, 121 (1980).